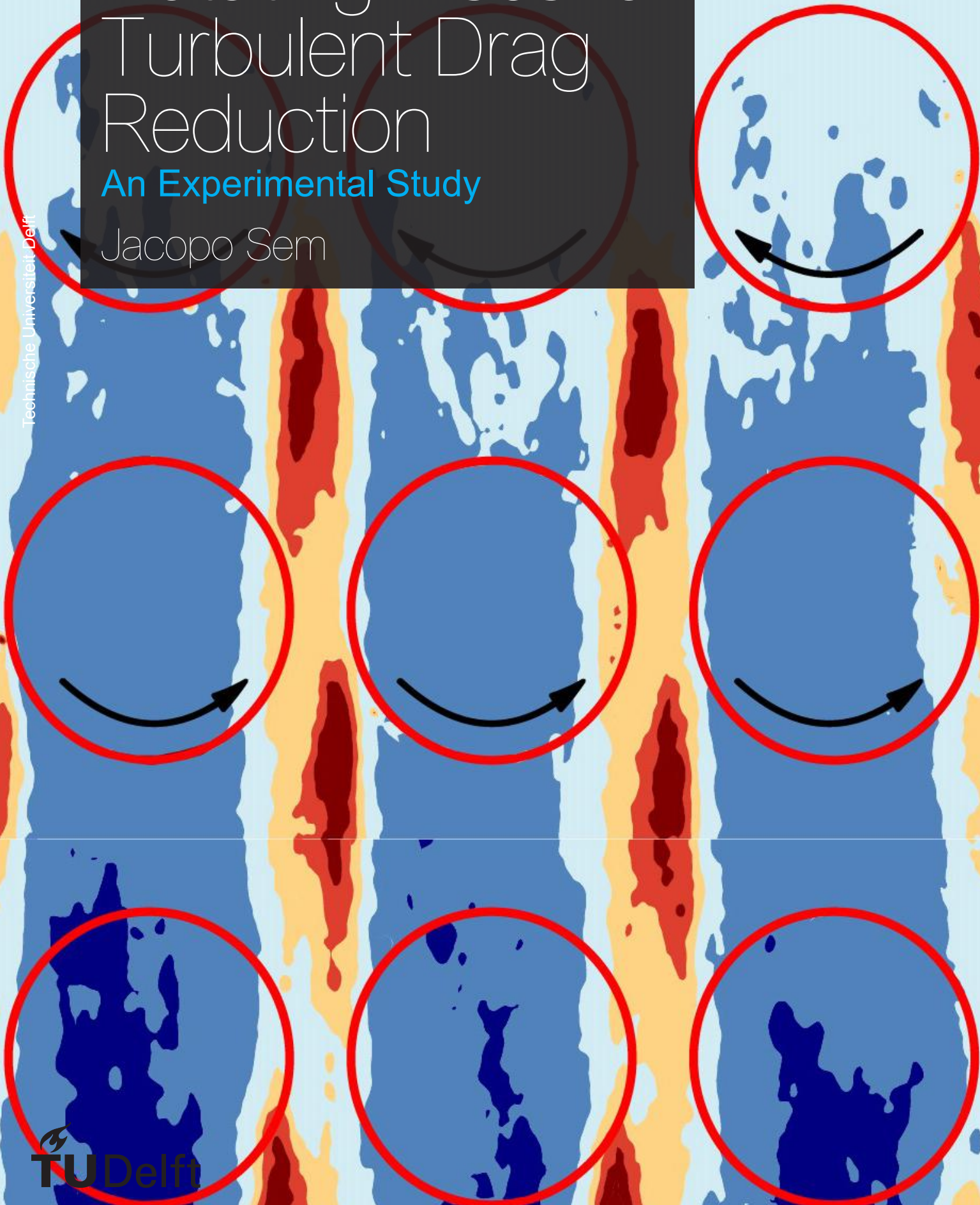


# Rotating Discs for Turbulent Drag Reduction

An Experimental Study

Jacopo Sem

Technische Universiteit Delft





# Rotating Discs for Turbulent Drag Reduction

An Experimental Study

by

Jacopo Sem

to obtain the degree of Master of Science  
at the Delft University of Technology,  
to be defended publicly on July 5, 2021.

Student number: 4458745  
Date uploaded: 21<sup>st</sup> June 2021  
Thesis supervisors: Dr. ir. W. Baars, TU Delft  
Ir. K. Kempaiah, TU Delft

# Abstract

The reduction of turbulent skin-friction drag has the potential to generate numerous societal benefits. In large-scale industrial applications, the largest share of energy consumption goes into overcoming the friction drag produced by turbulent boundary layers formed on the outside wall. Estimates assess that over 50% of the total fuel burn is due to overcoming friction drag, highlighting how reducing it would result in large environment and economic savings. In this work, an active technique for friction drag reduction in a turbulent boundary layer is studied in TU Delfts windtunnel laboratory. The flow over a stationary wall is modified by the steady rotation of flush-mounted discs - aiming to mimic a motion of wall-oscillation perpendicular to the flow, a well-documented turbulent drag reduction technique. The effect of the disc motion on turbulent drag is investigated at friction Reynolds numbers of 912 and 1483. The chosen rotational velocity of the discs, the disc diameter and disc spacing represent the optima defined in literature, and a further parameter exploration was conducted around these optima.

To assess the performance of the disc array, high resolution planar PIV is employed to measure skin-friction drag reductions at the wall, as well as to quantify second order statistics and other phenomena within the turbulent boundary layer. The results reveal drag reductions in the order of 50%, with Reynolds stresses and peaks of turbulent kinetic energy production decreasing by similar amounts. Analysis of turbulent velocity fluctuations reveals that the prevalence of turbulence producing events is significantly decreased close to the wall, and two-point correlations of vorticity contours show that vortical events are remarkably hindered by the disc rotation. Further analysis of a wall-parallel plane reveals that the mean velocity increases over the discs and decreases in between. This suggest that the detrimental effects of such a disc array occur at spanwise locations between each disc row, in accordance with literature. By using an assumption of outer flow similarity, the performance of the array is then quantified as being 10% less than the local optimum in the disc center.

# Acknowledgements

This thesis marks the end of an exciting time, not only counting the past nine months (which in reality were anything but exciting) but of my stay at TU Delft as a whole. It has been an exciting journey filled with highs and lows, but none has given me more of a sense of accomplishment than working on this thesis and extracting insights out of (literally) thin air.

The reality is that it has been such a long journey that I cannot possibly thank all the fantastic people who helped me through it. Every one of them contributed to making my stay here special in some way. But I wanna keep this preface short and sweet since I know whoever is reading this just cannot wait to read the rest of the thesis - so here it goes.

Thank you to Woutijn and Kushal for your feedback and help throughout the entire thesis, both in the lab and during the rest of the process. You've always been there for my questions at crazy hours of the day and helped me push the data in this thesis further than I thought possible. Thank you also to the lab staff, Dennis, Frits, Peter, Henk-Jan and Nico. You have helped me with your suggestions throughout, from feedback in designing parts to playing with mirrors, lenses and a high-power laser.

Thank you to Andrea, Jasper and Klemens for being amazing roommates and bearing with me when the lockdown got difficult to deal with (I promise there weren't any mental breakdowns).

Thank you Giulio, Enrico and all the other people who shared the "disagio" in aerodynamics, but also throughout my whole time in Delft. And also for the surf lessons. Thank you Ide for all the fun climbing sessions, I'm sure one day you'll crack the red and the black courses. Thanks Arthur, Victor and Katy for all the random stuff we've gotten up to in these past 6 years - I sure hope we can go on holiday all together again.

Thank you Siba for all the laughs and support, cheering me up when I was sad and listening to my endless rants - I definitely wouldn't have made it without you!

Finally last but absolutely not least the biggest thank you to my parents. Especially during the thesis you managed to avoid the dreaded "are we there yet"-equivalent and you always supported me no matter what. Can't wait to see you soon, hopefully on a Thai beach. And thank you Giona for all the fun we've had during the "great Italian lockdown".

*Dobby is a free elf!*

---

Dobby, c.1992

# Contents

<b>Abstract</b>	<b>iv</b>
<b>Acknowledgements</b>	<b>v</b>
<b>Contents</b>	<b>vi</b>
<b>1 Introduction</b>	<b>1</b>
1.1 Scope	3
1.2 Research Methodology	4
<b>2 Fundamentals of Boundary Layers</b>	<b>5</b>
2.1 The Turbulent Boundary Layer	6
2.1.1 Parametrization of the Boundary layer	7
2.2 Turbulence Cascade and Production	9
2.3 Coherent Structures in Boundary Layers	11
2.3.1 Inner Layer Structures	12
2.3.2 Outer Layer Structures	13
2.3.3 Vortical Structures within the TBL	14
2.4 Mechanisms of Friction Drag Generation and Reduction	15
2.4.1 Linking Turbulent Fluctuations to Friction Drag	15
2.5 Reynolds Number Effects	16
2.5.1 Experimental Research	16
2.5.2 Structures and Self-Similarity	17
2.6 Summary	19
<b>3 Turbulent Drag Reduction</b>	<b>20</b>
3.1 Passive Methods for Drag Reduction	21
3.1.1 Large Eddy Breakup Devices	21
3.1.2 Riblets	22
3.2 Active Methods for Drag Reduction	23
3.2.1 Wall Oscillations	23
3.3 Reynolds Number Effects on Oscillating Walls	26
3.4 Spatial vs. Temporal Forcing	27
3.5 Industrial Readiness of TDR Techniques	27
3.6 Summary	28
<b>4 Rotating Discs</b>	<b>29</b>
4.1 Normal Vorticity Actuators	30
4.2 Rotating Discs for Friction Drag Reduction	30
4.2.1 Flow Structures and Drag Reduction Mechanisms	32
4.3 Disk Spacing	33

4.4	Oscillating Discs . . . . .	35
4.5	Summary . . . . .	37
<b>5</b>	<b>Experiment Design and Methodology</b>	<b>38</b>
5.1	Wind Tunnel . . . . .	39
5.2	Setup and Coordinate System . . . . .	39
5.3	Test Section . . . . .	40
	5.3.1 Design Methodology . . . . .	41
	5.3.2 Assembly Considerations . . . . .	42
5.4	Measurement Equipment Setup . . . . .	42
<b>6</b>	<b>Measurement Techniques</b>	<b>44</b>
6.1	Particle Image Velocimetry . . . . .	45
	6.1.1 Seeding . . . . .	45
	6.1.2 Illumination . . . . .	46
	6.1.3 Imaging . . . . .	46
6.2	Data Acquisition . . . . .	48
	6.2.1 Calibration . . . . .	49
	6.2.2 Locations of Measurement Planes . . . . .	49
	6.2.3 Non-dimensional Test Matrix . . . . .	50
6.3	Data Processing and Reduction . . . . .	52
	6.3.1 Cropping . . . . .	53
	6.3.2 Data Reduction . . . . .	54
	6.3.3 Reconstruction of full boundary layer profile . . . . .	56
6.4	Uncertainty Analysis . . . . .	57
	6.4.1 Statistical Uncertainty . . . . .	57
	6.4.2 Interrogation Window Size Uncertainty . . . . .	57
	6.4.3 Cross-Correlation Uncertainty . . . . .	57
	6.4.4 Particle Tracing Uncertainty . . . . .	58
	6.4.5 Uncertainty in numbers . . . . .	58
<b>7</b>	<b>Results and Discussion</b>	<b>59</b>
7.1	Canonical Turbulent Boundary Layer . . . . .	60
7.2	Wall Shear and Friction Velocity estimation . . . . .	62
7.3	Turbulence Statistics . . . . .	66
	7.3.1 Reynolds Shear Stresses . . . . .	66
	7.3.2 Near Wall TKE Production . . . . .	67
7.4	Quadrant Decomposition . . . . .	68
7.5	Instantaneous Field Organization . . . . .	71
7.6	Over-Array Structure Behaviour . . . . .	75
7.7	Discussion . . . . .	80
<b>8</b>	<b>Conclusion and Recommendations</b>	<b>84</b>
8.1	Conclusions . . . . .	84
8.2	Recommendations . . . . .	86
<b>A</b>	<b>Appendix A - Technical Drawings</b>	<b>88</b>
<b>B</b>	<b>Appendix B - Test Matrices</b>	<b>93</b>

**Bibliography**

# List of Figures

1.1	Drag breakdown on passenger aircraft, replicated from Marec, 2001 . . . . .	1
1.2	Environmental impact of drag savings, replicated from Marec (2001). Figure refers to a 1% reduction in total aerodynamic drag for an A340 aircraft operating in long range mode, resulting in 400,000L of fuel saved per year per aircraft. . . . .	2
2.1	Simplified geometry of TBL, from Perlin et al. (2016) . . . . .	6
2.2	Dependence of skin-friction coefficient on Reynolds number on flat plate boundary layer (Sforza, 2014) . . . . .	7
2.3	Mean Velocity profile of smooth plate turbulent boundary layer . . . . .	9
2.4	Schematic Diagram of the energy cascade at high Reynolds numbers. Adapted from Pope (2001) . . . . .	10
2.5	Labelled Reynolds stresses at $Re_\theta = 5230$ , adapted from Sillero et al. (2013). Symbols are an experiment from Osaka et al. (1998) . . . . .	11
2.6	Streaks at $y^+ = 4.5$ (Kline et al., 1967) . . . . .	12
2.7	The $u - v$ sample space showing the numbering of the four quadrants, with labelled sweeps and ejections. . . . .	13
2.8	Vectorized drawing of the viscous superlayer from Falco (1977), (Pope, 2001) . . . . .	14
2.9	Different hairpin geometries and structures, adapted from Adrian (2007) . . . . .	15
2.10	Pre-multiplied turbulence energy production. Adapted from Marusic et al. (2010) and Smits et al. (2011). . . . .	18
2.11	<b>Left:</b> Inner normalized time between pocket events $T^+$ as a function of Reynolds number. <b>Right:</b> Inner normalized streak spacing $\lambda^+$ versus Reynolds number. (Present study: Klewicki et al. (1995). Others: Yoo et al. (1991) and Smith and Metzler (1983)) . . . . .	18
3.1	Sketch of tandem arrangement for LEBUs, from Gad-El-Hak (2000) . . . . .	21
3.2	Generic scalloped riblet geometry (Adapted from Bilinsky (2017)) . . . . .	22
3.3	Velocity contours showing vortical structures within the riblet valleys, from El-Samni et al. (2007) . . . . .	23
3.4	Setup of an oscillating wall experiment, by Laadhari et al. (1994) . . . . .	24
3.5	Three dimensional plot of drag reduction (circle size) versus $T^+$ and $W^+$ . From Quadrio and Ricco (2004) . . . . .	25
3.6	Percent drag reduction vs a-dimensional oscillation period for $A^+ = 12$ . Adapted from Gatti and Quadrio (2013). . . . .	26
4.1	Schematic of the turbulent channel flow with disc arrangement used in the parametric study by RH13. . . . .	31
4.2	Map of drag reduction as a function of $D^+$ and $W^+$ . The numbers within the circles represent the reduction percentage. . . . .	31

4.3	Isosurfaces of $\sqrt{u_d^{+2} + w_d^{+2}} = 2.3$ , isometric view with the discs in dark grey <b>(a)</b> and seen from the $y - z$ plane <b>(b)</b> . Adapted from RH13. The rotating discs are in darker grey. . . . .	32
4.4	Isosurfaces for stationary wall case <b>(a)</b> and rotating disc flow case <b>(b)</b> . . . . .	32
4.5	Disc layouts studied by Wise et al. (2014) in the $x - z$ plane. . . . .	33
4.6	Map of drag reduction (circled values) for different streamwise and spanwise spacing, for a single value of $D$ and $W$ . . . . .	34
4.7	Isosurfaces for fixed $D$ and $W$ for cases $C_3$ and $C_4$ . . . . .	34
4.8	Schematic showing the two mechanisms determined to be responsible for the drag reduction. Radial flow spanwise forcing (Eq. 5.3) over the disc and structures (Eq. 5.4) between discs. Adapted from Wise et al., 2018 . . . . .	36
4.9	instantaneous $\lambda_2$ iso-contours for <b>a)</b> reference flow, <b>b)</b> rotating rings only, <b>c)</b> rotating rings and opposition control and <b>d)</b> rotating rings and hydrophobic surface . . . . .	36
5.1	Full windtunnel test sections as described. Wooden extension <b>(1)</b> , plexiglass <b>(2)</b> and open bottom test section <b>(3)</b> . . . . .	39
5.2	<b>(a, b)</b> 2D schematic of full experimental setup. <b>(c)</b> Detailed view of disc array, with non-equidistant spacing in the streamwise and spanwise directions. The angular velocity direction is shown by the blue arrow. . . . .	40
5.3	Render of LEGO trip . . . . .	41
5.4	RPM Map for disc array, pattern of various voltages measured. Darker is faster, but the scale is not absolute (fastest to lowest spinning discs only have $\sim 5\%$ deviation) . . . . .	42
6.1	Excess seeding . . . . .	45
6.2	Configurations of 2D-2C PIV, FOVs in wall-normal plane <b>(a, b)</b> and in the wall parallel plane <b>(c)</b> . In all configurations, the sCMOS cameras are located outside of the tunnel, with the optical axis perpendicular to the FOV-planes . . . . .	50
6.3	Non-dimensional test matrix for $D^+$ and $W^+$ combinations. RH13's optimum is found at the red dot, and blue stars represent points tested in in this work. . . . .	51
6.4	Horizontal near wall crop . . . . .	54
6.5	Extracted volume for near-wall measurements, pre-processed (left) and correlated (right). . . . .	54
6.6	Data reduction steps to make the mean profiles suitable for analysis . . . . .	55
6.7	Normalized wall-normal velocity distribution for 3 [m/s]. Disc leading and trailing edge are marked at $x = 2.6\delta$ and $x = 3.38\delta$ respectively. Disc surface is marked with the dash-dotted line. . . . .	56
7.1	Characterization of TBL at $Re_\theta = 1966$ , both profiles normalized with inner variables . . . . .	60
7.2	characterization at $Re_\theta = 3270$ , both profiles normalized with inner variables . . . . .	61
7.4	Comparison of wall-normalized boundary layer profiles, extracted from each section of FOV-4 as described in Section 6.3.2. . . . .	63
7.5	Comparison of wall-normalized boundary layer profiles on semilogarithmic axis. . . . .	63
7.6	Wall-normal velocity contours over the fourth disc. Measured at $Re_\theta = 1966$ , $W^+ = 0$ <b>(A)</b> and $W^+ = 25$ <b>(B)</b> . . . . .	64
7.7	Skin-friction coefficient calculated using Eq. 7.1 per section, $Re_\theta = 1966$ . . . . .	65
7.8	Mean streamwise Reynolds stresses for each section over the disc, $Re_\theta = 1966$ . . . . .	66
7.9	Turbulence Kinetic Energy Production normalized by outer variables $u_\infty$ and $\delta_{99}$ for $Re_\theta = 1966$ . . . . .	68

7.10	Probability Density Function of streamwise and wall-normal velocity fluctuations for a selection of wall-normal locations. $Re_\theta = 1966$ . . . . .	69
7.11	Two-point cross correlation map of $u'$ at $y^+ = 50$ . . . . .	70
7.12	0.1 threshold contours of two-point correlation coefficients for $u'$ fluctuations. Captured at $y^+ = 25, 50, 70, 100$ from bottom to top. Axis normalized with viscous units. . . . .	71
7.13	<b>(1)</b> Hairpin vortices heads, <b>(2)</b> wake layer vorticity signatures, <b>(3)</b> viscous sublayer. . . . .	72
7.14	Instantaneous fields captured at $Re_\theta = 1966$ and colored by vorticity. . . . .	72
7.15	Two-point cross correlation map for $\omega_z$ calculated at $y^+ = 50$ and $Re_\theta = 1966$ . . . . .	73
7.16	Two-point cross correlation contours of $\omega_z$ with a threshold value of 0.1. Contours at $y^+ = 25, 50, 70, 100$ . . . . .	74
7.17	Location of wall parallel imaging plane. The red line is the mean velocity over the fields of view, and black dash-dotted lines are the upper and lower bounds of velocities found within the FOV. . . . .	75
7.18	Normalized mean velocity for different RPMs at $Re_\theta = 1966$ . Discs locations are highlighted in red, with their direction of rotation marked by the arrow. . . . .	76
7.19	In plane normalized vorticity contours for three different RPMs at $Re_\theta = 1966$ . Discs locations are highlighted in red, and the black dots to the left of the image are poor quality data-points far into the test section. . . . .	77
7.20	In plane normalized streamwise Reynolds stresses contours for three different RPMs at $Re_\theta = 1966$ . Discs locations are highlighted in red. . . . .	78
7.22	Velocity defect for DNS solutions of a channel flow at $Re_\tau = 550$ and $Re_\tau = 1000$ . Note how the “fan” between $y/h = 0.05$ and $y/h = 0.4$ becomes more cohesive as the Reynolds number increases. . . . .	80
7.23	Mean normalized spanwise velocity over the streamwise extent of FOV-4 (curved lines) compared to measurement location (dots). The horizontal lines represent the mean velocity over the entire array. . . . .	81
7.24	Schematic aiming to illustrate the different types of flow phenomena present in a disc array. Over the discs the flow behaves like in an oscillating wall, while between the discs the flow is strongly sheared. . . . .	83
8.1	Wall-normal velocity contours over the fourth disc, measured at $Re_\theta = 1966$ and $W^+ = 25$ . . . . .	86
A.1	The plate holding the disc array in the test section . . . . .	89
A.2	The disc . . . . .	90
A.3	The plate used to secure the discs flush with the plate in Fig. A.1 . . . . .	91
A.4	Assembly of motor, mounting plate and disc. . . . .	92

# List of Tables

6.1	<i>dt</i> used for each dataset-type collected . . . . .	48
6.2	Specifications of Imaging Equipment . . . . .	48
6.3	Non-dimensional disc velocities and relevant nomenclature used in the Results section. . . . .	51
6.4	Report of uncertainty values. . . . .	58
7.1	Turbulent Boundary Layer properties. The friction Reynolds number has been calculated using the $u_\tau$ from the linear region. . . . .	62
7.2	Skin Friction coefficient and change to baseline for tested datasets. Data is mean of sections from Figure 7.7, captured over the last central disc. . . . .	65
B.1	Test matrix for FOVs over the discs . . . . .	93
B.2	Test matrix for wall parallel FOVs . . . . .	93
B.3	Test matrix for FOVs over the full array . . . . .	94

# List of Symbols and Abbreviations

## Abbreviations

<i>APG</i>	Adverse Pressure Gradient
<i>CMOS</i>	Complementary metaloxidesemiconductor
<i>DNS</i>	Direct Numerical Simulation
<i>FIK</i>	Fukagata-Iwamoto-Kasagi (identity)
<i>FOV</i>	Field of View
<i>FPG</i>	Favorable Pressure Gradient
<i>LEBU</i>	Large Eddy Break-Up
<i>Nd : YAG</i>	Neodymium-doped Yttrium Aluminium Garnet (laser)
<i>PIV</i>	Particle Image Velocimetry
<i>RPM</i>	Rotations Per Minute
<i>TBL</i>	Turbulent Boundary Layer
<i>TDR</i>	Turbulent Drag Reduction
<i>TKE</i>	Turbulent Kinetic Energy
<i>ZPG</i>	Zero Pressure Gradient

## Greek Symbols

$\delta, \delta_{99}$	Boundary layer thickness	[ <i>m</i> ]
$\delta^*$	Displacement thickness	[ <i>m</i> ]
$\delta_v$	Viscous lengthscale	[ <i>m</i> ]
$\epsilon_\kappa$	Turbulence kinetic energy dissipation	[ $m^2/s^3$ ]
$\epsilon_{xx}$	Uncertainty of parameter <i>xx</i>	[–]
$\kappa$	Turbulence kinetic energy	[ <i>J/Kg</i> ]
$\lambda$	Laser wavelength	[ <i>nm</i> ]
$\mu$	Dynamic viscosity	[ <i>Kg/(m · s)</i> ]
$\nu$	Kinematic viscosity	[ $m^2/s$ ]
$\Omega$	Disc rotational velocity	[ <i>rad/s</i> ]
$\omega$	Wall-oscillation angular velocity	[ <i>rad/s</i> ]
$\rho$	Density	[ <i>Kg/m<sup>3</sup></i> ]
$\rho_{aa}$	Auto-correlation coefficient	[–]
$\theta$	Momentum thickness	[ <i>m</i> ]

## Latin Symbols

$\mathcal{P}_\kappa$	Turbulence kinetic energy production	[ $m^2/s^3$ ]
$\mathcal{R}_d$	Drag effect of interdisc structures	[–]
$\mathcal{R}_t$	Drag effect of spanwise forcing	[–]
$\tau_w$	Wall shear stress	[ <i>Pa</i> ]
<i>A</i>	Wall-oscillation amplitude	[ <i>m</i> ]
$C_f$	Skin-friction coefficient	[–]
<i>D</i>	Disc diameter (Non-dimensional, $D^+$ )	[ <i>m</i> , (–)]
$D_0$	Nominal disc diameter	[ <i>m</i> ]
<i>dt</i>	Laser pulse interval	[ $\mu s$ ]
<i>f</i>	Focal length	[ <i>mm</i> ]

$f_{\#}$	f-stop	[-]
$H$	Shape factor	[-]
$l_{pix}$	Pixel size	[ $\mu m$ ]
$M$	Magnification factor	[-]
$P_{\infty}$	Pressure	[Pa]
$R_{xx}$	Reynolds stress, $xx$ -component	[m/s]
$Re_{\theta}$	Momentum Reynolds number	[-]
$Re_{\tau}$	Friction Reynolds number	[-]
$Re_x$	Reynolds number	[-]
$T$	Wall-oscillation time period	[s]
$u$	Velocity x-component	[m/s]
$u'$	Velocity fluctuation, x-component	[m/s]
$U_{\infty}$	Freestream velocity	[m/s]
$u_{\tau}$	Friction Velocity	[m/s]
$v$	Velocity y-component	[m/s]
$v'$	Velocity fluctuation, y-component	[m/s]
$W$	Disc tip velocity (Non-dimensional, $W^+$ )	[m/s, (-)]
$w$	Velocity z-component	[m/s]

## Chapter 1

# Introduction

Calls for more sustainability and further environmental regulatory pressure are some of the main drivers of transport engineering in the modern world. The cost efficiency of transporting people and goods is put into question more now than ever before, especially considering the active and passive environmental damages caused by airlines, freight and passenger ships and even conventional oil pipelines.

The aviation industry has been delivering improvements under massive pressure from regulatory bodies and the public alike, all the way from more efficient ducted turbofan engines to new composite structures offering higher strength to weight ratios than ever before (Mahashabde et al., 2011). Recently, Airbus has committed to a new zero emission commercial airliner making use of hydrogen fuel cells (Duvelleroy et al., 2020), aiming to maximize sustainability long shunned for its environmental impacts.

Despite all these improvements, aerodynamic drag has been known to be one of the main sources of fuel consumption (Schrauf, 2005). Aerodynamic drag is defined as the force acting on any solid body moving in a surrounding fluid (Anderson, 2010). From the body's perspective, this force can be decomposed into two parts: the *pressure drag* due to pressure distributions over the body and the *friction drag* due to the viscous effects acting on the body. For streamlined bodies such as airlines and ships, the friction drag is the primary component of the drag force while pressure drag is more prominent in bluff bodies such as wheeled transport vehicles.

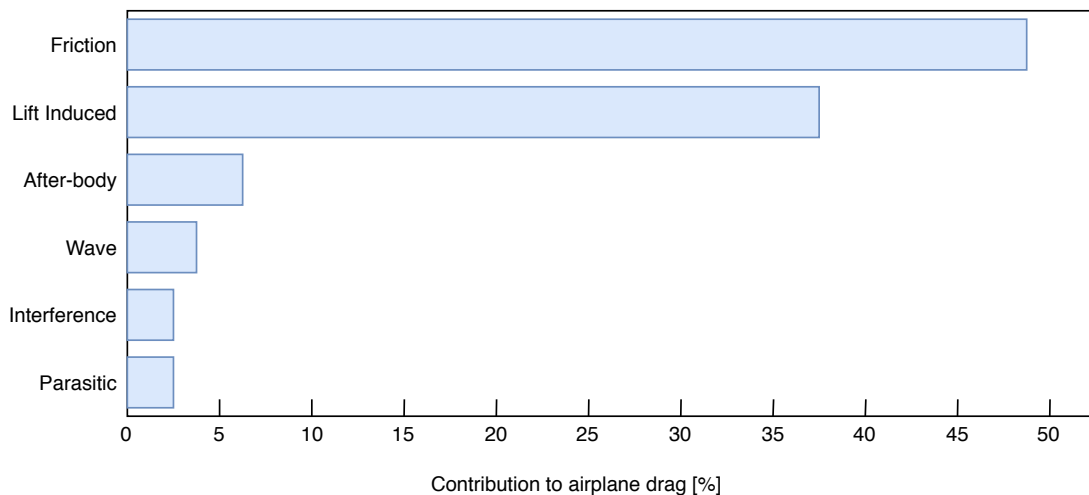


FIGURE 1.1: Drag breakdown on passenger aircraft, replicated from Marec, 2001

Friction drag reduction is one of the greatest challenges in modern engineering and fluid dynamics research. An opportunity to achieve significant reductions in turbulent friction drag would lead to immense energy savings throughout the entire engineering spectrum. Consider, for example, that

friction drag is roughly 50% of the total drag of a conventional surface ship (Perlin et al., 2016) and similar numbers for commercial aircraft (Schrauf, 2005) a small reduction in friction drag would therefore bring enormous monetary and environmental incentives in the industry. This relation is clearly visualized in Figure 1.2 below, showing the paramount importance of understanding the underlying flow physics and drag-generation mechanisms, and to developing methods to affect skin-friction drag. Scientific studies aimed at changing skin-friction drag can lead the development of practical systems for achieving drag reduction at industrial scales.

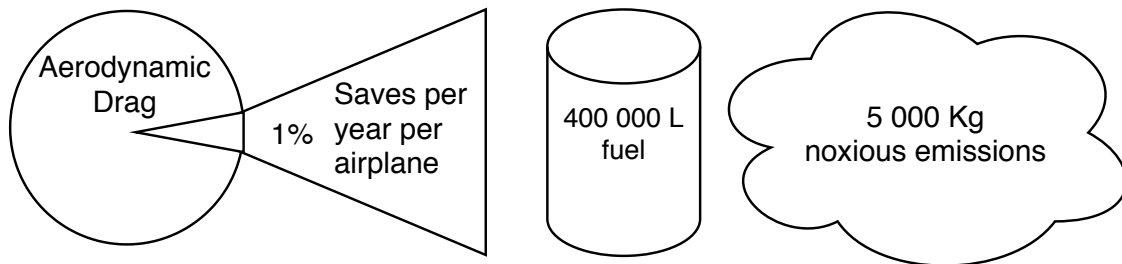


FIGURE 1.2: Environmental impact of drag savings, replicated from Marec (2001). Figure refers to a 1% reduction in total aerodynamic drag for an A340 aircraft operating in long range mode, resulting in 400,000L of fuel saved per year per aircraft.

Skin friction drag arises due to the boundary layer, a region of fluid where the mean momentum is decreased by the action of the wall-shear stress generated by the no-slip boundary condition at the wall. This boundary layer can either be laminar or turbulent, with every boundary layer transitioning into a turbulent state after a certain critical velocity or length-scale is reached. For this reason among others, the majority of skin-friction reduction research is performed in the area of turbulent boundary layers. Note that laminar boundary layers constitute a much lower skin-friction drag than their turbulent counterparts, and as such, another research area of interest is delaying the laminar-to-turbulent transition on transportation systems. Nevertheless, transition is unavoidable due to roughness, free-stream turbulence and cross-flow instabilities. This is why turbulent drag reduction will remain a topic of scientific and practical interest.

The turbulent boundary layer is generally referred to as being subjected to random fluctuations of velocities and other related quantities. These fluctuations are superimposed to the mean flow, and as such they render the behaviour of the bulk flow rather unpredictable. In recent years however, it has come to light how turbulent flows are actually comprised of several types of coherent structures (Townsend, 1951; Adrian, 2007), with quasi-streamwise vortices and low-speed streaks being the primary drivers of skin friction and therefore turbulent wall drag. Because of this limited number of features directly related to skin friction drag, the majority of research in this area is focused on suppressing these features via various methods (Choi et al., 1994; Baron and Quadrio, 1995; Ricco, 2004; Bai et al., 2014). The control methods used are both active and passive, and they range from simple surface textures to complex oscillating mechanisms.

Ricco and Hahn, 2013 performed a numerical study on an array of wall-flush mounted rotating discs, inducing a spanwise triangular wave by having neighbouring streamwise discs spinning in opposite directions. Further numerical optimization studies were performed by Wise et al., 2014, Wise and Ricco, 2014 and Olivucci et al., 2019, but no experimental campaign has been conducted yet. Furthermore, the Reynolds numbers at which the aforementioned studies were performed were all relatively low, many orders of magnitude removed from typical large scale industrial applications.

## 1.1 Scope

Given the current research in the field of skin-friction drag reduction in turbulent flows and the capabilities of the research facilities at Delft University of Technology, the objective of this work is as follows:

*The objective of this research project is to perform a PIV-based experimental campaign on an array of rotating discs with the goal to understand its effect on the flow, including an investigation on the skin-friction drag reduction.*

Effectively this objective implies the measurement of the flowfield over a disc, which will be spun at different RPM to understand how its rotation can influence the flow physics. The disc will be part of an array where successive streamwise rows of discs rotate in different directions, effectively creating a spanwise wave. In general, the change of boundary conditions at the wall has limited effects on vortical structures and the turbulence cycle. Altering the boundary conditions to pure wall oscillations has been studied in detail before and resulted in a reduction in hairpin packets, decreases in turbulence coherence and an overall decrease in turbulent skin-friction drag (Baron and Quadrio, 1995; Skote, 2013; Kempaiah et al., 2020). Spatial oscillations such as the ones undertaken in this work aim to achieve the same effects on the flowfield, but without oscillating the entire wall. In order to properly quantify the flowfield resulting from this interaction, several measurements will be taken. The velocity field is going to be imaged using Particle Image Velocimetry (PIV), and turbulence structures will be visualized using several post-processing techniques in an attempt to understand the flow physics. These experimental and data processing techniques will serve as a tool to understand key aspects of the problem.

To control the interaction between the flow and the experiment, several key performance parameters will need to be defined. These are, in no particular order,

- **Disc diameter:** The physical disc diameter, defined in the design phase and left constant throughout the experimental campaign.
- **Disc rotational velocity:** The RPM of the disc, defined at the start of the experimental campaign and changed throughout. One of the control parameters.
- **Disc stream- and spanwise spacing:** The physical spacing of the discs in the streamwise and spanwise directions. Like the diameter, this is defined in the design phase and left constant throughout the work.
- **Flow velocity:** The flow velocity at which the experimental campaign is conducted. This will indirectly influence the scaled dimensions of the other performance parameters via the Reynolds number. One of the control parameters.

With the parameters defined it is possible to identify the main research question, an answer to which will be sought throughout the project.

**How do turbulent boundary layer dynamics above an array of rotating discs mounted flush with the wall vary with a change to disc the control parameters, and why?**

This question can then be branched off into several sub-questions, answered separately throughout the work.

1. *How does the rotation of the discs influence the turbulent boundary layer?*

- 1.1. *Can the effect of this rotation on the near wall slope of the boundary layer profile be quantified?*
  - 1.2. *What is the effect of various disc rotational velocities on skin-friction trends?*
  - 1.3. *What is the effect of varying disc rotational speed and Reynolds number while keeping a constant diameter?*
  - 1.4. *What is the effect of disc rotation on the turbulent statistics?*
  - 1.5. *What speculations can be made about the features of the flow from the data visualization employed?*
2. *What is the effect of the Reynolds number on the flowfield influenced by the discs rotating?*
    - 2.1. *What is the effect of higher Reynolds numbers on disc scaling factors?*

## 1.2 Research Methodology

In relation to the research questions presented, it is necessary to define ways in which the main flow variables can be measured.

Regarding flow measurement techniques, planar PIV imaging is going to be used to measure and quantify the velocity field and the complex three-dimensional interactions between the discs and the flowfield. Unlike tomographic and stereoscopic PIV which can measure the full three-dimensional velocity gradient tensor and resolve the out of plane component, respectively, this work will limit itself at measuring the in-plane velocity components. This is mainly because of the complexity involved in setting up the former two techniques.

In-plane velocity data can be used as a good indicator for the presence and coherence of turbulent structures, as well as a quantification for various mean quantities related to turbulence statistics. This data analysis will not be done only on wall-normal imaging planes, but also on wall-parallel ones. The wall-parallel plane imaged will capture data over the entire array of discs, allowing for the definition of a general theory on how the rotating discs are influencing the flowfield in the logarithmic layer.

## Chapter 2

# Fundamentals of Boundary Layers

This chapter presents an overview of turbulent boundary layers developing over a flat plate. This topic is of main importance for the literature survey, and as such its fundamental components must be understood. Turbulent flows are ones in which the velocity field varies significantly and erratically in both position and time (Pope, 2001); within this definition, they can be either free shear or wall bounded flows. Wall bounded flows can be further categorized as internal flows - flowing through pipes and ducts - and external flows - present over the fuselages of aircrafts or the hulls of ships. Three wall bounded flows with the simplest geometries and with the mean velocity parallel to the wall are dubbed the canonical flows: these are as the fully developed pipe flow, fully developed channel flow, and the flat-plate boundary layer (Buschmann and Gad-El-Hak, 2006). For the purposes of this study, the turbulent boundary layer on a flat plate will be reviewed more in depth - first described using mean quantities (Section 2.1) and then focusing on turbulent fluctuations (2.2).

### Contents

---

<b>2.1</b>	<b>The Turbulent Boundary Layer</b> . . . . .	<b>6</b>
2.1.1	Parametrization of the Boundary layer . . . . .	7
<b>2.2</b>	<b>Turbulence Cascade and Production</b> . . . . .	<b>9</b>
<b>2.3</b>	<b>Coherent Structures in Boundary Layers</b> . . . . .	<b>11</b>
2.3.1	Inner Layer Structures . . . . .	12
2.3.2	Outer Layer Structures . . . . .	13
2.3.3	Vortical Structures within the TBL . . . . .	14
<b>2.4</b>	<b>Mechanisms of Friction Drag Generation and Reduction</b> . . . . .	<b>15</b>
2.4.1	Linking Turbulent Fluctuations to Friction Drag . . . . .	15
<b>2.5</b>	<b>Reynolds Number Effects</b> . . . . .	<b>16</b>
2.5.1	Experimental Research . . . . .	16
2.5.2	Structures and Self-Similarity . . . . .	17
<b>2.6</b>	<b>Summary</b> . . . . .	<b>19</b>

---

## 2.1 The Turbulent Boundary Layer

The generic shape of a boundary layer is represented in Figure 2.1 below, displaying the turbulent boundary layer developing from  $x = 0$ , with the freestream velocity  $U_\infty$  parallel to the surface over which the TBL is forming. The quantity  $\delta(x)$  represents the boundary layer thickness, defined as the wall-normal location where the average flow velocity is 99% of the external one. Anything encompassed within this distance from the wall is referred to as the boundary layer.

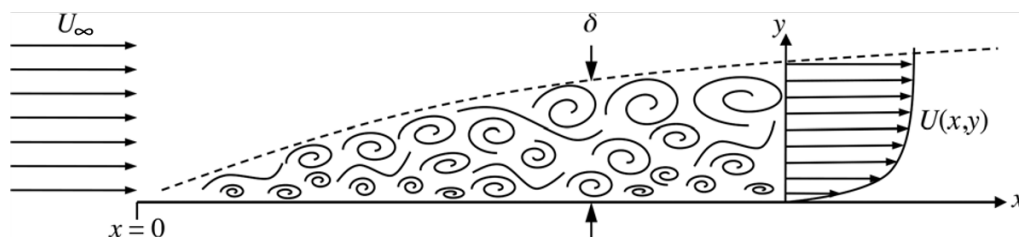


FIGURE 2.1: Simplified geometry of TBL, from Perlin et al. (2016)

This flow can be characterized by the density  $\rho$  and the dynamic viscosity  $\mu$ . This flow viscosity and the no-slip boundary condition at the wall are what causes a boundary layer to develop once the stationary plate is met at  $x = 0, y = 0$ . Furthermore, the free-stream pressure  $P_\infty(x)$  can be linked to the external velocity  $U_\infty$  by Bernoulli's equation, so that the pressure gradient is

$$\frac{dP_\infty}{dx} = -\rho U_\infty \frac{dU_\infty}{dx} \quad (2.1)$$

Accelerating flow corresponds to a negative, also known as favorable, pressure gradient (FPG). A decelerating flow on the other hand corresponds to a positive, adverse, pressure gradient (APG); in this case, the boundary layer is inclined to eventually separate from the surface. The third and most common type of flow in engineering applications for large scale transport is a zero pressure gradient (ZPG), where the flow is neither accelerating nor decelerating (George and Castillo, 1997). As mentioned earlier, the boundary layer thickness  $\delta$  is generally defined as the value of  $y$  for which the mean flow velocity  $\bar{u}(x, y)$  equals 99% of the free stream velocity. However, there also exist other definitions of the thickness that are not reliant on the measurement of a small velocity difference. These are integral measures, such as the displacement thickness

$$\delta^*(x) \equiv \int_0^\infty \left(1 - \frac{\bar{u}}{U_\infty}\right) dy \quad (2.2)$$

and the momentum thickness

$$\theta(x) \equiv \int_0^\infty \frac{\bar{u}}{U_\infty} \left(1 - \frac{\bar{u}}{U_\infty}\right) dy \quad (2.3)$$

These relations explain how much the wall would have to be displaced into an inviscid flow maintaining the same mass flow rate (the former) and same streamwise momentum (the latter). The ratio between the displacement thickness and the momentum thickness is defined as the shape factor  $H$ , which quantitatively describes the "tapering-off" of the velocity profile. The lower the shape factor, the higher the momentum of the flow for the same displacement thickness and therefore the steeper the velocity profile. These parameters are fundamental in understanding the TBLs dealt with within this work.

The boundary layer contains flow that has been slowed down by the action of the shear stress  $\tau_w$  at the wall. For smooth surfaces, this shear stress is determined from the flow viscosity and the wall-normal velocity gradient evaluated at  $y = 0$

$$\tau_w = \mu \left( \frac{\partial \bar{u}}{\partial y} \right)_{y=0} \quad (2.4)$$

Alternatively, one can integrate the momentum thickness equation (Eq. 2.3) to obtain the von Karman's integral momentum equation. For the zero pressure gradient case the result is Equation 2.5 below, quantifying the decrease in the momentum flow rate (and therefore the increase in the momentum deficit) caused by the wall shear stress.

$$\tau_w = \frac{d}{dx} (\rho U_\infty^2 \theta) = \rho U_\infty^2 \frac{d\theta}{dx} \quad (2.5)$$

Furthermore, for engineering purposes, the shear stress can be rendered non-dimensional and is generally expressed as the skin-friction coefficient

$$C_f = \frac{\tau_w}{\frac{1}{2} \rho U_\infty^2} = 2 \frac{d\theta}{dx} = 2 \left( \frac{u_\tau}{U_\infty} \right)^2 \quad (2.6)$$

When the dependence of this coefficient is plotted versus the Reynolds number (defined as  $Re = U_\infty x / \nu$ , with  $x$  the distance from the leading edge of the plate,  $U_\infty$  the freestream velocity and  $\nu$  the kinematic viscosity) as in Figure 2.2, it is immediately noticeable how the friction coefficient goes down when the Reynolds number increases. This happens because the conversion of momentum into shear force at the wall decreases in effectiveness as the flow proceeds downstream and the Reynolds number increases.

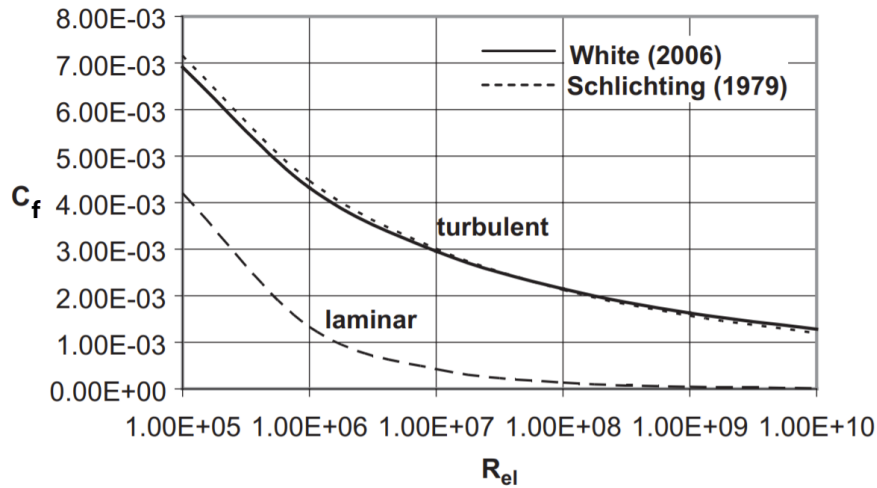


FIGURE 2.2: Dependence of skin-friction coefficient on Reynolds number on flat plate boundary layer (Sforza, 2014)

### 2.1.1 Parametrization of the Boundary layer

Parametrizing a boundary layer is of paramount importance, as it allows researchers to distinguish between two fundamentally different regions: one closer to the wall, where viscosity dominates, and another further away where inertial forces are more important. At any downstream location

$x$ , the parametrization and scaling of the boundary layer divides the velocity field  $u(x, y)$  into an inner region where the kinematic viscosity  $\nu$  is a parameter, an outer region where it is not and an overlap of the two where the velocity depends logarithmically on the wall normal distance  $y$ . Furthermore, the inner region is subdivided into three layers and the outer one into two - with the "upper"-most inner layer and lower-most outer layer being shared as the logarithmic layer. A quantitative definition of these four layers is

$$\begin{array}{l} \text{Inner Region} \left\{ \begin{array}{ll} \text{Viscous Sublayer: } 0 < y^+ < 5 & u^+ = y^+ \quad (2.7) \\ \text{Buffer layer: } 5 < y^+ < 30 & u^+ = f_1(y^+) \quad (2.8) \end{array} \right. \\ \text{Outer Region} \left\{ \begin{array}{ll} \text{Logarithmic layer: } 30 < y^+ < 0.2\delta^+ & u^+ = \frac{1}{\kappa} \ln(y^+) + B \quad (2.9) \\ \text{Wake layer: } 0.2\delta^+ < y^+ & U_\infty - u = f_2(y/\delta) \quad (2.10) \end{array} \right. \end{array}$$

where  $f_1$  and  $f_2$  are empirical functions,  $\kappa$  is the von Karman constant (0.387 for the purpose of this work according to Marusic et al. (2010)) and  $B$  is the wake-intercept parameter (4.2).

In the inner region of the boundary layer,  $u$  and  $y$  are rendered dimensionless with the velocity and length scales defined using the viscosity, wall shear stress  $\tau_w$  and density  $\rho$ . These are the friction velocity

$$u_\tau = \sqrt{\frac{\tau_w}{\rho}} = \sqrt{\nu \left( \frac{\partial \bar{u}}{\partial y} \right)} \quad (2.11)$$

and the viscous lengthscale  $\delta_\nu$

$$\delta_\nu = \nu \sqrt{\frac{\rho}{\tau_w}} = \frac{\nu}{u_\tau} \quad (2.12)$$

Following standard notation, all the variables and parameters made dimensionless with these inner scales are marked with the superscript "+", so for example the wall units  $y^+$

$$y^+ = \frac{y}{\delta_\nu} = \frac{y u_\tau}{\nu} \quad (2.13)$$

In the outer region, the boundary layer thickness  $\delta$  replaces  $\delta_\nu$  in the scaling - this disparity between the inner and outer layer scaling is the reason for the existence of the logarithmic layer (Eq. 2.9) where the two regions overlap.

An important parameter that will be used throughout this study, as well as in most of the current literature about wall-bounded turbulent flows, is the friction Reynolds number. This quantity represents the outer length scale divided by the inner length scale.

$$Re_\tau = \frac{\delta}{\delta_\nu} = \frac{u_\tau \delta}{\nu} \quad (2.14)$$

The sublayers of the boundary layer are depicted in Figure 2.3 using a log-linear axis scaling and law-of-the-wall normalization for the parameters. Note that the Reynolds numbers used in this plot are very high, much higher than any that will be considered in this study. The consequence of this is that the logarithmic layer is extended, spanning multiple orders of magnitude in terms of  $y^+$ . This won't be the case in the current work, where the logarithmic layer will be less discernible.

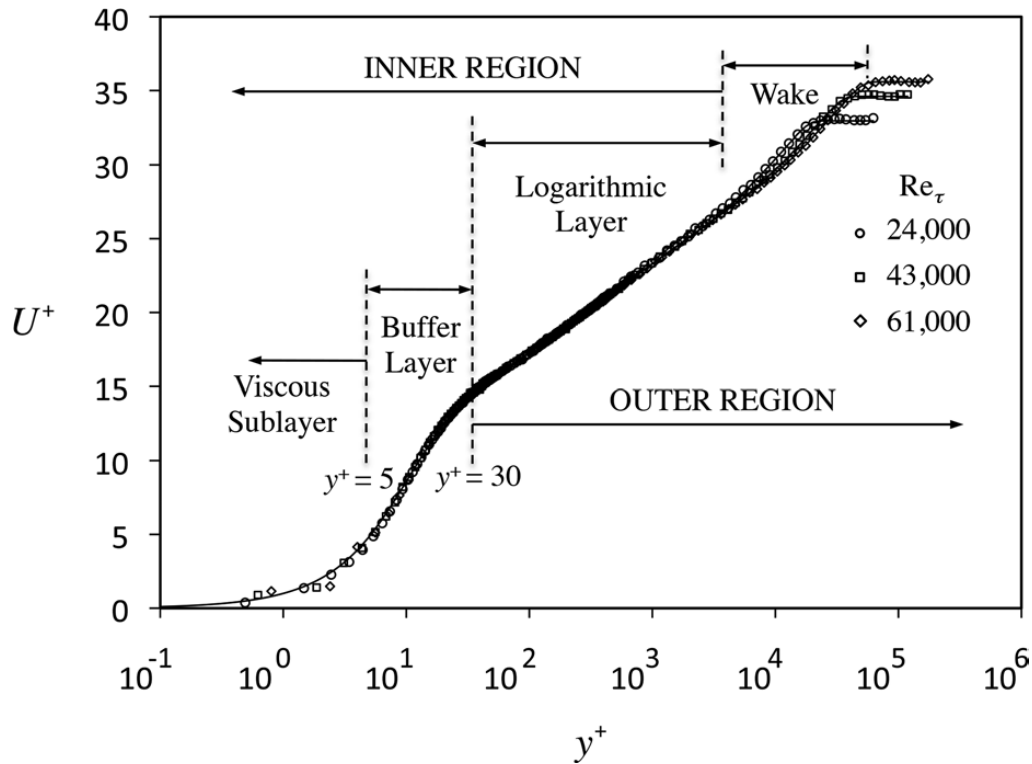


FIGURE 2.3: Mean Velocity profile of smooth plate turbulent boundary layer with wall normalizations and plotted in log-linear axis (adapted from Perlin et al. (2016) and data from Oweis et al. (2010))

## 2.2 Turbulence Cascade and Production

So far there has been a review of TBL fundamentals only in terms of mean quantities. However, turbulent flows are composed of random and chaotic fluctuations superimposed on the mean flow. This section will therefore differentiate these random components from the mean flow velocity, and review TBL fundamentals focusing on those.

Here we can define the instantaneous turbulent velocity component as the difference between the instantaneous and mean velocities, in a process known as Reynolds decomposition. This decomposition is extremely important for statistical analysis of a TBL, and defines the fluctuating part of the velocity as

$$u' = u - \bar{u} \quad (2.15)$$

A fundamental concept within the study of turbulence is the turbulent energy cascade. The idea of the turbulent energy cascade is that kinetic energy is fed by external forces and excites the largest possible eddies, entering the turbulence cycle. This energy is then passed down to smaller and smaller scales, until, at the smallest scales, it is finally dissipated by viscous actions.

Richardson (1922) argued that the largest eddies (which will be discussed more in depth in Section 2.3.2 below) are unstable and break up, transferring their energy to smaller eddies. These break up in similar fashion, continuing the cycle (or cascade) until the Reynolds number of the smallest eddies is sufficiently small that molecular viscosity is effective in dissipating the kinetic energy. In this classical model for turbulent cascade, the energy and momentum in wall bounded flows are transported from the largest scales to the smallest ones with the range of scales spanned by the cascade depending on  $y^+$  (Jimenez, 2012).

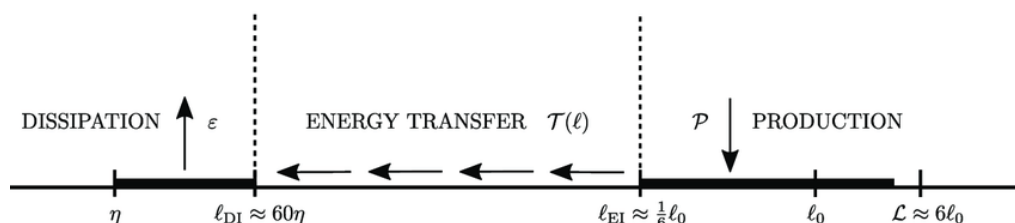


FIGURE 2.4: Schematic Diagram of the energy cascade at high Reynolds numbers. Adapted from Pope (2001)

In Figure 2.4, a schematic of the energy cascade is shown. The energy transfer happens between lengthscales  $\ell_{EI}$  and  $\ell_{DI}$ , limiting the inertial subrange. Here  $\ell_{EI}$  is the demarcation lengthscales between the energy containing range of eddies and the smaller eddies, and  $\ell_{DI}$  is a similar demarcation between the dissipation range and the inertial subrange. The dissipation range is on one side of this spectrum, while the energy containing range is found on the other side containing the largest eddies (of scale  $\ell_0$ ) and terminating below the flow scale  $\mathcal{L}$ .

The production of turbulent kinetic energy is defined using the fluctuating velocities described above, with the following equation

$$\mathcal{P} = -\overline{u'_i u'_j} \frac{\partial u'_i}{\partial x_j} \quad (2.16)$$

The dissipation is similarly

$$\varepsilon_k = \nu \overline{\frac{\partial u'_i}{\partial x_j} \frac{\partial u'_i}{\partial x_j}} \quad (2.17)$$

In these equations, the product  $\overline{u'_i u'_j}$  represents the Reynolds stresses, another concept key to the understanding of turbulence.

Dividing the flow into three regions makes it possible to discuss various statistics related to Reynolds stresses using a DNS study on a turbulent channel flow by Kim et al. (1987).

Within the log-region ( $50 < y^+ < 120$ ) of this boundary layer the normalized Reynolds stresses  $\langle u_i u_j \rangle / u_\tau^2$  and the production to dissipation ratio  $\mathcal{P} / \varepsilon$  are essentially uniform. With the production and dissipation almost in balance, the viscous and turbulent transport of the turbulence kinetic energy  $k$  is very small in comparison.

A detailed overview of the Reynolds stresses is shown in Figure 2.5, where they are plotted on a semi-log axes. The streamwise Reynolds stresses, and consequently the turbulent kinetic energy, have their peak in the buffer layer around  $y^+ = 12$ . At this peak, the production is about 1.8 times the dissipation, with the excess energy produced being transported away. It has been shown in multiple studies (Harder and Tiederman, 1991; Choi et al., 1998; Fukagata et al., 2002; Kempaiah et al., 2020) that the peak in normal stresses  $\langle u'u' \rangle$  and  $\langle v'v' \rangle$  as well as the shear stress  $\langle u'v' \rangle$  has to decrease in order to have a skin-friction drag reduction.

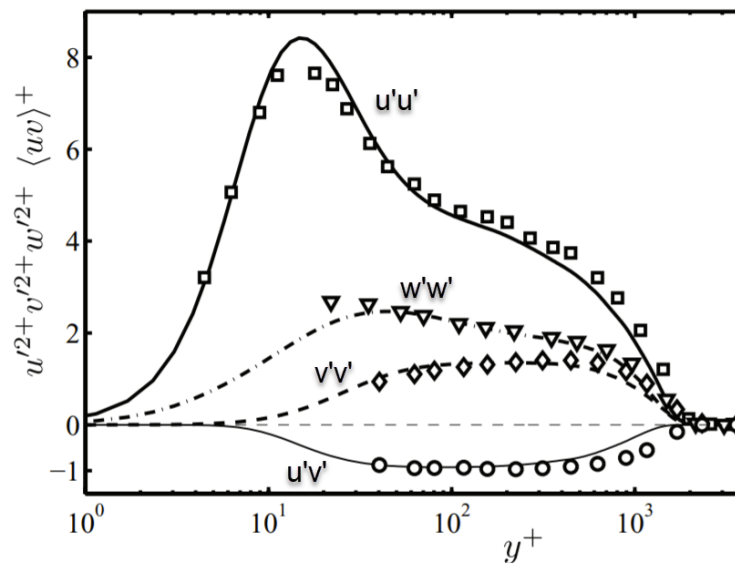


FIGURE 2.5: Labelled Reynolds stresses at  $Re_\theta = 5230$ , adapted from Sillero et al. (2013). Symbols are an experiment from Osaka et al. (1998)

### 2.3 Coherent Structures in Boundary Layers

Over the past few decades, the view that turbulence is a random phenomenon superimposed over a mean flow has shifted with the realization that quasi-period, large scale vortex motions dominate the transport properties of turbulent flows (Robinson, 1991; Barthlott and Fiedler, 2003). Despite the extensive work in this area it is rather difficult to describe these precisely. As such, the main idea is that there exist regions of space and time significantly greater than the smallest scales, where there are characteristic coherent patterns present within the flow, defined as a variable correlating with itself or another (Pope, 2001).

Robinson (1991) classifies these quasi-coherent structures in eight different categories, defined as follows:

- low speed streaks
- ejections of low speed fluid away from the wall
- sweeps of high speed fluid towards the wall
- vortical structures of several forms
- strong internal shear layers within the wall zone
- near wall pockets visible as regions clean of marked near-wall fluid
- shear layers of large outer region motions, consisting of  $\delta$ -scale discontinuities in the stream-wise velocity
- large scale motions in the outer layers

Despite all these categories, the apparent randomness of the flow field comes also due to the random size and intensities of the various kinds of organized structures within the field itself (Gad-El-Hak, 2019).

The challenge then is to identify these coherent structures either with a visual impression of the flow or in an instantaneous velocity or pressure signal. An added challenge is that the large eddies, being the same scale as the flow, are not universal - making it hard to develop a coherent theory for them. In wall bounded flows, for example, a multiplicity of coherent structures have been identified mostly through flow visualization experiments. The simplest of these structures are steady and quasi-steady patterns of vortices travelling near the wall, while more complex structures display the bursting dynamics described more in depth in the following section (Graham and Floryan, 2021).

### 2.3.1 Inner Layer Structures

Numerous flow visualization experiments, in particular those of Kline et al. (1967) and Smith and Metzler (1983), have identified streaks in the near wall region,  $y^+ < 40$ . The aforementioned researchers used hydrogen bubbles in a turbulent boundary layer to observe a well-organized motion in the near-wall region - specifically, they found an accumulation of alternating high- and low-speed regions aligned in the streamwise direction. These streaks, shown in Figure 2.6, are spaced randomly between 80 and 100 viscous lengthscales independently of the Reynolds number. Their length in the streamwise direction can reach and exceed  $1000\delta_v$ .

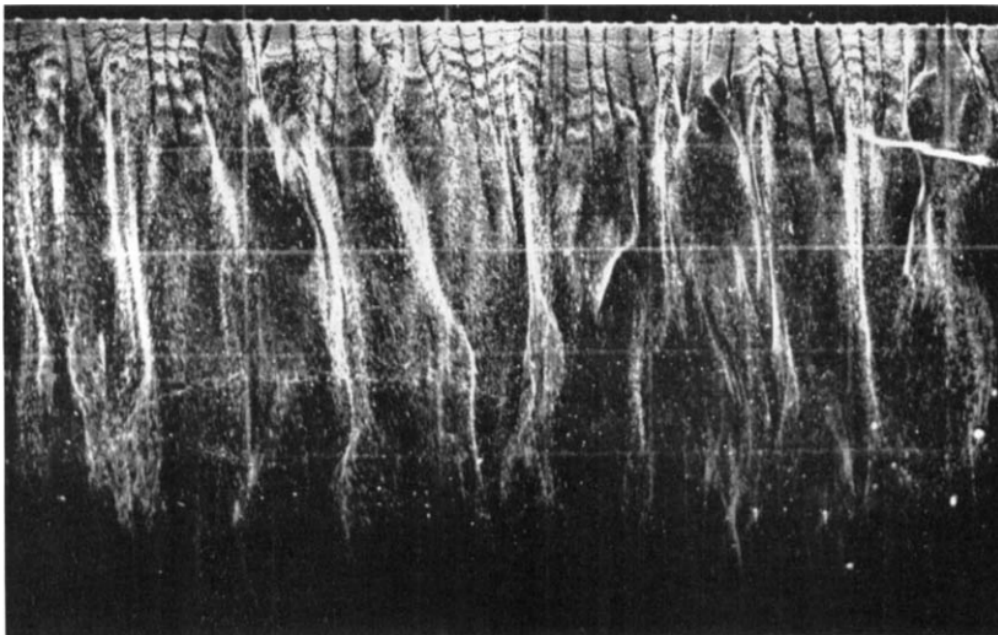


FIGURE 2.6: Streaks at  $y^+ = 4.5$  (Kline et al., 1967)

The streaks themselves correspond to a relatively slow moving fluid with about half of the local mean streamwise velocity, while the flow between them is relatively fast moving, and they display a characteristic behaviour known as bursting. This behaviour was studied in depth by Blackwelder and Eckelmann (1979), who investigated how with increasing downstream distance the streaks tend to move slowly away from the wall. At some point, typically around  $y^+ = 10$ , they rapidly move away from the wall in a process known as streak lifting or ejections. As it lifts, the streak oscillates rapidly and proceeds to breakdown into finer scale motions.

Corino and Brodkey (1969) further identified regions of fluid moving at high speed towards the wall, thereby satisfying continuity with the streaks. They called these regions sweeps, and proceeded to study how they contribute to the production of turbulent kinetic energy.

To do this, they divided all fluctuating velocities into four different quadrants divided by two axis: one for positive and negative  $u'$  and the other for positive and negative  $v'$ . This quadrant decomposition is represented in Figure 2.7 below, with labels for ejections and sweeps in quadrants 2 and 4, respectively. Wallace et al. (1972) further reviewed this, and called the motions in quadrants 1 and 3 outward and inward interactions, for lack of a more descriptive term.

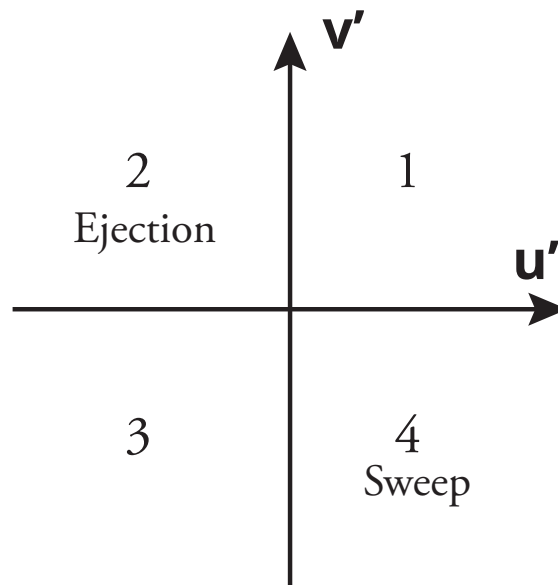


FIGURE 2.7: The  $u - v$  sample space showing the numbering of the four quadrants, with labelled sweeps and ejections.

As discussed, sweeps correspond to a high speed  $u'$  velocity fluctuation and a low speed  $v'$  fluctuation meaning that flow moves in the streamwise direction but towards the wall. Ejections, on the other hand, have a high speed  $v'$  fluctuation and a low speed  $u'$  one, meaning that they move away from the wall relatively fast to how they move in the streamwise direction. In quadrants 2 and 4 the product of the fluctuations is negative, meaning that overall they have a positive production of turbulence energy (recall Eq. 2.16).

Furthermore, near the wall ( $y^+ < 15$ )  $Q_4$  motions contribute considerably more to the turbulent shear stresses than  $Q_2$ , with the trend inverting further away from the wall (Wallace, 2016).

### 2.3.2 Outer Layer Structures

In the outermost layers of the TBL the flow is intermittent, with the coexistence of multiple scales and types of structures rendering the structure of the flow much more complicated to dissect. The streamwise streaks, for example, are now much larger with widths increasing up to  $z^+ \approx 3000$  and crossing the entire simulation domain studied by Jimenez (2013). The vortical structures, defined in more detail in a later section, also become more isotropic - making it extremely hard to discern particular orientations of geometries. Furthermore, at higher Reynolds numbers where the lengthscale range is largest, the larger structures start dominating the flow and superimposing themselves over the smallest scales (Marusic and Adrian, 2012).

However, something consistent across most turbulent boundary layers is the presence of a thin turbulence front known as the viscous superlayer, separating the turbulent boundary layer flow from the irrotational free stream fluid. This viscous superlayer has large scale characteristics best

viewed with flow visualization techniques such as those from Falco (1977), where the location of this superlayer can be inferred from the boundary of a smoke-filled region.

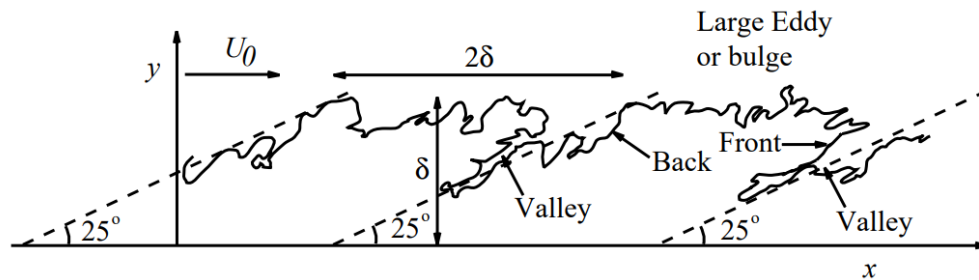


FIGURE 2.8: Vectorized drawing of the viscous superlayer from Falco (1977), (Pope, 2001)

Some features have been quantified in a number of experiments, such as those from Blackwelder and Kovaszny (1972) and Murlis et al. (1982). The researchers showed that, for a given stream-wise location, the  $y$  location of the superlayer is normally distributed with mean  $0.8\delta$  and standard deviation  $0.15\delta$ .

Furthermore, valleys of non-turbulent fluid have been shown to creep deep into the boundary layer, separating the large eddies inclined at a characteristic angle of  $20 - 30^\circ$ . These eddies, or bulges, are typically  $\delta$  to  $3\delta$  long in the streamwise direction and about half that size in the wall-normal direction. As they are convected downstream they slowly rotate in the streamwise direction and their large scale behaviour is fully characterized by the outer scales.

### 2.3.3 Vortical Structures within the TBL

Vorticity plays a paramount role in the understanding of phenomena occurring within the turbulent boundary layer.

One of the most important breakthroughs in understanding TBL vorticity was made by Theodorsen, who first proposed the horseshoe vortex structure, a hairpin-like loop. Theodorsen (1955) visualized a vortex filament oriented spanwise to the mean flow and perturbed upwards by a small motion. The “head” of this filament, laying higher from the wall, would experience a higher velocity and be dragged faster downstream. This would stretch the “legs” of the hairpin, causing the vortex to lift away from the wall into even higher mean velocity. The Theodorsen view of the hairpin is shown in Figure 2.9a

Some forty years later, Robinson’s DNS study (Fig. 2.9b) confirmed the existence of these large structures, with both arches and quasi-streamwise structures being observed. The advent of Particle Image Velocimetry furthermore showed that hairpins occur most often in packets, features where individual hairpins are travelling with nearly equal velocities to their neighbours (Adrian, 2007).

In an attempt to explain the creation of turbulent structures, Head and Bandyopadhyay (1981) suggested that larger structures can be composed by ensembles of hairpin vortices. This was further elaborated on by Perry and Chong (1982) and Marusic and Perry (1995), demonstrating that various measured statistics in boundary layers can be explained by a suitable distribution of elemental vortical structures such as these. Furthermore Pirozzoli et al. (2010) showed that at higher Reynolds numbers the flow in the layers closer to the wall consists of “vorticity tongues” that are more elongated than normal hairpins. The general hairpin geometry therefore does not change with Reynolds number, but the higher convective flow speeds drag the head further.

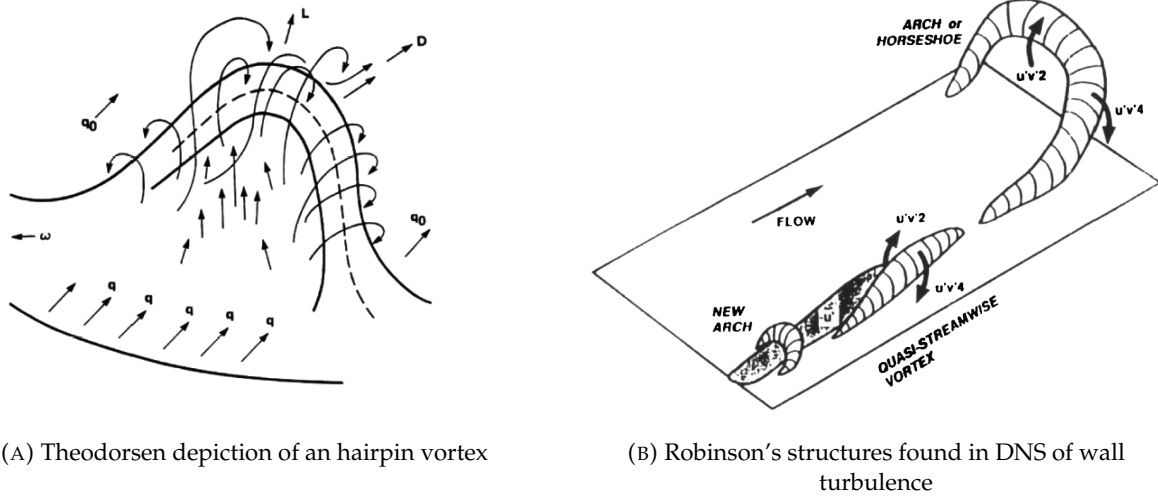


FIGURE 2.9: Different hairpin geometries and structures, adapted from Adrian (2007)

## 2.4 Mechanisms of Friction Drag Generation and Reduction

According to Adrian (2007), low-speed streaks in the buffer layer are critical in governing skin-friction and producing turbulent kinetic energy, as they are the dominant mechanism in the region where, at low Reynolds numbers, most of the velocity changes happen. Blackwelder and Eckelmann (1979) studied how a momentum defect was present in the flow between vortices nearby the wall, as low speed fluid was moved away from the wall in a long and narrow region. As such, reducing the streaks' intensity would be an approach to reduce turbulent skin-friction drag. Moreover, a turbulent flow is an excellent conductor of momentum. Such a flow is characterized by a very large friction coefficient, and as such drag can also be reduced targeting this. Recall the definition of skin-friction coefficient, now given in a slightly different form

$$C_f = \frac{\tau_w}{\frac{1}{2}\rho U_\infty^2} = \frac{2\nu}{U_\infty^2} \left[ \frac{\partial \bar{U}}{\partial y} \right] \quad (2.18)$$

where  $\bar{U}$  is the time average velocity component in the streamwise direction. This implies that reducing the mean-velocity gradient at the wall, or making the curvature of this profile as positive as possible, is a brute force but effective method of reducing drag.

### 2.4.1 Linking Turbulent Fluctuations to Friction Drag

The Fukagata, Iwamoto & Kasagi (FIK) identity, postulated by Fukagata et al. (2002), derives a simple and direct relationship between the Reynolds stresses to the skin-friction coefficient in the three canonical turbulent flows. For turbulent boundary layers, this relation is expressed as

$$C_f = \frac{4(1 - \delta_d)}{Re_\delta} + 2 \int_0^1 2(1 - y)(-\overline{u'v'})dy - 2 \int_0^1 (1 - y)^2 \left( \bar{I}_x + \frac{\partial \bar{U}}{\partial t} \right) \quad (2.19)$$

with the assumptions of constant free stream velocity and homogeneity in the spanwise direction - assumptions that are valid more often than not in zero pressure gradient boundary layer flows.

Furthermore, the term  $\bar{I}_x$  is defined as

$$\bar{I}_x = \frac{\partial(\overline{uu})}{\partial x} + \frac{\partial(\overline{uv})}{\partial y} - \frac{1}{Re_b} \frac{\partial^2 \bar{u}}{\partial x^2} \quad (2.20)$$

and the term  $\delta_d$  is the displacement thickness (Eq. 2.2) normalized by the boundary layer thickness. Several interesting takeaways can be made from Equation 2.19, not last how the magnitude of the skin-friction coefficient is not directly dependent on the Reynolds stresses but varies with wall distance. However, decreasing the Reynolds stresses would still be yet another approach at decreasing the skin-friction exerted on the wall.

## 2.5 Reynolds Number Effects

Despite extensive study of the canonical turbulent boundary layer, significant questions remain about the Reynolds number scaling in zero-pressure-gradient boundary layers on a flat plate.

The Reynolds number at which large scale engineering applications operate can be orders of magnitude larger than the one that can be tested in experiments or numerical simulations. These large differences have the potential to make extrapolation from experimental data erroneous, and therefore investigations on Reynolds number effects are key in understanding the implications of scaling flow-controlling methods from the laboratory into practice.

Because of the expense of large scale facilities, as well as the difficulties in measuring high Reynolds number flows, the vast majority of experimental data available has been collected at low Reynolds numbers. Further to this, the high computational costs associated to direct numerical simulations (DNS) at high Reynolds numbers make it hard - if not impossible - to gather DNS data for flow velocities resembling those of large scale engineering applications, such as aircraft or maritime transport.

The investigations that can be performed are generally concerned with various physical parameters, ranging from the aerodynamic drag measured to how the turbulence intensities scale with external flow speed.

### 2.5.1 Experimental Research

For the following sections, it is important to recall the definition of the friction Reynolds number

$$Re_\tau = \frac{u_\tau \delta}{\nu} \quad (2.21)$$

as well as the momentum Reynolds number

$$Re_\theta = \frac{U_\infty \theta}{\nu} \quad (2.22)$$

where  $\theta$  is the momentum thickness. Empirically defined relationships exist between the friction and the momentum Reynolds numbers, however this report will refer only to the friction Reynolds number unless indicated.

DeGraaff et al. (1998) used a low-speed but high Reynolds number facility to measure Reynolds stresses on a flat plate turbulent boundary layer, for momentum thickness Reynolds numbers ranging from  $Re_\theta = 1430$  to  $Re_\theta = 31000$

The question the authors attempted to answer was whether the log-law (Eq. 2.9) is truly independent from the Reynolds number, or whether a power-law with Reynolds number dependence

would be more correct. Laser-Doppler Anemometry showed that the mean streamwise velocity data collapsed in the sublayer, keeping the total shear stress near the wall near unity. This proved that the log-law works rather well even at higher Reynolds numbers.

Osaka et al. (1998) further experimented to verify the Reynolds number independence of the von Karman constant  $\kappa$  and the wake parameter  $B$ . The von Karman constant was proven to remain constant at 0.41 down to  $Re_\theta = 840$  and all the way to the top of the range at  $Re_\theta = 6220$ ; this implies that the slope of the logarithmic layer remains constant throughout the entire Reynolds number range, supporting the previously mentioned research by DeGraaff et al. (1998). The wake parameter, however, increases as the Reynolds number decreases and asymptotes at 0.62 for sufficiently high Reynolds numbers.

In a test campaign specifically dedicated to smooth plate turbulent boundary layers, Oweis et al. (2010) tested momentum thickness Reynolds numbers reaching up to  $\mathcal{O}(10^5)$ . Using the largest possible plate fitting into the (currently) largest low-turbulence tunnel, the researchers measured various TBL parameters such as skin friction and mean streamwise velocity. The main takeaway from this study was that the traditional scaling for turbulent boundary layers, as well as the Reynolds number dependence for profiles shown by Monkewitz et al. (2007), are sufficient to fit the data collected for  $Re_\theta$  up to 156000.

Smits et al. (2011) built upon the reviews by Gad-el-Hak and Bandyopadhyay (1994), Klewicki (2010), and Fernholz and Finley (1996) and many others to review the current understanding of high-Reynolds number turbulent flows, specifically for zero-pressure-gradient flat plate boundary layers. In traditional theory the peak production of turbulent kinetic energy comes from the buffer layer, at a wall distance of (approximately)  $12y^+$ . What is often overlooked, however, is that the bulk production at high Reynolds numbers happens within the logarithmic region. When showing the turbulence production in pre-multiplied form - where equal areas represent equal production contributions - it appears clear that this production is shifted further and further away from the wall at higher Reynolds numbers. In Figure 2.10, The production  $\mathcal{P}$  is given as  $\mathcal{P} = -\overline{u'v'}^+ \frac{\partial U^+}{\partial y^+}$  and is estimated using Reynolds shear stress profiles given by Perry et al. (2002) and the law of the wall formulation for mean velocity. While it is still correct to say that at low Reynolds numbers the bulk of the production comes from near the wall, the production in the logarithmic region dominates at higher  $Re_\tau$  values, values usually more interesting for engineering applications. Smits et al. (2011) estimated the cross over point at which the contribution from the log-region is the same as the one from the near-wall-region to be around  $Re_\tau = 4200$ .

## 2.5.2 Structures and Self-Similarity

In Gad-el-Hak and Bandyopadhyay (1994) and Smits et al. (2011)'s reviews there has been a significant focus on organized motions within the turbulent boundary layer and how these motions vary with Reynolds number. Given that coherent structures are a key part in the understanding of boundary layers, it is reassuring that they appear to be robust enough features not to change dramatically with Reynolds number. Specifically the near-wall, low-speed streaks have been shown to remain relatively constant both in spacing and length throughout a range of Reynolds numbers by the flow visualization experiments performed by Klewicki et al. (1995) the results of which are shown in Figure 2.11. There is a remarkably similar position of data points both for time scales and streak spacing compared to low and extremely high Reynolds numbers.

Finally, it was reviewed that the classical structure of the inner and outer layers with overlap is still a robust representation for all but the lowest Reynolds numbers; the limit in accuracy is most often found in the measuring of the skin friction at the wall.

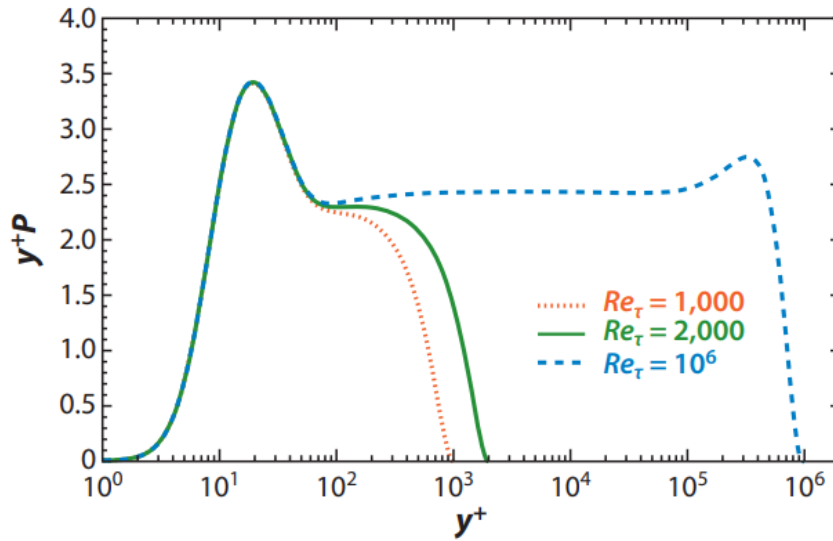


FIGURE 2.10: Pre-multiplied turbulence energy production. Adapted from Marusic et al. (2010) and Smits et al. (2011).

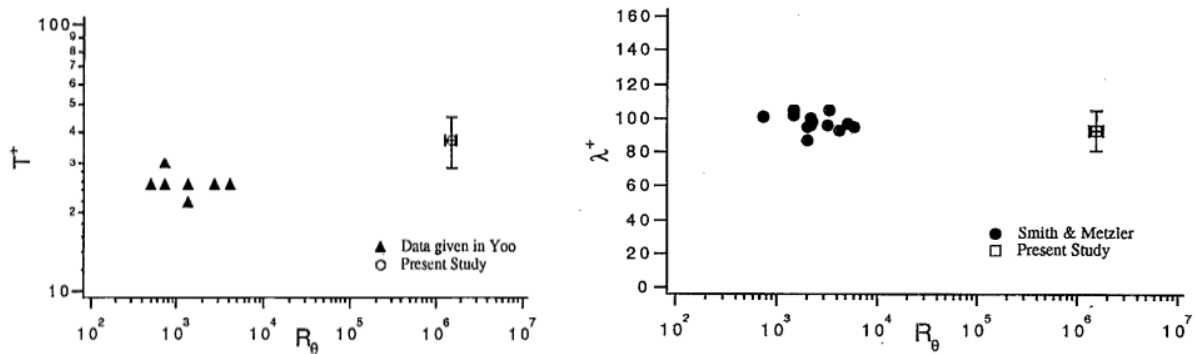


FIGURE 2.11: **Left:** Inner normalized time between pocket events  $T^+$  as a function of Reynolds number. **Right:** Inner normalized streak spacing  $\lambda^+$  versus Reynolds number. (Present study: Klewicki et al. (1995). Others: Yoo et al. (1991) and Smith and Metzler (1983))

In a study about wall turbulence at high Reynolds numbers, Marusic et al. (2017) noted that the interactions between the inner and outer layers are quite evident in the streamwise velocity fluctuations in the near wall region. The authors of this study described how the small scale turbulence within the inner region has its statistics described as a function of  $y^+$ , in a way that is consistent with the usual definition of near-wall turbulence. As  $Re_\tau$  grows however, the energy in the outer region grows as well. This superimposes the outer region fluctuations onto the near wall turbulence, making it so the peak variance of  $u'$  grows with Reynolds number. The separation of turbulence scales becomes larger, with the ratio of large to small scales increasing almost linearly with Reynolds number. This was also a result supported by Hutchins and Marusic (2007), who stated that the energy of large scale motions in the logarithmic region becomes more and more comparable to the energy in the near-wall layers as the Reynolds number increases. One of the main takeaways from this study was the existence of two different “inner” and “outer” energy sites, and that the Reynolds number determines how well these sites are separated. For example, at higher Reynolds numbers

it is well defined where the inner units are used as opposed to the outer units. As the Reynolds number decreases however, there is an increasing amount of overlap between these scales, until the physical dimensions of the inner and outer lengthscales are the same at a critical Reynolds number  $Re_\tau = 167$ .

## 2.6 Summary

This chapter opens up this work with a presentation of the fundamentals needed to gain good understanding of turbulent boundary layers. The various scaling parameters have been identified and discussed, alongside the parametrization of the boundary layer itself. Turbulence statistics such as Reynolds stresses and turbulent kinetic energy production have been introduced, and will be a key tool in analyzing the results. An introduction to structures within turbulent boundary layers has been made, with the key takeaway being that all the coherent structures within the turbulent boundary layer are interdependent: changes made either at the wall or at the larger outer scales will have effects on the other, and because of the lack of a general theory of turbulence, a complete understanding of all the interactions is still not possible as of today. Furthermore, it was shown how most of the friction drag generation comes from ejection and sweep events, where the product of the velocity fluctuations is negative. Turbulent skin-friction drag is therefore strongly connected to the dynamics of the turbulent structures and not just to their mean. Furthermore, there is plenty of evidence that these dynamics are dependent on the Reynolds number. It is therefore evident that when studying turbulent drag reduction the Reynolds number effect needs to be considered in designing the study and, most importantly, in interpreting the results.

## Chapter 3

# Turbulent Drag Reduction

Now that the boundary layer fundamentals have been introduced, and that some Reynolds number effects have been reviewed, it is necessary to delve into how these phenomena can be controlled in our favor. This chapter will deal with methods of drag reduction in turbulent flow, briefly talking about passive ones and then investigating active ones further. Special attention will be paid to oscillating walls, since these are directly relevant to the proposed control method in this thesis work.

In broad strokes, various flow control strategies can be utilized. These can be passive, requiring no power source and no control loop, or active, requiring some energy expenditure. The latter can be further divided into predetermined control or reactive control. These, respectively, describe the input of energy into the system as without regard for the system's state, or they adjust the input "smartly" based on sensor information. This kind of control is further divided into categories, each describing the type of closed loop control used.

On practical applications, drag is usually composed by pressure drag and friction drag. This work will focus exclusively on the latter, exploring drag reductions mechanisms to minimize the effect of friction forces.

### Contents

---

<b>3.1</b>	<b>Passive Methods for Drag Reduction</b>	<b>21</b>
3.1.1	Large Eddy Breakup Devices	21
3.1.2	Riblets	22
<b>3.2</b>	<b>Active Methods for Drag Reduction</b>	<b>23</b>
3.2.1	Wall Oscillations	23
<b>3.3</b>	<b>Reynolds Number Effects on Oscillating Walls</b>	<b>26</b>
<b>3.4</b>	<b>Spatial vs. Temporal Forcing</b>	<b>27</b>
<b>3.5</b>	<b>Industrial Readiness of TDR Techniques</b>	<b>27</b>
<b>3.6</b>	<b>Summary</b>	<b>28</b>

---

### 3.1 Passive Methods for Drag Reduction

Passive methods are defined as the ones that do not add mass, momentum and energy into the flow. They purely change the shape of the wall, or its chemical or mechanical properties. Once implemented, the drag reduction due to these methods will happen indefinitely at no extra energy cost. Other passive methods not discussed in this review include, but are not limited to, super-hydrophobic surfaces (Rothstein, 2010).

#### 3.1.1 Large Eddy Breakup Devices

Large Eddy Breakup devices (LEBUs), as the name suggests, are designed to modify and break-up the large vortices that form in the boundary layer's outermost layers. This off-surface design makes them somewhat unique, as they are designed to have no direct influence on the inner layer structures.

Typical LEBU arrangements consist in positioning them in a tandem configuration such as the one shown in Figure 3.1. In this position, they are able to inhibit wall-normal velocity fluctuations.

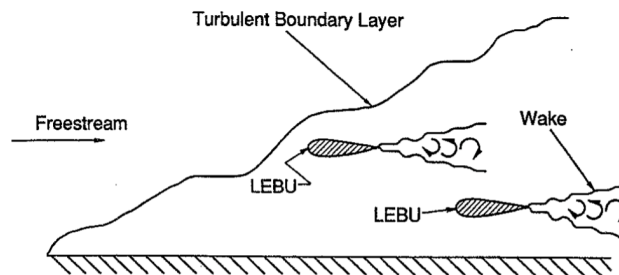


FIGURE 3.1: Sketch of tandem arrangement for LEBUs, from Gad-El-Hak (2000)

While it is relatively simple to reduce the skin-friction in a flat plate boundary layer by placing an obstacle above the surface, it is quite complicated to ensure that there is a net drag reduction: that is, the device's own pressure or skin-friction drag does not overcome the savings. Corke et al. (1980) performed several experiments on LEBUs, showing a net drag reduction of the order of 20%. This was achieved by two tandem elements spaced approximately  $\mathcal{O}(10\delta)$  apart, suppressing the large scale events happening in the outer regions of the boundary layer. Several other studies have been conducted, showing similar results for flat plate or airfoil-like shapes. The latter would offer several structural benefits extendable to real world applications (Gad-El-Hak, 2000), even though this method has not been expanded to large scale engineering yet.

Dowling (1985) performed an analytical study to understand the underlying mechanisms of LEBUs. His model showed that the vorticity shed from the trailing edge of the LEBU appears to cancel the effect of the incoming vortex and reduces the velocity fluctuations near the wall. Supporting this argument was the fact that the maximum local drag reduction took place where wall vortices reached the viscous sublayer. From this, it appears that although the method itself targets the outer part of the boundary layer, the drag reduction effect stems from physical phenomena happening within the viscous sub-layer. After this historical perspective, other methods discussed within this chapter aim at modifying and controlling the structures within the inner region of the turbulent boundary layer.

### 3.1.2 Riblets

Riblets are an interesting flow control method because they are the only ones that have been proven to work on real life engineering applications (so far) <sup>1</sup> after being adapted from swimming fishes and mammals. In a review of flow control on aspects of aquatic locomotion, Fish and Lauder (2006) found that riblets were one of the most effective methods for drag reduction.

Riblets are small wall grooves, typically aligned with the streamwise direction of the flow. Despite the increase in surface area, their small striations near the surface interact favorably with the near-wall structures in the turbulent boundary layer in order to produce a significant amount of drag reduction.

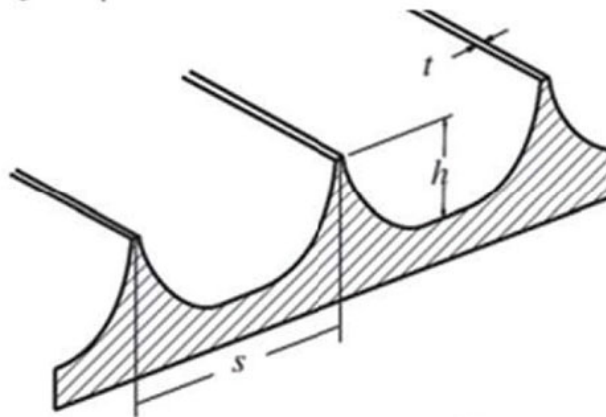


FIGURE 3.2: Generic scalloped riblet geometry (Adapted from Bilinsky (2017))

The most important parameters in the design of the riblets are the shown in Figure 3.2 above: the height  $h$  and the spacing  $s$ , rendered non-dimensional with inner units to obtain  $h^+$  and  $s^+$ . Studies have found that the optimal values are in the range  $h^+ = 8 - 12$  and  $s^+ = 15 - 20$  (García-Mayoral and Jiménez, 2011), corresponding to around 0.6 and 1.2 [mm] (respectively) for friction velocities around 0.200 [ms].

Walsh (1983) tested several shapes such as the one shown in Figure 3.2, and consequently his team found drag reduction possibilities of up to 8% for riblet spacing of approximately 15 wall units. In this experiment, riblets were found to be effective in the presence of both positive and adverse pressure gradients, having a gradual decrease in performance as flow conditions vary off-design. The percentage of drag reduction tapers to zero as the yaw angle of the flow is increased; surprisingly, after this reaches zero at around 30 degrees, the drag does not increase once yaw is increased (Gad-El-Hak, 2000).

There are several theories for why riblets are effective in reducing the mean-velocity gradient in the boundary layer. Riblets are thought to restrain the movement of the near wall longitudinal vortices, and therefore to maintain their coherence. Stabilizing these rolls prevents them from taking part in the energy cascade, and hence impede the rate of energy loss with consequent drag improvements. García-Mayoral and Jiménez (2011) argued that the vorticity present in the valleys of riblets interacts with the coherent streamwise vortices and weakens them, reducing their intensity. Similarly, Lumley and Kubo (1985) stated that the streamwise vortices near the wall are forced to negotiate with the sharp peaks of the riblets, causing energy losses. Therefore, to remain in equilibrium, the eddies must increase their energy gain by growing larger. The larger scales result in secondary instabilities and sharp changes in mean velocity slope occurring farther away from the wall. For the

<sup>1</sup>See <https://www.nasa.gov/centers/langley/news/factsheets/Riblets.html>

same friction velocity then, the mean velocity itself is higher thus reducing the skin-friction. Velocity contours showing vortical structures being trapped within the riblet valleys is shown in Figure 3.3 below, taken from an experimental study by El-Samni et al. (2007). Overall, it is clear from the review that riblets produce their drag reduction by inhibiting the vortical structures within the inner layers of the boundary layer. Given that this is a method tested and proven in engineering applications, the suppression of the low-speed streaks is brought to the forefront of desirable effects of turbulent drag reduction techniques.

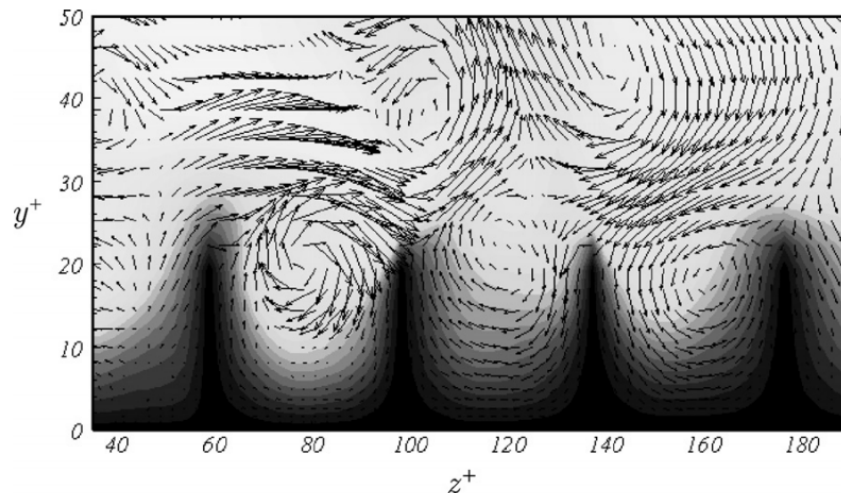


FIGURE 3.3: Velocity contours showing vortical structures within the riblet valleys, from El-Samni et al. (2007)

## 3.2 Active Methods for Drag Reduction

Active methods involve some sort of input to the flow, be it mass, momentum or energy. Unlike passive methods, active flow control changes the properties of the boundary layer only intermittently, either through a control system loop or at predetermined times. With active techniques for drag reduction, it is very important also to consider the power spent on the flowfield changes, as the net power saved will then determine whether the system is worthwhile or not. Other active methods not mentioned in this work include, but are not limited to, plasma actuators (Corke et al., 2010; Cattafesta and Sheplak, 2011), polymer injection (Berman, 1978; White and Mungal, 2008), synthetic jets (Glezer and Amitay, 2002) and porous wall blowing (Antonia et al., 1995).

### 3.2.1 Wall Oscillations

Wall oscillations methods have received much attention in recent times, with the most recent and comprehensive review presented by Ricco et al. (2021). The foregoing gives a concise presentation on the concept.

After several early studies of turbulent boundary layers subjected to spanwise pressure gradients (Bradshaw and Pontikos, 1985; Driver and Hebbar, 1987), Jung et al. (1992) showed with a numerical study that significant reductions in drag can be achieved via an unsteady transverse motion of the wall. This motion involves oscillating the wall sideways, in the direction normal to where the boundary layer develops.

The sinusoidal wall oscillations first considered by Jung et al. (1992) are defined by the displacement

$$z = A_{osc} \sin(\omega t + \phi) \quad (3.1)$$

where  $z$  is the location on the oscillating plate,  $A_{osc}$  being the amplitude of oscillation and  $\omega$  and  $\phi$  being the angular velocity and phase difference, respectively. The time period of the oscillation is naturally given by  $2\pi/\omega$ , and is the second of the two parameters governing the system.

The time period and the amplitude can be rendered non-dimensional by scaling them with inner units, resulting in the following parameters:

$$T_{osc}^+ = \frac{Tu_{\tau}^2}{\nu} \quad (3.2)$$

$$A_{osc}^+ = \frac{Au_{\tau}}{\nu} \quad (3.3)$$

Following the initial study by Jung et al. (1992), an experimental study by Laadhari et al. (1994) showed that the mean streamwise velocity profile for the oscillating wall is reduced compared to baseline cases, decreasing further with an increase in frequency of wall oscillations. Furthermore, the Reynolds stresses also behaved in a similar pattern, making all these experimental observations agree with the initial findings by Jung et al. (1992).

In a following study specifically aimed at experimentally confirming the findings from Jung et al. (1992), Choi et al. (1998) measured the skin-friction drag coefficient to show a reduction of up to 45% near the wall for up to  $5\delta$  downstream of the start of the oscillation. The above experiments were setup similarly to the one shown in Figure 3.4, with a plate in an enclosed channel being oscillated by a crankshaft system. Limitations of this setup include the frequency of the oscillations, which is restricted by the inertia of the plate itself.

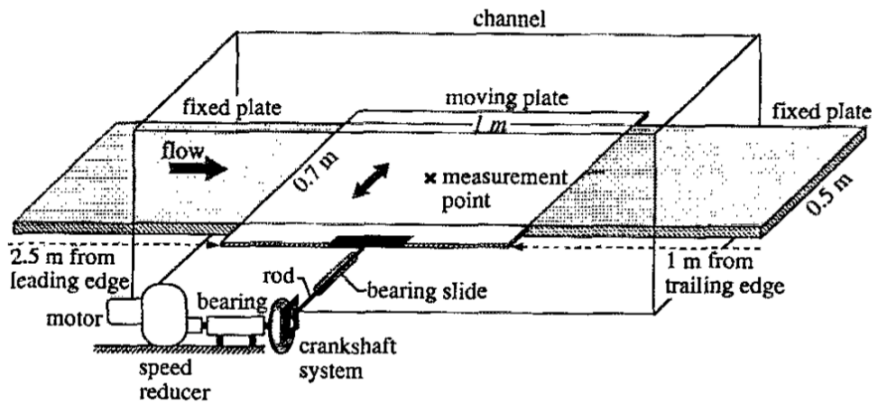


FIGURE 3.4: Setup of an oscillating wall experiment, by Laadhari et al. (1994)

In order to investigate the limits of this technique, Quadrio and Ricco (2004) performed a parametric DNS study at a friction Reynolds number  $Re_{\tau}$  of 200, resulting in a map like Figure 3.5. Here,  $W^+$  is the non-dimensional wall boundary condition for the spanwise velocity,

$$W = W_m \sin\left(\frac{2\pi}{T}t\right) \quad (3.4)$$

The plot shows the drag reduction dependency on the two non-dimensional parameters of the oscillation. The hyperbolae in the plane are lines of constant maximum displacement of the wall, while the dashed line is the optimum period curve for a fixed displacement. The investigation

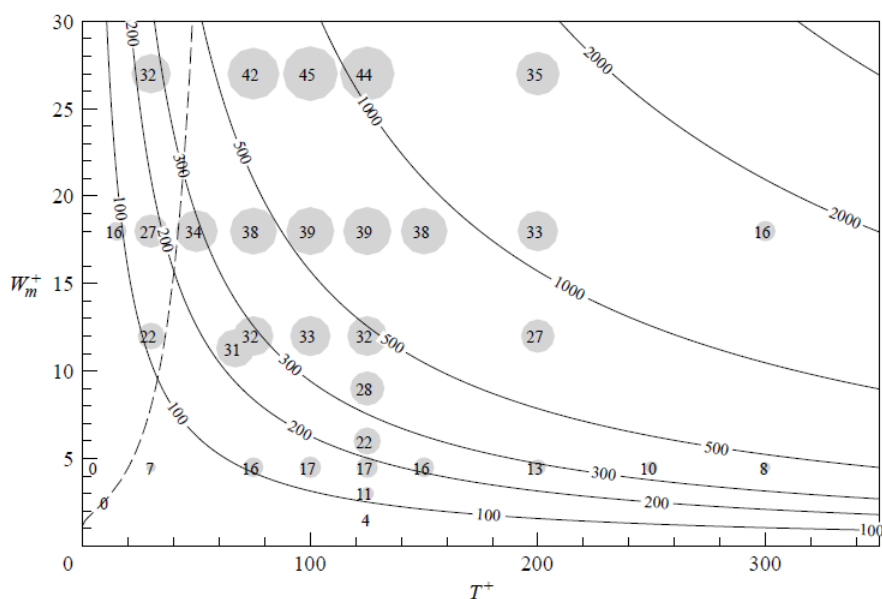


FIGURE 3.5: Three dimensional plot of drag reduction (circle size) versus  $T^+$  and  $W_m^+$ .  
From Quadrio and Ricco (2004)

reveals that for a given value of  $W^+$ , the drag reduction can be kept at a maximum by fixing  $T^+$  around the 100-125 range. Furthermore, for a fixed period of oscillation, the drag reduction appears to increase monotonically with  $W^+$ .

Laadhari et al. (1994) attempted to explain this reduction in drag with turbulence statistics, attributing it to the interaction between longitudinal vortices and the low speed streaks near the wall. Due to the oscillatory motion of the wall, the streamwise vortices are convected in the spanwise direction, breaking their coherence and thus reducing the turbulence production. This view was corroborated by Ricco (2004), whose simulations distinctly showed that the streaks are dragged laterally by the Stokes layer generated by the oscillating wall. Ricco's study built on Choi and Clayton (2001), also supporting the presence of a periodic Stokes layer, but arguing that this influences mostly the mean velocity gradient near the wall. A weakening of the near wall bursts was also noted, attributed to the spanwise convection of the streaks. In terms of parameters driving the drag reduction, Baron and Quadrio (1995) determined an optimum amplitude of  $T^+ = 100$  by observing that the oscillations of the plate generate a boundary layer equal to  $\delta^+ = \sqrt{(4\pi T^+)}$ . This boundary layer must embed as much of the streaks as possible, ideally without influencing the vortices.

To shed further light on the physical mechanisms behind the skin-friction drag reduction, Ricco et al. (2012) performed several DNS studies on harmonic wall oscillations. The channel flow used in these numerical simulations was driven by a constant pressure gradient to maintain an unambiguous inner scaling, and resulted in drag reduction manifesting itself as an increase of mass flow rate. From this study it emerged that the energy spent to drive the wall was almost the same as the viscous dissipation due to the oscillating layer, but only when looking at the global energy fluxes. Furthermore, the analysis of short-term evolution of the flow after the motion start-up shows that the near wall dissipative properties are responsible for the reduction in turbulence intensity. Ultimately, it would be interesting to explore the long term sustained effects of the wall oscillations on drag reduction.

Finally, through another experimental study, Kempaiah et al. (2020) stipulated that the reduction in near-wall vorticity, as well as the accompanying reduction of hairpins in a hairpin packet, is the key

to the skin-friction reduction. For this, the oscillation frequency might be associated with the size of the packet, while the oscillation amplitude needs to be as large as the streaks' spanwise spacing.

### 3.3 Reynolds Number Effects on Oscillating Walls

As a connection from Section 2.5, it is interesting to study the Reynolds number dependence of the skin-friction drag reduction when the latter is achieved through wall-oscillations.

The drag reduction rate is speculated to often decrease following a power law, in other words  $\mathcal{R} \sim Re_\tau^{-\gamma}$  with the exponent determined empirically. Ricco and Quadrio (2008) considered an oscillating wall for  $Re_\tau$  200 and 400 and determined  $\gamma$  to be 0.21 at the point of largest drag reduction. Similarly, Quadrio et al. (2009) for the above mentioned experiment calculated a  $\gamma$  of 0.24. And finally, Touber and Leschziner (2012) achieved  $Re_\tau$  values of up to 1000 and suggested  $\gamma = 0.20$ . Clearly the real value is somewhere between 0.2 and 0.25, but changing the parameters of the oscillation is enough to change this exponent. This was furthermore highlighted in a more recent study by Gatti and Quadrio (2013), who performed simulations at  $Re_\tau$  up to 2000 in very small domains. The dependence of  $\mathcal{R}$  on different Reynolds numbers is shown in Figure 3.6. While the data clearly presents a power law dependency, the exponent cannot be determined with high enough accuracy to make general conclusions.

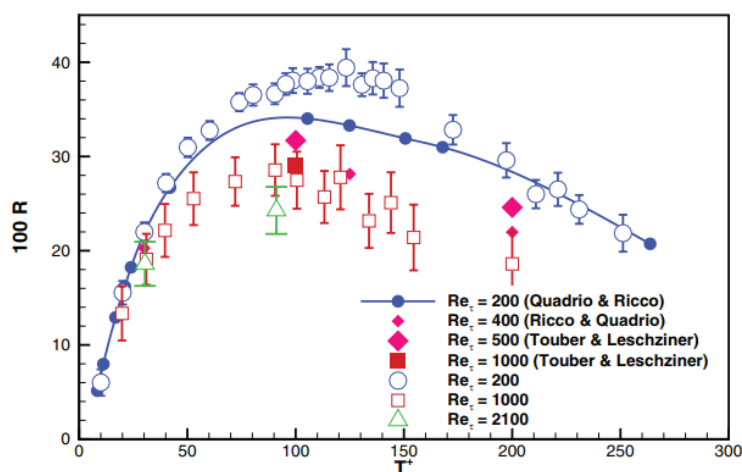


FIGURE 3.6: Percent drag reduction vs a-dimensional oscillation period for  $A^+ = 12$ . Adapted from Gatti and Quadrio (2013).

Most recently, Gatti and Quadrio (2016) performed a study to assess how increasing the value of  $Re_\tau$  (and therefore the impact on engineering applications for the method) affects the drag reduction created by spanwise forcing. Using the streamwise travelling waves of spanwise wall velocity from Quadrio et al. (2009), the authors performed a direct numerical simulation for  $Re_\tau = 200$  and  $Re_\tau = 1000$  of a turbulent channel flow. Gatti and Quadrio (2016) compared their results to those of various other studies and argued for some overarching trends. At low Reynolds numbers, all the studies agree with a maximum drag reduction for an optimal oscillation period of  $T^+ \approx 100 - 125$ . The magnitude of the drag reduction is also relatively constant throughout, at  $\mathcal{R} \approx 37.4\%$ . Both the optimal oscillation and the magnitude of drag reduction decrease with increasing  $Re_\tau$ , with the former being  $T^+ \approx 75$  and the latter  $\mathcal{R} \approx 27.7\%$ .

### 3.4 Spatial vs. Temporal Forcing

As a connection between oscillating walls and rotating discs, it is interesting to consider the comparison between spatial and temporal forcing made by Skote (2013). Consider a variation of Eq. 3.1, rewritten here as

$$W = W_m \sin(\omega t) \quad (3.5)$$

Instead of using an angular frequency  $\omega$  to define the wall oscillation, Skote (2013) used the wavenumber of the spatial oscillation  $\kappa$ , related to the wavelength via  $\kappa = 2\pi/\lambda_x$ . This turns the description of a wall oscillation into

$$W = W_m \sin(\kappa x) \quad (3.6)$$

converting the time-dependent forcing into a relatively unsteady interaction between the wall motion and the near-wall turbulence, like first described by Quadrio et al. (2009).

The wavenumber can then be related to the angular frequency through a convection velocity  $U_w$ , with the relationship  $\kappa U_w = \omega$ . Using two wall velocities for either temporal or spatial case, a net positive energy budget was achieved for a weaker wall velocity in both cases, while a higher wall velocity resulted in more energy required than saved (through drag reduction) for the spatial oscillations.

A comparison between Viotti et al. (2009) and Skote (2011) further showed that the drag reduction was higher in the spatial oscillation case than the temporal oscillation one. This greater drag reduction was attributed to the spanwise component of the Reynolds stresses, as this was the only component being considerably lower between the two cases. As a caveat however, in case of high wall velocities the power required for the spatial case is much higher than the drag save, rendering the method obsolete. The similarity between spatial and temporal forcing of the wall however could be exploited in more practical engineering applications; for example, Ricco and Hahn (2013) utilize rotating discs to produce spatial wave forcing instead of oscillating the whole wall. This has several beneficial effects, such as bypassing the problems related to the high oscillatory inertial of the wall, or increasing the compliance with engineering applications.

### 3.5 Industrial Readiness of TDR Techniques

It goes without saying that the overall goal of any drag reduction technique is to be applied to large scale engineering applications, generating monetary benefits to the user. This section will henceforth address how each of the techniques discussed in the previous sections address this ultimate need for the consumer.

Up to today, the only method that has been used in industrial applications are the riblets, albeit only at low Reynolds numbers. One reason for this single-product use might be that more interest is going into boundary layer transition delay mechanisms, which would ideally lead to greater savings across the field. However, on applications such as aircrafts, the critical transition Reynolds number is orders of magnitude smaller than Reynolds numbers experienced normally by aircraft (see previous sections), and as such turbulent drag reduction is clearly needed alongside transition delay mechanisms. Offering a perspective from Boeing, Spalart and McLean (2011) argued that the airliner industry is aware of the majority of currently-developed drag reduction methods but is hesitant of taking over development of any of them due to the lack of multi-disciplinary research; for example, the progress in material and manufacturing sciences is worth waiting for as it greatly impacts the performance of all methods considered.

Other problems with discussed techniques are in the complications arising from the use of control methods, such as increased weight from sensors and equipment, as well as the added energy

expenditure. Spalart and McLean (2011) bring this up as well, mentioning how active systems presented without mention of energy expenditure will be hard pressed to entice the management of whichever industry they are aimed at. The wear of components is also a clear downside to passive and active methods alike, with features such as riblets having to undergo thorough cleaning quite often (García-Mayoral and Jiménez, 2011) and suction and blowing micro-holes at risk of getting clogged by debris (Zhang et al., 2018). Oscillating walls on the other hand have their main drawback as the high oscillation frequencies needed for drag reduction at high Reynolds numbers. This, coupled with small and constantly moving mechanical parts results in a very impractical system for large scale engineering.

### 3.6 Summary

Several drag reduction methods have been discussed, classifying them into passive and active categories. After a brief historical perspective of a method targeting the larger outer eddies, it was reviewed how most (if not all) of these methods aim at targeting structures within the inner layers and reducing the Reynolds stresses. As mentioned, the primary structure to be suppressed to reduce the intensity of the turbulence production is the low-speed streaks in the near-wall region. This is achieved with various grades of success throughout the different methods, reflecting in their overall drag reduction. Out of all the drag reduction methods discussed in this and the previous chapter, oscillating walls have been shown to achieve the highest values of drag reduction. Several experimental campaigns and numerical studies have independently shown reductions in skin-friction drag around 45%, with most of the researchers agreeing to the generation of a Stokes layer as the primary cause of this reduction. Finally, the industrial readiness of the above-mentioned drag reduction techniques has been reviewed and put into question. Some if not most all of the techniques mentioned have fundamental engineering limitations that cannot be easily solved, putting their usefulness outside laboratory settings into question. In the following chapter, a novel active drag reduction method will be introduced - a flush mounted array of rotating discs. This method can be adapted to virtually any Reynolds number by changing the spinning velocity of the discs, and can be optimized for a certain engineering application by prescribing an ideal disc diameter. Most importantly, it targets the same turbulent vortical structures that are now proven to lead to reductions in skin-friction drag.

## Chapter 4

# Rotating Discs

Despite the large drag reduction and net power savings, spanwise forcing of a wall is not a practical method of turbulent drag reduction in engineering applications due to the extremely high oscillation frequencies, approximately 15kHz for an airliner cruising at  $225 \text{ ms}^{-1}$ , as well as the high inertia of the oscillating plate.

To overcome the motion of the plate, a novel concept proposed by Keefe (1997) involved a matrix of flush-mounted discs, spun in such a way that effectively a spanwise wave was induced at the wall. Ricco and Hahn (2013), Wise and Ricco (2014), and Olivucci et al. (2019) expanded upon this concept using high fidelity numerical simulations, arguing that this array of discs would be much more feasible for engineering applications, as the discs could be spun arbitrarily fast without inertial limitations such as the ones in oscillating walls.

### Contents

---

4.1	Normal Vorticity Actuators . . . . .	30
4.2	Rotating Discs for Friction Drag Reduction . . . . .	30
	4.2.1 Flow Structures and Drag Reduction Mechanisms . . . . .	32
4.3	Disk Spacing . . . . .	33
4.4	Oscillating Discs . . . . .	35
4.5	Summary . . . . .	37

---

## 4.1 Normal Vorticity Actuators

The first idea to use rotating discs for flow control was when Keefe (1997) speculated that drag reductions of up to 40% could be achieved using only spanwise and streamwise control velocities near the wall. Rather than achieving this by oscillating the wall itself, he proposed a new actuation method: an array of rotating discs embedded in the wall would generate normal vorticity across the wall span. Theoretically, such an array could produce almost arbitrary distribution of spanwise and streamwise velocities in the near-wall regions - all while keeping an almost hydraulically smooth wall.

Keefe argued that any practical control scheme would be able to calculate the desired velocities as a function of surface position: from there, the normal vorticity  $\eta$  can be easily derived from the data.

Using results of a fully-developed turbulent channel flow from Kim et al. (1987), Keefe arrived at sizing the motor rotation rate as 1500 revolutions per second and a disc diameter of 80-90 [ $\mu\text{m}$ ]. The motors' useful range would reach around 6 wall units into the flow.

Unfortunately, he never tested such a system neither in experimental nor numerical studies, leaving his claims to be undemonstrated. This is, until Ricco and Hahn (2013) picked up the idea some 15 years later, using a more modern approach to the rotating disc problem.

## 4.2 Rotating Discs for Friction Drag Reduction

Ricco and Hahn (2013) (herein after RH13) performed a parametric study on the normal vorticity actuator devised by Keefe (1997).

In this study, the discs are located next to each other having a diameter  $D$  and rotating with a constant angular velocity  $\Omega$ . From this, the tip velocity  $W = \Omega D/2$  can be defined. The quantities are then normalized with inner units as follows.

$$D^+ = \frac{Du_\tau}{\nu} \quad (4.1)$$

$$W^+ = \frac{W}{u_\tau} \quad (4.2)$$

Discs located next to each other in the streamwise direction have opposite rotation directions, while ones next to each other in the spanwise direction have the same. This is visualized in the schematic 4.1, taken directly from RH13. This configuration was chosen to mimic the standing wave forcing by Viotti et al. (2009), albeit with the difference that the wall forcing covers the entire wall surface with sinusoidal and uniform oscillations along  $z$ .

Furthermore, RH13 simulated the spacing between the discs with a linear velocity change, shown in the right hand side of the figure above. This was done not only to represent the inevitable experimental gap between the discs, but also to avoid the Gibbs phenomenon by using a sufficient number of Fourier modes (Gottlieb and Shu, 1997).

The parametric study was ran at a friction Reynolds number  $Re_\tau$  of 180, based on the stationary wall and the channel half height. Their results are graphically presented in Figure 4.2.

In the above, the shaded area to the left of the hatched line represents the region of drag increase. This means that the optimal diameter in terms of viscous units cannot decrease below a certain threshold, and this threshold increases with increasing RPM. The x-axis shows the disc-diameter made non-dimensional by inner scales, while the y-axis shows the tip velocity scaled in the same way. The circles increase in size with increasing drag reduction, the value of which is expressed

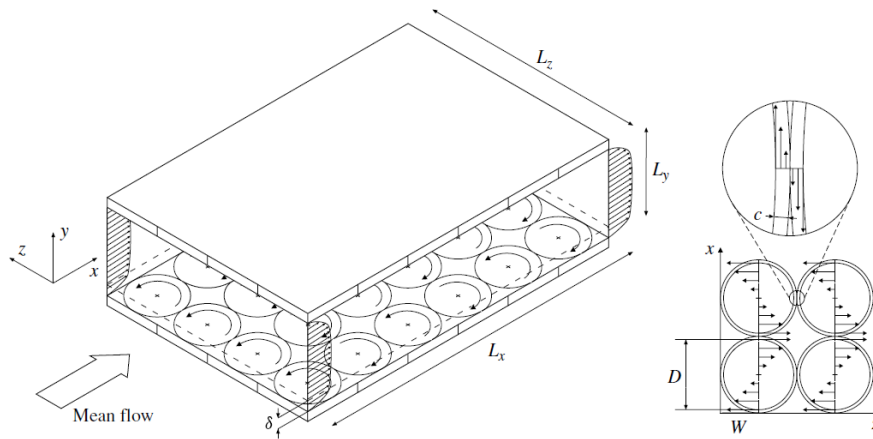


FIGURE 4.1: Schematic of the turbulent channel flow with disc arrangement used in the parametric study by RH13.

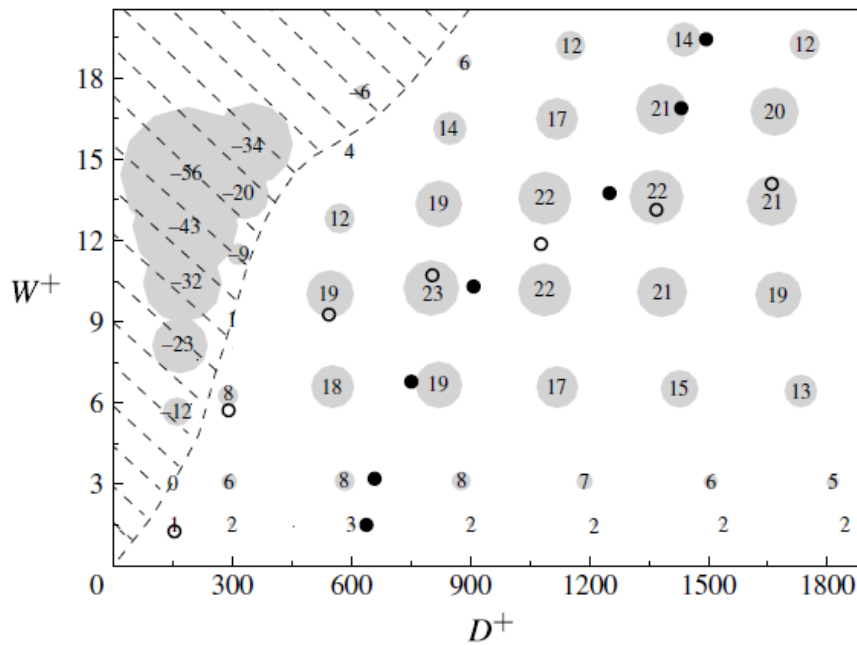


FIGURE 4.2: Map of drag reduction as a function of  $D^+$  and  $W^+$ . The numbers within the circles represent the reduction percentage.

within themselves. A maximum of this drag reduction was found to be 22.9%, computed from  $D^+ = 801$  and  $W^+ = 10.2$ .

Furthermore, the optimal disc diameter for fixed tip velocity is marked by black dots, while the optimal tip velocity (and therefore RPM) for fixed disc diameter is noted by the white circles. Interestingly all these parameters increase with  $W^+$ , and that the black dots (fixed  $W^+$ ) are the zero-drag-reduction profile just shifted to the right by approximately 600 wall units. This implies that there exist lines of optimal combinations for  $D^+$  and  $W^+$ , and that new combinations of these can be found by shifting said lines along the  $x$ -axis.

In a comparative parametric study applied to wall oscillations, Willis et al. (2010) had reported values of maximum drag reduction for amplitude forcing motions between 400 and 800 wall units, increasing when the oscillation length scale matched the spanwise spacing between the streaks;

this is also seen by RH13, with the highest drag reductions happening upwards of  $500 D^+$  and values below that (closer to the streak spanwise spacing) resulting in drag increases. These results are likely to be related to the need for the low-speed, near-wall streaks to be inhibited for a drag reduction to take place.

### 4.2.1 Flow Structures and Drag Reduction Mechanisms

Three dimensional isosurfaces found using Pythagorean sums of streamwise and spanwise velocities visualize the disc flow as near-wall circular patterns about 10 wall units thick. These well defined, streamwise structures appear over sections of the stationary wall where the shear is largest, caused by discs having opposite wall velocities next to each other. These structures are shown in Figure 4.3, showing how they appear as circles centered around  $y^+ \approx 40$

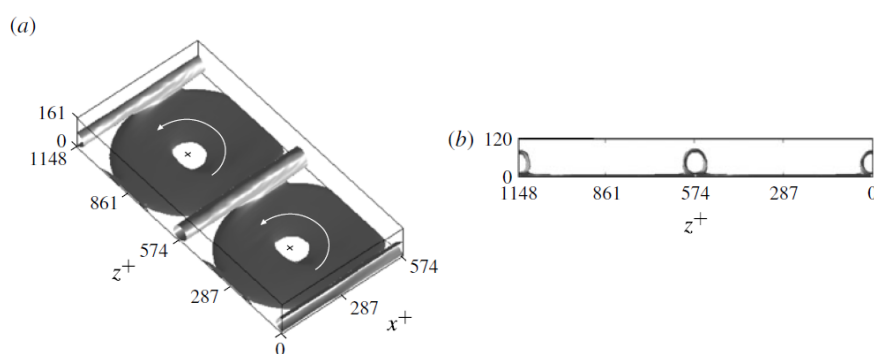


FIGURE 4.3: Isosurfaces of  $\sqrt{u_d^{+2} + w_d^{+2}} = 2.3$ , isometric view with the discs in dark grey (a) and seen from the  $y - z$  plane (b). Adapted from RH13. The rotating discs are in darker grey.

Using an adapted version of Fukagata-Iwamoto-Kasagi identity (Fukagata et al., 2002), RH13 proved that the drag reduction is due mainly to the reduction in disc-flow stresses  $\langle u_d v_d \rangle$  and to the modification of the turbulent stresses, with a major contribution to this reduction coming from the stretched tubular structures between discs.

One of the major takeaways from this study is shown in Figure 4.4 below. Showing instantaneous isosurfaces visualizing low speed streaks, it is immediately clear that the intensity of these is much reduced when passing over the rotating discs - while remaining the same over the stationary wall.

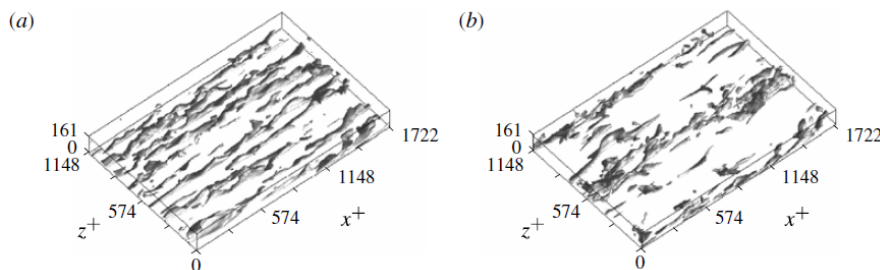


FIGURE 4.4: Isosurfaces for stationary wall case (a) and rotating disc flow case (b)

It has been explored how the low-speed, near-wall streaks are a key player in the production of turbulence, and how several methods that suppress or alter them are successful in decreasing skin

friction. This is likely to be the case also for the rotating discs, where the suppression of the streaks is a key parameter in drag reduction.

Unfortunately, RH13 did not account for  $Re_\tau$  influences in their design, and therefore scalability to engineering applications is still unclear. Furthermore, no experimental data was collected, leaving a substantial hole in the research on the topic.

### 4.3 Disk Spacing

Wise et al. (2014) took over the rotating disc topic and added some more complexity to it, by comparing different disc arrangements versus the baseline case from RH13.

In this previous study the discs were arranged in a square packing scheme (recall Figure 4.1), spinning in opposite directions along the streamwise direction. The coverage for this packing scheme, defined as the percentage of wall surface in motion, was 78%. In Wise et al. (2014)'s study the discs have various different layouts and coverage percentages, shown in Figure 4.5 below. The disc diameters and tip velocities were taken to be the ones with the highest drag reduction from RH13, namely  $D = 3.38, 5.02$  and  $W = 0.13, 0.26, 0.39, 0.52$ . The friction Reynolds number tested was the same, at 180.

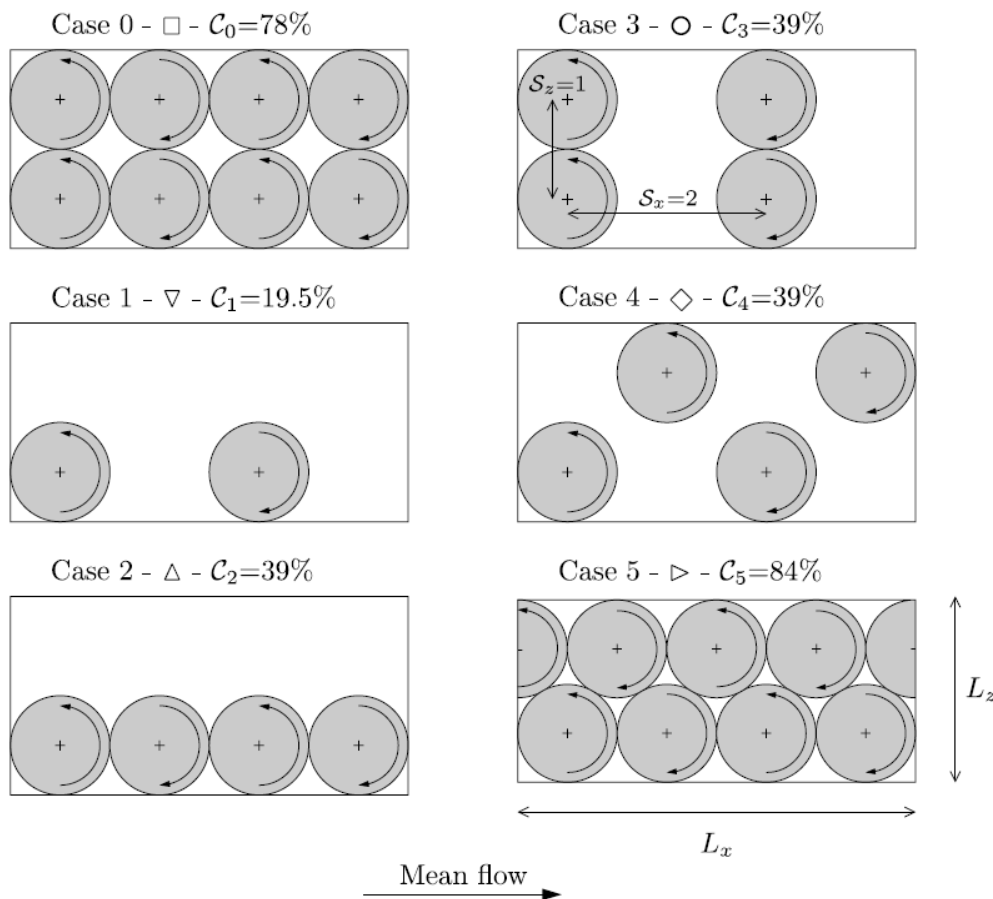


FIGURE 4.5: Disc layouts studied by Wise et al. (2014) in the  $x-z$  plane.

For case  $C_1$ , the surface is covered by a fourth of the number of discs than in RH13. However, the drag reduction is up to a third of the baseline  $C_0$  case. Furthermore, this drag reduction increases monotonically with the disc tip velocity  $W$ . Although cases  $C_2$ ,  $C_3$  and  $C_4$  have the same coverage

area, their drag reduction values differ greatly for the same  $D$  and  $W$ . This shows that the disc arrangement also has an influence on the mechanisms for drag reduction. Specifically regarding case  $C_3$ , two further quantities were defined. By setting the spacings  $S_x = x_d/D_0$  and  $S_z = z_d/D_0$ , a smaller parametric study was performed for optimal disc spacing, the results of which are presented in Figure 4.6. In the previous equation,  $x_d$  and  $z_d$  are the center-to-center spacing between two neighboring discs in the  $x$  and  $z$  directions, respectively.

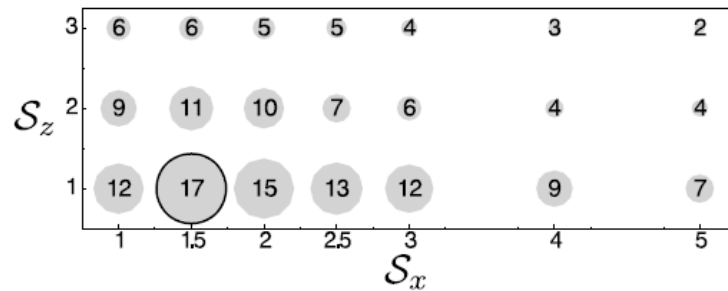


FIGURE 4.6: Map of drag reduction (circled values) for different streamwise and spanwise spacing, for a single value of  $D$  and  $W$ .

As opposed to RH13 where the discs were  $(S_x, S_z) = (1, 1)$  apart, it was found that even higher values of drag reduction can be had by increasing the streamwise spacing to 1.5 times the disc diameter.

Similar to the flow features described in Section 4.2.1, isosurfaces of disc flow show the tubular structures present at the edges of the discs and elongated in the streamwise direction. These structures were especially prominent in cases  $C_3$  and  $C_4$  (shown in Figure 4.7) and not nearly as much in the others, indicating that spanwise interaction between the discs is a prerequisite for their creation.

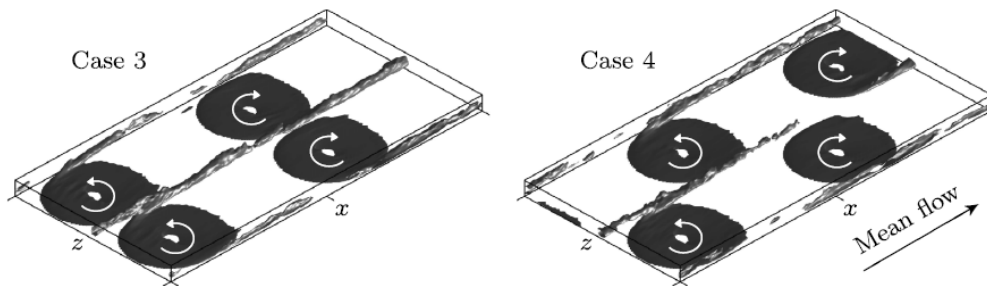


FIGURE 4.7: Isosurfaces for fixed  $D$  and  $W$  for cases  $C_3$  and  $C_4$

Further emphasizing the point made by RH13, the Reynolds stresses associated with these tubular structures were found to contribute favorably to the net drag reduction. The FIK identity was used once again to explain the formation of the inter-disc structures: these are created only in the case of sufficient interaction between spanwise discs (as alluded to in the paragraph above), as well as the disc sides. Furthermore, the disc tip velocity was required to be greater than  $W \geq 0.26$  for the generation of these structures, with a further requirement of a maximum spacing between disc centers approximately  $\sqrt{2}D_0$ . Unfortunately no other mechanisms were postulated for the reasons of drag reduction in this study.

## 4.4 Oscillating Discs

Another study was made by Wise and Ricco (2014) to study the behaviour of the flow with discs subjected to sinusoidal oscillations. With the discs spaced like RH13 (Case  $C_3$  and  $(S_x, S_z) = (1, 1)$  from WR14), the tip velocity was prescribed as

$$\tilde{W} = W \cos\left(\frac{2\pi t}{T}\right) \quad (4.3)$$

The rest of the quantities were left to be the same, with the Reynolds number prescribed as 180 and subsequent streamwise rows of discs rotating in opposite directions.

Using the Fukagata-Iwamoto-Kasagi identity (Fukagata et al., 2002), the authors showed that the wall-friction reduction was caused by two separate effects. One, causing the attenuation of the turbulent Reynolds stresses, is the direct shearing action of the near wall boundary layer on the oscillating disc. This oscillatory boundary layer strongly resembles the oscillating wall Stokes layer at high frequencies, and it is therefore expected to modify the flow over the disc surface in a similar way. This was elaborated in depth by Ricco et al. (2012), who stated that the period shear near the wall acts to increase the turbulent kinetic energy of the flow and attenuate the Reynolds stresses, as well as reducing the intensity of the low-speed streaks.

The second independent effect is once again due to the streamwise elongated structures forming between discs and modulating slowly over time. While the authors first stated their positive contribution to drag reduction, they further published a corrigendum (Wise et al., 2018) going back on their claims. In the corrigendum, the inter-disc structures are directed away from the wall and against the mean flow direction, as shown in Figure 4.8. This, unlike what was mentioned in Ricco and Hahn (2013) and Wise and Ricco (2014), further increases the Reynolds stresses and has a negative effect on drag reduction. Still, further insight is needed into the generation of these structures. Quantitatively, the authors describe the spanwise forcing to have a drag effect

$$\mathcal{R}_t \propto \int_0^1 (1-y) [\widehat{u_t v_t} - \langle \widehat{u_{t,s} v_{t,s}} \rangle] dy \quad (4.4)$$

and the structures between discs

$$\mathcal{R}_d \propto \int_0^1 (1-y) \langle u_d v_d \rangle dy \quad (4.5)$$

where, after the corrigendum, the disc stresses have opposite signs and therefore lead to an increase in turbulence production.

As a finale for the spinning discs series, Olivucci et al. (2019) studied a flush-mounted spinning rings setup, coupled with vertical velocity opposition control and hydrophobic surfaces. The main goals of this numerical study were to further develop and understanding of the physical mechanisms behind the drag reduction, as well as enhancing the latter by two types of distribution control: wall-normal velocity actuation and hydrophobic surfaces.

The arrangement is very similar to the ones discussed previously, with the rings creating triangular waves of spanwise velocity along the streamwise lines passing through their centers. The difference with the other studies, besides the opposition control, resides in the fact the discs are not fully rotating, but they are instead a ring. This means that the center of the disc does not induce any velocity over a diameter  $D_i < D$

This study once again found the rolls present at the disc interaction boundary, characterized by wall normal velocity. These are formed by ejections towards the channel core in the streamwise direction, themselves created by large values of the wall-normal ring flow component  $v_d$ .

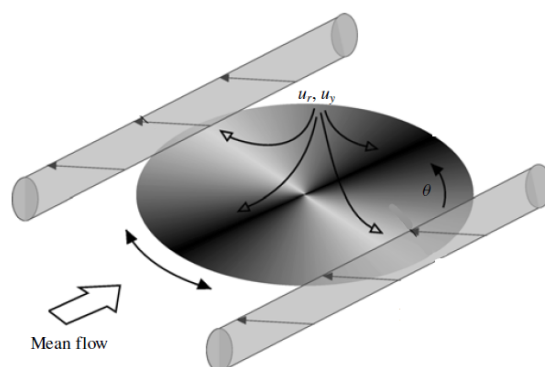


FIGURE 4.8: Schematic showing the two mechanisms determined to be responsible for the drag reduction. Radial flow spanwise forcing (Eq. 5.3) over the disc and structures (Eq. 5.4) between discs. Adapted from Wise et al., 2018

The product  $u_d v_d$  (recall  $u_d$  being the streamwise ring flow component) is negative where these structures exist; over the spinning portion of the rings,  $v_d$  takes negative values because it balances the intense positive ejections at the sides, as well as the weaker positive motion toward the portion of stationary wall above the ring centers. These positive and negative regions of  $v_d$  cancel each other out, with the alternating suction/ejection pattern inducing four coherent streamwise rolls.

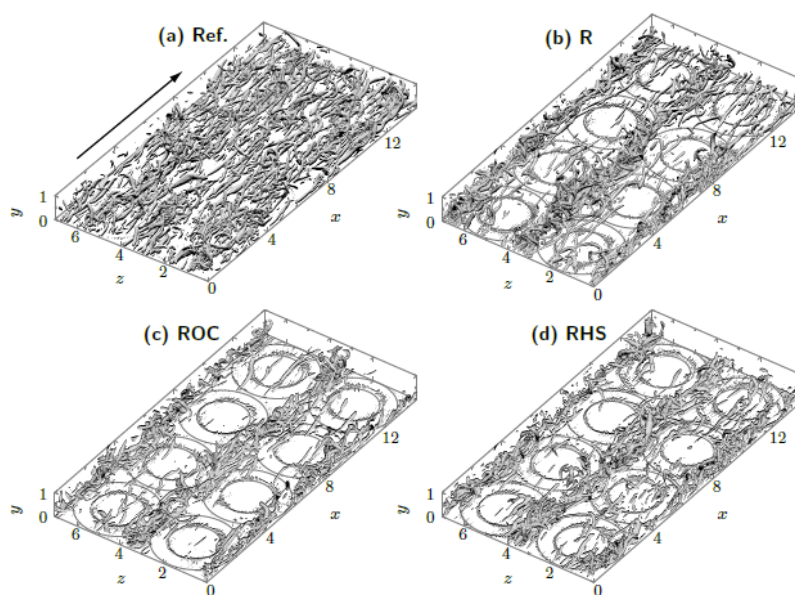


FIGURE 4.9: instantaneous  $\lambda_2$  iso-contours for **a)** reference flow, **b)** rotating rings only, **c)** rotating rings and opposition control and **d)** rotating rings and hydrophobic surface

The highest value of drag reduction (27.7%) was found with the hydrophobic surface only. This is significantly larger than the 20% present with the rotating rings only, but when combining the two a similar result was obtained at 26.5%. Combining the rotating discs and the opposition control also yields close to 30% drag reduction, further highlighted by the lack of coherent structures over that configuration as seen in Figure 4.9.

Overall, it was found that the streamwise aligned rolls on the ring side have a local effect in decreasing the wall shear stress because of their negative near-wall streamwise velocity. However, in

a ring arrangement, they are responsible for additional negative ring-flow Reynolds stresses, which globally contribute to an increase in turbulent drag. Within the central section, the Stokes layer previously seen in RH13, WR14 and other oscillating wall studies is still present. This is responsible for the drag reduction, and its thickness is the same as the optimal one studied by Quadrio and Ricco (2011). The combination of opposition control and hydrophobic surfaces further decrease the skin friction drag by 7.4 and 6.5%, respectively. Importantly, the Stokes layer is not damaged by these control schemes, implying that the drag-reduction effect due to the rings is still present and the increase can be said to be net.

However, the authors acknowledged the difficulties in the practical realization of the rings and associated control systems, specifically for large scale engineering applications such as aircraft or ships. Specifically regarding the opposition control, enormous databases of information would need to be processed every second, rendering this combined method far out of reach of experiments with current processing capabilities.

## 4.5 Summary

The research topic on which this work hinges upon has been thoroughly reviewed along several variations of it. From this review, specifically the articles from Ricco and Hahn (2013) and Wise et al. (2014), several non-dimensional parameters have been identified as driving the performance of the rotating discs. The optimal non-dimensional disc diameter  $D^+$  and tip velocity  $W^+$  have been found to be 800 and 10.2, respectively. The spacing between the discs has been further defined to be  $D_0$  in the spanwise and  $1.5D_0$  in the streamwise direction. Putting this all together, a turbulent drag reduction of around 30% was found at a Reynolds number  $Re_\tau = 180$ . By scaling these parameters with the appropriate units, it is possible to reproduce the same non-dimensional parameters in an experimental setup at much higher Reynolds numbers than previously tested. As the following chapters will describe, this setup will be limited to the rotating discs without opposition control, oscillating rings or any more complicated mechanical features. The aim will be to investigate the flow physics in the rotating discs case versus a baseline case.

## Chapter 5

# Experiment Design and Methodology

To achieve the aims described in previous chapters, an experimental campaign was conducted in TUDelft's windtunnel laboratories. In the foregoing chapter the specifications of the setup used to answer the research question is provided, ranging from the windtunnel, presented in Section 5.1, to the test setup presented in Section 5.2. The setup is investigated more in detail in Section 5.3, with the design procedure detailed in 5.3.1.

### Contents

---

<b>5.1</b>	<b>Wind Tunnel</b>	<b>39</b>
<b>5.2</b>	<b>Setup and Coordinate System</b>	<b>39</b>
<b>5.3</b>	<b>Test Section</b>	<b>40</b>
5.3.1	Design Methodology	41
5.3.2	Assembly Considerations	42
<b>5.4</b>	<b>Measurement Equipment Setup</b>	<b>42</b>

---

## 5.1 Wind Tunnel

The experimental campaign took place at the W-Tunnel in TUDelft's high speed laboratory within the Aerospace Engineering faculty. The W-Tunnel is an open jet open return facility with an exit cross sectional area of 0.6[m] × 0.6[m]. The flow velocity is regulated by setting the RPM of a centrifugal fan, and is displayed live on a control PC which calculates it using pitot tube within the nozzle. The control PC, running LabVIEW's software, is also able to use sensors placed within the W-tunnel to give live readings of barometric pressure, temperature and density. Recording these measurements allows the computation of the dynamic and kinematic viscosity of the flow for every individual test using Sutherland's law, recalled below:

$$\mu = \mu_0 \left( \frac{T}{T_0} \right)^{3/2} \frac{T_0 + S}{T + S} \quad (5.1)$$

Where  $T_0$  and  $\mu_0$  are reference temperature and dynamic pressure, respectively, and  $S$  is Sutherland's constant. The kinematic viscosity is then simply  $\nu = \mu/\rho$ .

The maximum velocity of the tunnel is 25 [m/s], more than sufficient for the current investigation. Furthermore, the seeder used for the Particle Image Velocimetry measurements is located upstream of the contraction.

In order to accommodate for the plate over which the turbulent boundary layer would develop and the plate containing the discs itself, the test section was elongated using a 0.4[m] long wooden section (1), a 1[m] long plexiglass section (2) and a 0.6[m] long plexiglass section open at the bottom (3). The latter allowed for the blockage produced by the motors to have a minimal effect on the turbulent boundary layer formation upstream. The various sections are highlighted in Figure 5.1.

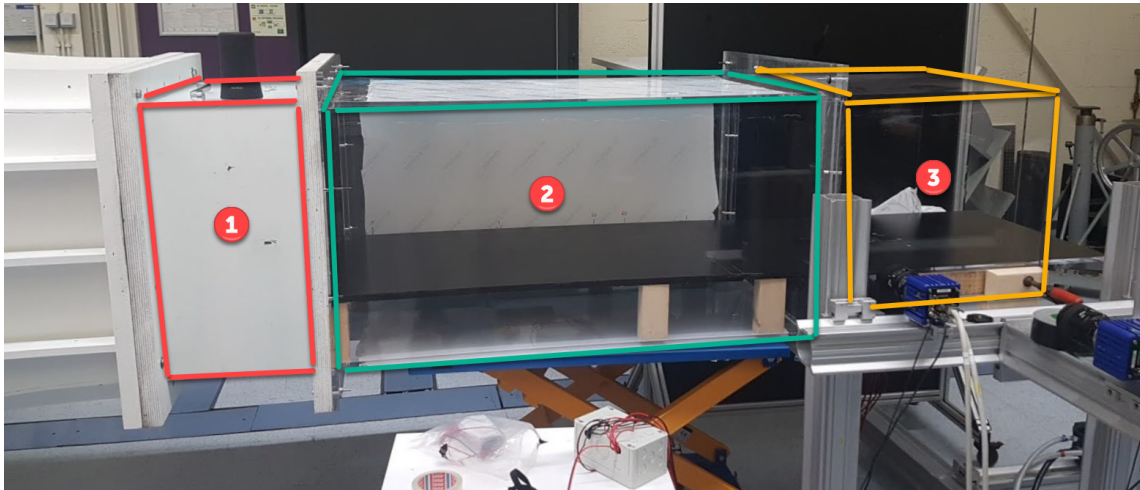


FIGURE 5.1: Full windtunnel test sections as described. Wooden extension (1), plexiglass (2) and open bottom test section (3)

## 5.2 Setup and Coordinate System

The full setup is as depicted in Figure 5.2. Note how the setup coordinate system is located at the trip, while a second coordinate system is placed at the first disc's leading edge. Both these coordinate systems are Cartesian right-handed and placed at the wall. The setup coordinate system

$(x_s, y_s, z_s)$  was used to define the setup dimensions, while the disc-coordinate system  $(x_d, y_d, z_d)$  will be used for the result description.

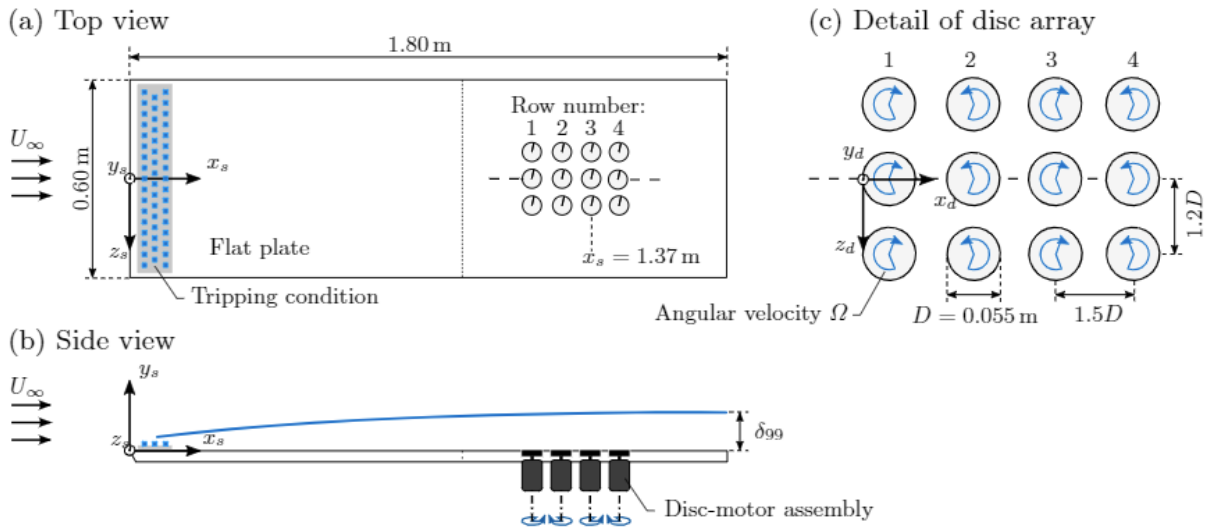


FIGURE 5.2: (a, b) 2D schematic of full experimental setup. (c) Detailed view of disc array, with non-equidistant spacing in the streamwise and spanwise directions. The angular velocity direction is shown by the blue arrow.

The following sections describe the various components of the setup more in-depth.

### 5.3 Test Section

To answer the present work's research questions, it is necessary to take measurements of a fully turbulent boundary layer. The largest scales of the flow are fixed by the scale of the facility used and the viscous scales become too small at high Reynolds numbers (Marusic et al., 2010); it is then important for the to maintain sufficiently small measurement volumes to avoid spatially averaging the smaller scales. Generally, better measurements can be obtained in a thicker boundary layer due to the thickening of the logarithmic layer. While this could be achieved naturally by extending the test section and allowing the TBL to develop naturally, space constraints within the W-Tunnel call for a boundary layer trip to artificially transition the flow upstream of the test section. The boundary layer was therefore heavily tripped approximately 1.4 [m] upstream of the measurement location by means of distributed roughness elements, also known as LEGO bricks, of 15 [mm] height (Figure 5.3).

Within the test section, the setup was composed of two different plates, taped over a split line to ensure a flush finish: the first, holding the trip, was placed at the beginning of the contraction and extended 1.25[m] downstream. The second, housing the disc array, was positioned downstream of the first plate and it extended 1[m] further downstream. Comparing these dimensions to the ones from Figure 5.1 leaves approximately 0.25[m] of plate hanging outside the enclosed test section, ending a few centimeters behind the last disc of the array. This was not considered to be a problem, as the expansion at the very edges of the plate was deemed to be acceptable and no measurements would be taken there.

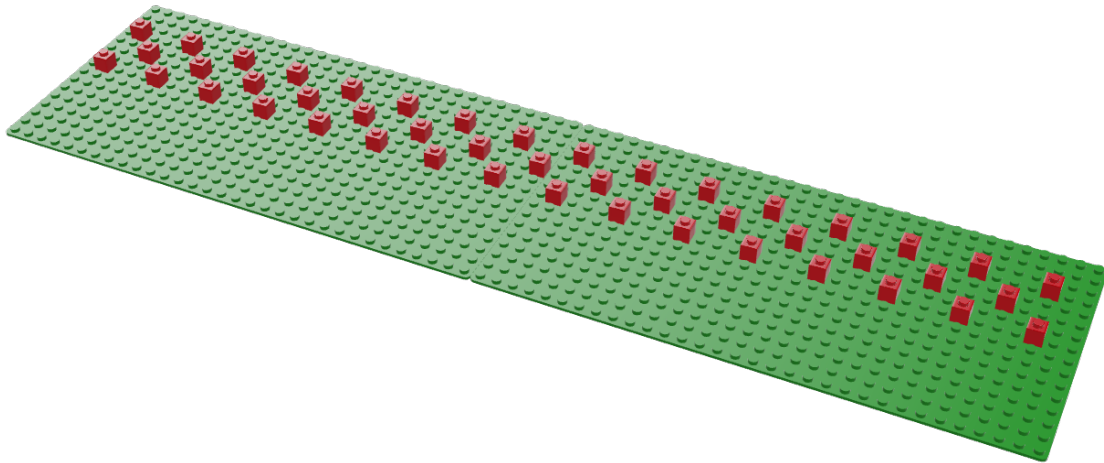


FIGURE 5.3: Render of LEGO trip

The entire setup was positioned 0.15 [m] above the text section's floor using wooden supports, to allow for the cables to slide underneath. Finally, the plates' inclination was measured independently at various locations using a digital clinometer, resulting in a rather consistent  $0.0^\circ \pm 0.2^\circ$  of inclination in both the spanwise and streamwise direction.

The leading edge of the first plate was manufactured to have a  $30^\circ$  angle, in order to avoid any large separation. In the downstream plate, a  $3 \times 4$  array of counter-rotating discs was installed flush with the plate. The rotation itself was obtained by mounting a EsportsMJJ 775 DC Motor rated for 12 [V] to the machined discs. This specific motor was chosen due to its dual ball-bearings placed at the ends of the shaft, guaranteeing minimum vibrations in the shaft even at high rotational speeds. The motors were connected in parallel to a 5 [A] power supply; the dial on the power supply was used to finetune the voltage supplied to the motors, in turn providing the RPM desired. Rotations per minute up to the tens of thousands can be achieved with this setup, but the RPM was limited to 3400 during the experiment.

After describing the main components of the setup, the following subsections presents the design methodology and a side note about the manufacturing and assembly considerations encountered during the experiment preparation.

### 5.3.1 Design Methodology

The inputs driving the process were partially provided by literature from Ricco and Hahn (2013) and Wise et al. (2014). Their research defined the parameter space for rotating discs mainly by diameter and tip velocity, and partially by the stream- and spanwise disc spacing. Non-dimensional optimal parameters were provided by Ricco and Hahn (2013) for the diameter and the tip velocity, while Wise et al. (2014) offered diameter-normalized information about the disc spacing. Turbulent boundary layer characteristics offered by Kempaiah et al. (2020) proved useful in scaling the discs to physical units, provided that the windtunnel and the boundary layer trip used were consistent with the previous experiment. Using a friction velocity from Kempaiah et al. (2020)'s  $Re_\theta = 1787$  experiment the optimal values of Ricco and Hahn (2013) were scaled to physical units, corresponding to a disc diameter ( $D_0$ ) of 0.055 [m], a streamwise spacing of 0.083 [m] ( $1.5D_0$ ) and a spanwise spacing of 0.065 [m] ( $1.2D_0$ ) between disc centers. The spanwise spacing was increased from the one proposed in the literature to allow for the physical constraints of clearance between discs. The tip velocity was also scaled to physical units and converted to rotations per minute, allowing for

a direct measurement during experimental conditions described in Section 5.3.2. However, as the wind-tunnel flow velocity changes so do the boundary layer characteristics, and with them the friction velocity. While the RPM of the motors can be changed to compensate for this, the disc diameter cannot; for this reason the non-dimensional diameter is not at the optimum found in literature for all velocity campaigns. Further discussion of this consideration and its effects will be forthcoming in Section 6.2.3. The dimensions of the array were chosen in order to have spanwise symmetry across the center disc, and with enough discs in the streamwise direction so that the flow evolution over the array could be quantified. Furthermore, the number of discs was limited by the manual labour required to mount, align and wire all the discs.

Full technical drawings presenting the mounting arrangements between disc and motors can be found in Appendix A.

### 5.3.2 Assembly Considerations

While the design of the setup is discussed in Section 5.3.1, the assembly considerations presented here are ones that arose only at the time of preparation. To guarantee a uniform RPM throughout the entire array, it is necessary to mount the motors so that a constant gap remains to all of their sides - that is, the motor shaft cannot be placed off center. To achieve this, the mounting holes in the plate were drilled slightly larger than required allowing for some wiggle room during assembly; moreover, the discs were mounted while spinning so that any vibrations could be felt and the position could be adjusted.

As a result, a quantification of disc RPM variance performed with the plate mounted in the wind-tunnel resulted in the following map (Fig. 5.4). The RPM of the discs had a mean deviation ranging from 2.2% at lower RPM (around 700) to less than 1.5% at higher RPM (upwards of 3000). A voltage-mean RPM curve was then created for the data points needed to run the experiments, so that the RPM could be set via the power supply without need for further measurements.

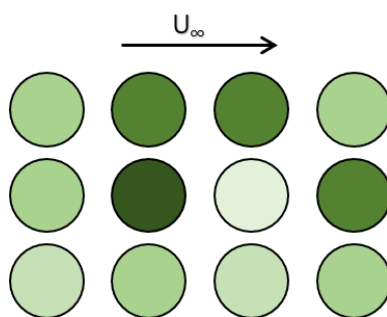


FIGURE 5.4: RPM Map for disc array, pattern of various voltages measured. Darker is faster, but the scale is not absolute (fastest to lowest spinning discs only have  $\sim 5\%$  deviation)

Finally, to reduce the reflections of the laser on the disc array plate the latter was covered in matte black adhesive foil. This significantly decreased the reflections to be reduced in pre-processing, and is augmented by using matte black spray paint for certain datasets where the ground itself does not need to be imaged at high resolution.

## 5.4 Measurement Equipment Setup

Although a more in-depth overview on the PIV system will be provided in Section 6.1, a brief introduction on how the PIV system was setup will be provided as a conclusion to this chapter. For

the characterization of the turbulent boundary layer two cameras were employed to image the flow over several discs in the array. These cameras were mounted on Linos X95 beam systems, allowing them to slide in the wall normal and streamwise direction while maintaining their  $x$  or  $y$  location, respectively. Several structures were built throughout the testing campaign, but all of them were connected directly to the laser pulse generator to make certain that the laser sheet used would be perpendicular to the camera sensor in all the planar PIV measurements. The beams furthermore guaranteed a high level of stiffness against vibration and bumps, keeping the field of views always at the desired locations.

## Chapter 6

# Measurement Techniques

Following a description of the setup, this chapter describes in detail the tools and methodology used throughout the testing campaign. It covers the motivations for each choice, the measurement equipment setup and hardware as well as the acquisition and processing procedures. An introduction to Particle Image Velocimetry and its practical considerations are given in Section 6.1. Following, Section 6.2 reviews all the parameters related to data acquisition, including the test matrix that was followed throughout the campaign. This leads directly into Section 6.3, discussing the data processing and reduction procedures followed. Finally the chapter is concluded by an analysis of the statistical significance of the results, presented in Section 6.4.

### Contents

---

<b>6.1 Particle Image Velocimetry</b>	<b>45</b>
6.1.1 Seeding	45
6.1.2 Illumination	46
6.1.3 Imaging	46
<b>6.2 Data Acquisition</b>	<b>48</b>
6.2.1 Calibration	49
6.2.2 Locations of Measurement Planes	49
6.2.3 Non-dimensional Test Matrix	50
<b>6.3 Data Processing and Reduction</b>	<b>52</b>
6.3.1 Cropping	53
6.3.2 Data Reduction	54
6.3.3 Reconstruction of full boundary layer profile	56
<b>6.4 Uncertainty Analysis</b>	<b>57</b>
6.4.1 Statistical Uncertainty	57
6.4.2 Interrogation Window Size Uncertainty	57
6.4.3 Cross-Correlation Uncertainty	57
6.4.4 Particle Tracing Uncertainty	58
6.4.5 Uncertainty in numbers	58

---

## 6.1 Particle Image Velocimetry

The experiment makes use of 2D2C PIV, two-dimensional two-component planar Particle Image Velocimetry. This technique employs double-frame single-exposure imaging, meaning that a single illuminated image is captured for each illumination pulse.

Particle Image Velocimetry (PIV) is a non-intrusive flow measurement technique based on capturing the position of seeder particles in the flow at very short time intervals, and reconstructing the velocity vectors of a set of these particles via a cross-correlation analysis. Seeder particles, discussed more in depth in Section 6.1.1 below, are added to the flow and are illuminated by a thin laser sheet (discussed also further down in Section 6.1.2) at a very small time interval  $\Delta t$ . During the illumination period, a digital camera with a CMOS sensor captures the images in two subsequent frames. Following the capture of a set amount of images and their storage into the control PC memory, the images are divided into smaller interrogation windows and a cross correlation is performed between subsequent frames for each interrogation window. The correlation results in a physical displacement vector, which is then divided by the time interval to obtain the velocity of the particles within that interrogation window. Stitching together all the windows results in the overall imaged flowfield.

### 6.1.1 Seeding

When conducting PIV measurements the ideal case is to have as many particles as possible in a homogeneous distribution along the measurement plane, such that each particle can be distinguished individually but no flow structures can be observed like in Figure 6.1. Inhomogeneous, insufficient and excessive particle densities can all result in failures to identify distinct particles and therefore critical flow features. While the seeding distribution characteristics can be determined empirically, the seeding particle themselves have to have specific mechanical and light scattering properties, discussed below.

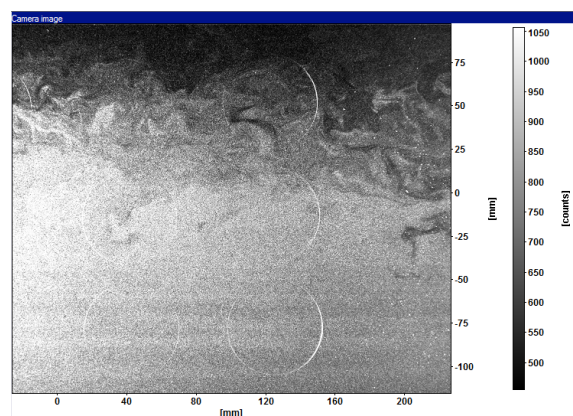


FIGURE 6.1: Excess seeding

For a seeding particle to be used as proper tracer in PIV applications there are a few requirements that it has to satisfy. Firstly, it must follow the flow in a realistic fashion and with minimal lag. Secondly, it must scatter enough light when illuminated so that it is visible in the recordings. Other requirements consist of safety and contamination considerations, but the first two are the main ones discussed in this section.

To begin discussing the first requirement, one has to realize that following the flow with minimal lag also comes with the implied requirement that the effect of particles on the flow must also be kept to a minimum. The particles generally used for PIV are assumed to be spherical and with a low Reynolds number, so that their forces are dominated by Stokes drag. This allows the researcher to define a certain slip velocity of a particle with respect to the accelerating surrounding flow, for example with Equation 6.1 from Raffel et al. (2018)

$$V_{\text{slip}} = V_p - U = -\frac{d_p^2}{18} \frac{(\rho_p - \rho_f)}{\mu} \frac{dU}{dt} \quad (6.1)$$

where  $p$  and  $f$  subscripts refer to the particle and fluid properties, respectively. The solution of the above equation is an exponential decay of the velocity for a change in flow speed, meaning that the

particle will always have a time response to the flow. This time response is the particle lag which, assuming a particle density much greater than flow density ( $\rho_p \gg \rho_f$ ), is proportional to the particle size.

Reducing particle size indiscriminately however runs into problems with the requirement for light scattering. In order to acquire good quality data, the particle's intensity on the recorded image must exceed that of the background by several orders of magnitude. The light scattering behaviour of a particle depends, among others, on the particle diameter and the laser light wavelength; therefore the particle size is yet again a critical factor for the selection of the seeder and a trade-off must be made between the tracing fidelity and light scattering.

The seeding particles used for this experimental campaign take the form of spherical fog particles with the diameter of around 1 [ $\mu\text{m}$ ], generated by a SAFEX Fog Generator<sup>1</sup>. The fog generator is placed upstream of the test section, and the flow is seeded by running the generator with the wind on for a certain amount of time. The windtunnel action scatters the particles around the tunnel room, until a sufficient density is achieved and particles can start recirculating in the flow. Given their naturally buoyant properties, minimal residue is expected while the windtunnel is running, allowing the tests to be as long as necessary. Consistent top-up of generated particles in the room was performed once every two datasets were collected, with visual inspection being performed every dataset.

Despite the small diameter of the selected particles, the laser used is deemed to have enough energy per pulse to sufficiently illuminate the particles. It is then necessary to determine how to setup the illumination equipment.

### 6.1.2 Illumination

The illumination of the seeding particles is obtained with a double pulse Nd:YAG EverGreen Quanta laser. This laser produces light at a wavelength of 532 [nm] and a frequency of 15 [Hz] shaped in a circular light beam, which is then expanded and shaped into a sheet using several mirrors and spherical lenses. The exact setup of these depended on the dataset of interest, but generally the resulting laser sheet thickness was found to be around 2 [mm] at the measurement location.

Two main illumination setups were employed throughout the testing campaign, with a brief description of each following below.

**Wall Normal, Flow Parallel (X-Y) Sheet** The laser sheet for the X-Y measurements was introduced into the windtunnel from downstream of the test section. The laser was placed on the ground below the test section and pointed in the direction of the flow; two mirrors rotated the beam 180 degrees around while enlarging it into a sheet, "cutting" across the domain in the X-Y plane.

**Wall Parallel, Flow Parallel (Z-X) Sheet** Similarly to the above, the laser was shined through the test section from the opening downstream of it. The same mirror and lenses setup was used, but this time a lens was tilted 90° to generate a wall-parallel sheet. The height of the sheet was regulated using a Linos beam connection to move the mirror/lenses assembly and was set at approximately 4 [mm] above the wall, a location corresponding to approximately  $70y^+$  for a 3 [m/s] flow velocity.

### 6.1.3 Imaging

Before discussing about imaging and the practicalities of it during the experimental campaign, it is necessary to introduce some fundamental parameters and governing equations.

<sup>1</sup>[https://www.flowmarker.com/fileadmin/user\\_upload/pdf/SDB\\_NEBELFLUID\\_EN\\_alle\\_Sorten\\_V1\\_01\\_-\\_03\\_11\\_2011.pdf](https://www.flowmarker.com/fileadmin/user_upload/pdf/SDB_NEBELFLUID_EN_alle_Sorten_V1_01_-_03_11_2011.pdf)

The geometrical features of any thin lens are governed by the thin lens equation, as follows:

$$\frac{1}{f} = \frac{1}{d_o} + \frac{1}{d_i} \quad (6.2)$$

where  $d_o$  is the distance between lens and object to be imaged and  $d_i$  is the distance between the lens and the sensor recording the image. The magnification factor represents the ratio between image and object distance, equivalent to the ratio between field of view and sensor size.

$$M = \frac{d_i}{d_o} = \frac{N_{pix}l_{pix}}{l_{fov}} \quad (6.3)$$

Given the desired field of view to be imaged, the thin lens equation can then be used to determine the location of the camera with respect to the test section. Of course, practical hardware limitations impose further restrictions on this and therefore the equation will not be followed precisely. Furthermore, the focus characteristics of the lens can be used to further improve the imaging. These are governed by the f-stop, the ratio between the focal length and the lens' diaphragm's aperture ( $d_{lens}$ ):

$$f_{\#} = \frac{f}{d_{lens}} \quad (6.4)$$

The higher the f-stop, the larger the depth of field and the more particles will be in focus to be imaged properly. The focal depth  $\delta z$  is expressed as follows

$$\delta z = 4.88\lambda f_{\#}^2 \left( \frac{M+1}{M} \right)^2 \quad (6.5)$$

where  $\lambda$  is the laser wavelength.

For the purpose of a PIV experiment the depth of field has to be at least equal to the laser sheet thickness, so that all the particles within it will be imaged correctly. A further requirement concerns the particle diameter, limiting it to

$$d_{diff} = 2.44\lambda(1+M)f_{\#} \quad (6.6)$$

due to diffraction effects coming into play for small diaphragm apertures.

Going back to the magnification factor, the imaged particle geometrical diameter is given by

$$d_{geom} = Md_p \quad (6.7)$$

With these two diameter requirements placed by the imaging system, the particle image diameter can be approximated by a Pythagorean sum of the two:

$$d_{\tau} = \sqrt{d_{diff}^2 + d_{geom}^2} = \sqrt{(Md_p)^2 + d_{diff}^2} \quad (6.8)$$

To avoid peak-locking problems, when the particle appears as a single pixel on the image and has no displacement between image pairs, the value of  $d_{\tau}$  can be set to be greater than 2-3 pixels, resulting in an f-stop to be used of  $f_{\#} = 8$ .

The last parameter to be optimized is the time between laser pulses, in return determining the time between each image in the pair and the displacement of any given particle on the sensor. Empirically, the "quarter rule" states that the time interval  $dt$  should be chosen such that the particle displacement does not exceed one fourth of the interrogation window size. By experience, it is known that the particle's average displacement should be around 12 pixels on the sensor for optimal

quality data, and therefore the following equation is composed

$$dt = \frac{s_{pix} l_{pix} M}{u_{\infty}} \quad (6.9)$$

where  $s_{pix}$  is the particle displacement between images in the pair and is set to 12. The  $dt$  value itself changes greatly between dataset to be collected, due to external flow velocity and other considerations. The values used are presented in Table 6.1 below.

$U_{\infty}$ [m/s]	$dt$ [ $\mu$ s]	
	Wall Normal	Wall Parallel
3	200	300
5	150	200

TABLE 6.1:  $dt$  used for each dataset-type collected

The wall-parallel datasets are expected to be imaged within the logarithmic layer, and therefore the mean flow velocity is expected to be lower than when sampling the full boundary layer.

The flow was sampled at the maximum frequency allowed by the laser, 15 [Hz]. This means that with this laser it is not possible to have full time resolution of the flow.

Finally, Table 6.2 presents an overview of the technical specifications for the various imaging equipment used.

<i>LaVision Imager sCMOS</i>		
Property	Symbol	Value
Resolution	$r$	2560x2160 [px]
Pixel size	$l_{pix}$	6.5x6.5 [ $\mu$ m]
Frame rate	$f_{im}$	50 [Hz]
Exposure time	$t_{im}$	15 [mics] - 100 [ms]
Digital output	-	16 [bit]
<i>Lenses</i>		
Property	Symbol	Value (f105 / f60)
Focal length	$f$	105 [mm] / 60 [mm]
Aperture range	$f_{\#,min} - f_{\#,max}$	2.4-32 / 2.8-32

TABLE 6.2: Specifications of Imaging Equipment

## 6.2 Data Acquisition

This section will discuss the practical data acquisition procedures, ranging from the calibration of the PIV system to the plane location for the different dataset types. Recall that the aim of this experiment is to quantify the change in skin-friction drag and investigate the flow mechanisms that drive this change. The first part will be done in two main ways

- Direct wall measurements, quantifying the slope of the velocity profile at the wall  $(\partial u / \partial y)_{y=0}$  and allowing a direct description of the wall shear stress and therefore the skin-friction coefficient.

- Determining the friction velocity from Spalding's law of the wall and the Clauser chart, using the logarithmic region  $u^+ = \frac{1}{\kappa} \log y^+ + B$  with constants  $\kappa = 0.387$  and  $B = 4.1$  (Marusic et al., 2010).

All the data acquisition is therefore performed keeping the objectives in mind, at freestream velocities of 3 and 5 [m/s].

### 6.2.1 Calibration

Calibration of the captured images serves various important purposes. Firstly, the camera images might be slightly warped in one or more directions; while this is less of a problem in planar than in stereoscopic PIV, it is a geometrical effect still present and as such it must be corrected for. Secondly, in order for the processing software to have the correct physical displacement of the particles when performing a cross-correlation, the pixel-to-mm conversion must be given for the relevant images. To achieve both these goals simultaneously, a calibration procedure can be followed by identifying a set of points along physically orthogonal directions.

Bespoke calibration plates were created for both the wall normal and wall parallel planar measurements. These were placed on the measurement location by turning the laser to low power "alignment" mode and letting it graze the plate.

For planar PIV calibration, a sheet of paper with 10 [mm] squares drawn on was glued to a support and inserted in the tunnel. The support was roughly A3 sized, and this allowed for both full TBL and near-wall measurements to be calibrated using the same plate. For wall-parallel measurements, slits were cut along the two edges of the paper coinciding with the outer disc diameters, allowing the sheet to be aligned with the discs in two directions and therefore guaranteeing the correct directionality with respect to the flow.

### 6.2.2 Locations of Measurement Planes

In total, five different imaging planes and fields of view (FOVs) were used. These ranged through a variety of scopes, from imaging the full boundary layer for characterization to the near-wall, high-resolution imaging. In all configurations the CMOS cameras were located outside of the tunnel, with the sensor axis perpendicular to the FOV-planes.

Figure 6.2a below shows the setup for the TBL characterization. This involves one camera equipped with a Nikkor 105mm lens focused on the first disc (*FOV-S*) and a second camera with a Nikkor 60mm imaging the flowfield over the first three discs in the streamwise direction and extending over the full boundary layer in the wall-normal direction (*FOV-L*). *FOV-S* allows for high resolution of the near wall regions, especially the viscous sublayer. This, as will be discussed later, will be key in determining the friction velocity. *FOV-L*, on the other hand, allows for the characterization of the full logarithmic layer as well as the outer regions and wake of the boundary layer. Section 6.3.2 will discuss how the different profiles are merged together to reach a full characterization of the TBL.

Getting to the highest level of detail presented in this work, Figure 6.2b presents a schematic of the over-disk detail setup. Despite being represented by three fields of view, this setup still consisted of two cameras being moved around to image the flowfield above the third and fourth disc (*FOV-3* and *FOV-4* respectively), as well as the region immediately after the array (*FOV-A*). Firstly a series of datasets was collected over discs 3 and 4. Once this process was completed both cameras were moved horizontally by  $1.5D_0$  allowing for the imaging of the flowfield in *FOV-4* and *FOV-A*. All of these FOVs were captured with Nikkor 105mm lenses and have physical dimensions of 17.5x18[mm]. The last configuration to be discussed is the X-Z wall-parallel plane. Here two cameras are positioned above the plexiglass test section and equipped with Nikkor 60mm lenses.

Their fields of view span the entire array and have a 30[mm] overlap in the center, allowing for the reconstruction of the flowfield over all the discs. Each field of view spans 250x210 [mm], having approximately 10[mm] of clearance to the sides of the array. The schematic of this is presented in Figure 6.2c.

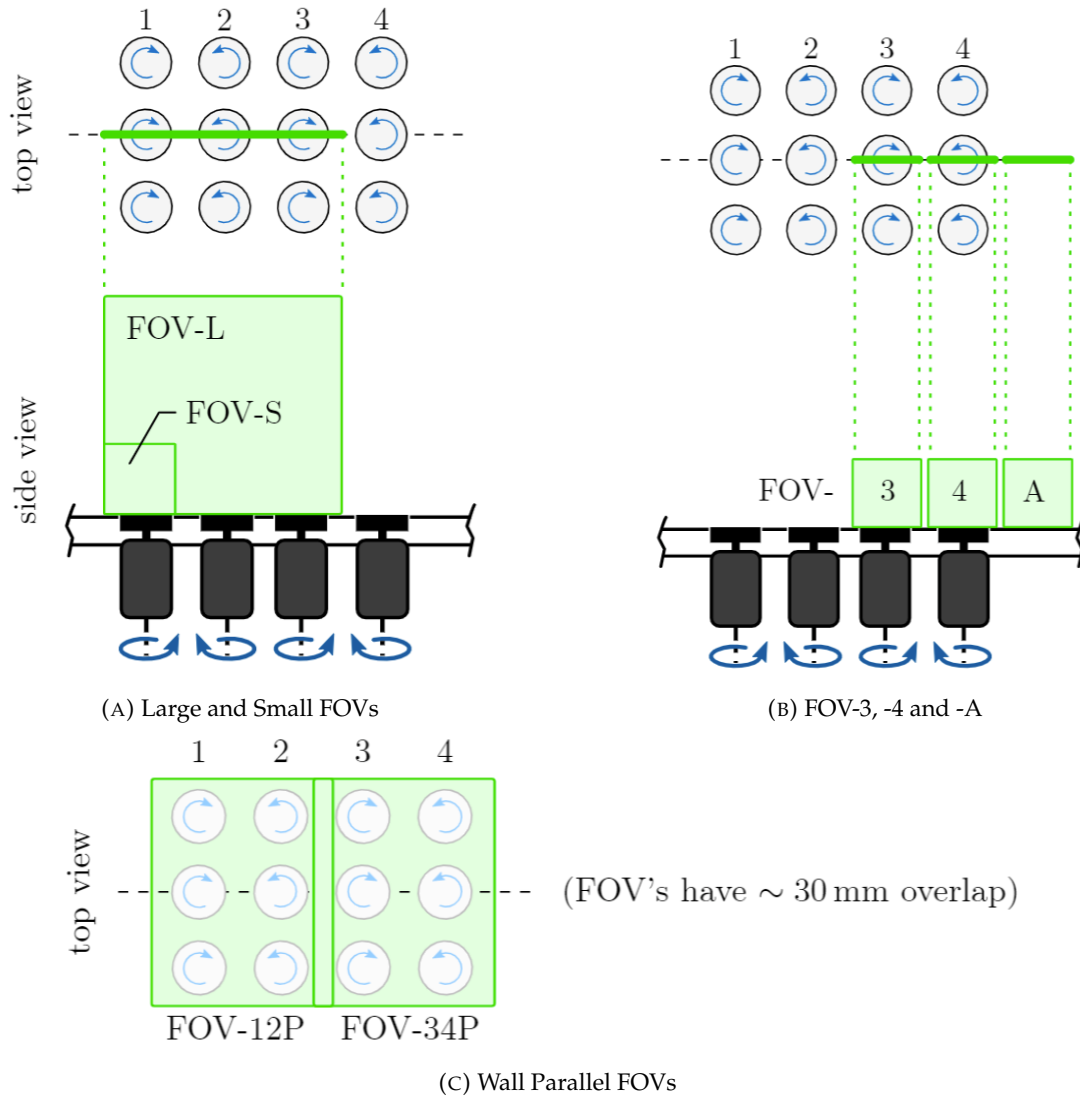


FIGURE 6.2: Configurations of 2D-2C PIV, FOVs in wall-normal plane (a, b) and in the wall parallel plane (c). In all configurations, the sCMOS cameras are located outside of the tunnel, with the optical axis perpendicular to the FOV-planes

### 6.2.3 Non-dimensional Test Matrix

Yet a key issue to solve before moving on with the data acquisition, is which data to acquire in order to satisfy the objectives discussed previously. Recall the definition of the key performance parameters defined by Ricco and Hahn (2013). These are  $D^+$ , the disc diameter, and  $W^+$ , the disc tip velocity. Both of these variables are normalized with viscous scaling. Once the physical dimensions of the discs and the RPM selected have been determined using the method described in Section 5.3, it is possible to generate a test matrix to overlap Ricco's. Initially the RPM values to be tested were

calculated from boundary layer data from Kempaiah et al. (2020). The choice of testing a baseline case ( $W^+ = 0$ ), an optimal RPM ( $W^+ = 10$ ) and a high RPM ( $W^+ = 25$ ) resulted in a selection of RPM for each freestream velocity, all tabulated in column two of Table 6.3. However, following the initial data processing and calculation of the friction velocity from the canonical TBL, it resulted that the RPM tested were not exactly on the optimum but slightly around it. Table 6.3 below provides a summary of this, with the conclusion that in the result section the three cases will be labelled as “Baseline”, “Optimal” and “High” respectively. The slight change in friction velocity moreover had the same effect on the non-dimensional disc diameter, shifting the tested  $D^+$  just slightly off the optimum found by Ricco. The test matrix overlapped to Ricco’s image is presented in Figure 6.3, with the full test matrix found in Appendix B.

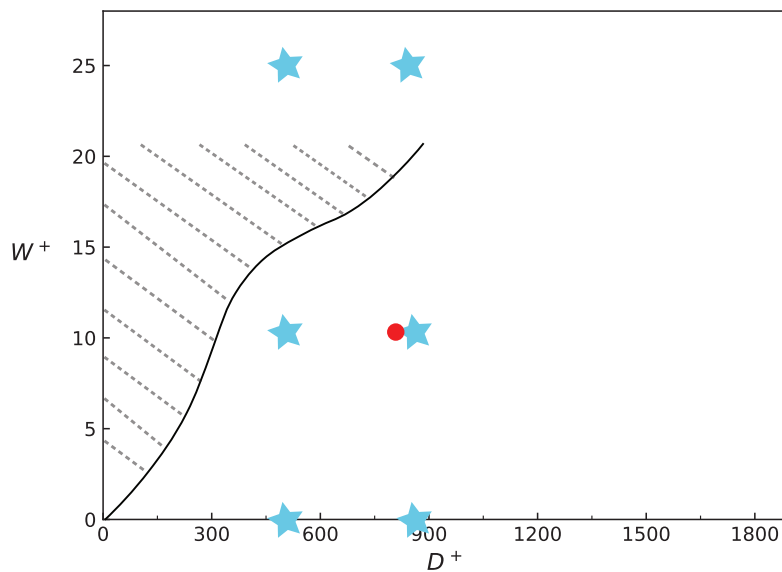


FIGURE 6.3: Non-dimensional test matrix for  $D^+$  and  $W^+$  combinations. RH13’s optimum is found at the red dot, and blue stars represent points tested in in this work.

Flow Velocity $U_\infty$ [m/s]	Set $\Omega$ [RPM]	Expected $W^+$	Actual $W^+$	% change	Nomenclature
3	0	0	0	0	baseline
	550	10	10.4	4	optimal
	1350	25	26.5	5.7	high
5	0	0	0	0	baseline
	870	10	9.9	1	optimal
	2170	25	24.8	<1	high

TABLE 6.3: Non-dimensional disc velocities and relevant nomenclature used in the Results section.

Different fields of view also beget different testing cycles. For example, the full TBL characterization has to be run only once per flow velocity, gathering a total of three datasets. For the over-disk detail, however, each flow velocity accrues three different RPMs to be tested, resulting in nine datasets without accounting for the different camera positions. In total, over 35 datasets were collected.

### 6.3 Data Processing and Reduction

The setup, fields of view and test matrix described up until this point allow the imaging of black-and-white images of the particles. Image processing techniques are performed to convert these images to velocity fields, and data reduction techniques have to be applied to render the data suitable for drawing conclusions.

Reconstructing the velocity field from the above-mentioned images is done with the use of PIV cross-correlation algorithms. Recall that images are taken “in pair” at an interval  $dt$ : any given image pair is divided into smaller “interrogation windows”, the size of which is determined with methods described later. Ideally, the particles present in each window of one image in the pair will be present in the same window in the other image, albeit displaced a certain distance due to the time interval between the two. The computation of this displacement is performed algorithmically with a cross-correlation analysis, where the location of the cross correlation peak with respect to the center gives average displacement of particles within that interrogation window. Knowing the time interval  $dt$  between the images in the pair, the velocity vector can then be calculated for each interrogation window. Repeating this process for all the windows results in the vector field of the entire image.

In practice, there are more steps that can be taken to increase the quality of the images as well as making further processing easier. The following steps have been taken prior to obtaining the velocity fields:

1. **Reorganize Frames:** Two cameras are used to simultaneously capture the flowfield, and the control PC stores the two image pairs in the same “file”. This option allows to decouple the image pairs from Camera 1 from the ones from Camera 2
2. **Subtract Time Filter:** Time filters can be used to remove the background noise from the image by, per pixel, removing the minimum intensity found over a certain time interval. Butterworth filtering can also be used to apply a high-pass filter to the images. In the present work the minimum time filter was applied, taking data from all images in the dataset.
3. **Extract Volume:** Also known as cropping the field of view, this cuts down the image to a pre-determined area while keeping the same amount of pixels. For efficiency reasons, it is not feasible to perform cross-correlation with small interrogation windows across the whole flowfield, and crops can be used to reduced the area used for the vector calculation. An overview of the crops used in this work is presented in Section 6.3.1.

Following this pre-processing, the vector calculation can take place:

1. **Vector Calculation:** The core of PIV, this is the cross correlation needed to transform the raw images to vector fields. Several parameters can be changed to enhance the quality of the data:
  - (a) *Window Size:* decreasing the size of the windows increases noise and spurious pixels, but also resolution. Larger windows “smooth out” the data by averaging over more particles, but lead to shorter processing times.
  - (b) *Window Deformation:* deformations can be applied to the windows to increase resolution in a certain direction. Moreover, circular windows ensure smoother transitions while square ones are more robust.
  - (c) *Number of passes:* the passes following the first one use the previously calculated correlation peak as an initial guess, refining the vector further. As a downside, more passes increase the processing time.

- (d) *Masking*: geometric masking consists of hiding regions deemed invalid for processing, such as very harsh reflections not eliminated in pre-processing steps or the wind-tunnel walls.
2. **Vector Validation**: Effectively a part of the previous step, this process checks for outlier vectors generated by the calculation described above. It is used to detect outliers outside of a  $2\sigma$  bound, which are then deleted and replaced with vectors interpolated from the neighbouring ones.
3. **Vector Statistics**: Postprocessing step used to determine vector averages of the dataset. This includes ensemble averaging the velocities, as well as computing standard deviation and Reynolds stresses.

All further data post-processing and reduction is performed via custom Python scripts.

For most of the datasets considered in this work a multipass PIV algorithm was employed to obtain a higher spatial resolution while still being able to resolve high particle displacements in the outer layers of the boundary layer, which would normally fail if only smaller interrogation windows would be used. The multipass algorithm performs as follows: after the first pass, the interrogation window is offset by the mean displacement of the particles calculated previously, thereby increasing the ratio of matched particle images to unmatched ones and the signal-to-noise ratio in the correlation peak. This permits the use of smaller window sizes (after the first pass) without increasing errors due to particles leaving the interrogation window. In the present work, the first pass always consisted of windows with 50% overlap and 1:1 aspect ratios, allowing particles who appear only in one frame of neighbouring windows to be captured. The pixel window dimensions for the first pass varied between datasets but were always between 48 and 96 [px]. Following the initial pass, two more passes with a 75% overlap and much smaller window sizes were performed. It is important to notice that although this large overlap between interrogation windows leads to more vectors because the vector spacing is diminished, these vectors are not independent from each other and therefore the spatial resolution is not directly improved (Scharnowski and Kahler, 2020). In the second and third pass, non-isotropic elliptical windows were used to increase wall-normal resolution (Scarano, 2003). For the wall-shear calculation, these had an aspect ratio of 4:1, resulting in a size of  $32 \times 8$  pixels<sup>2</sup> ( $0.94 \times 0.24$  [mm<sup>2</sup>]). This represents a 0.12 [mm] of vector spacing. For the full field of view, as well as the wall-parallel planes,  $24 \times 24$  pixels<sup>2</sup> ( $0.7 \times 0.7$  [mm<sup>2</sup>]) windows were used, for a vector pitch of 0.25 [mm].

For the purpose of vector validation, the universal outlier detection algorithm was used (see Westerweel and Scarano (2005)) to remove spurious vectors using a filter of size  $5 \times 5$  [px]. A vector was considered invalid if it exceeded two times the standard deviation of the  $5 \times 5$  group, but reinserted if the residual was less than  $3\sigma$ . The empty spaces would then be filled up with vectors interpolated from the neighbours

### 6.3.1 Cropping

As mentioned previously, it is not efficient to process the entire field of view with small interrogation windows. Regions of interest near the wall can therefore be extracted, and since the amount of pixels within the region remains constant the data captured can be sampled with a much higher resolution. This enables higher spatial resolution for small regions of field of view taking acceptable processing time (Scharnowski and Kahler, 2020).

One particular crop was employed consistently throughout the data analysis process. Spanning the entirety of the field of view and extending approximately 15 [mm] into the flow, this crop is

designed to encompass the entire streamwise extent of the disc, while allowing higher spatial resolution near the wall. The latter is critical in determining second-order statistics such as the Reynolds stresses and the turbulent kinetic energy production.

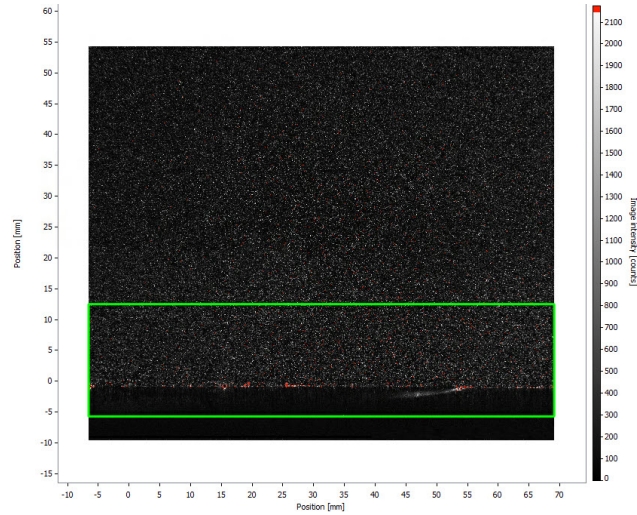


FIGURE 6.4: Horizontal near wall crop

### 6.3.2 Data Reduction

After cropping and processing, it is imperative to obtain the location of the wall to match the mean boundary layer profile. Especially present in near wall measurements, the reflection of the fog particles on the wall produces a symmetric velocity profile with a minimum point of inflection. Furthermore, this point of inflection is not necessarily the zeroed value set by the calibration. As an example, consider Figure 6.5b below, representing the mean flowfield of a 3 [m/s] case within the horizontal wall crop: it appears as the velocity field is almost mirrored across the wall, particularly so near the wall.

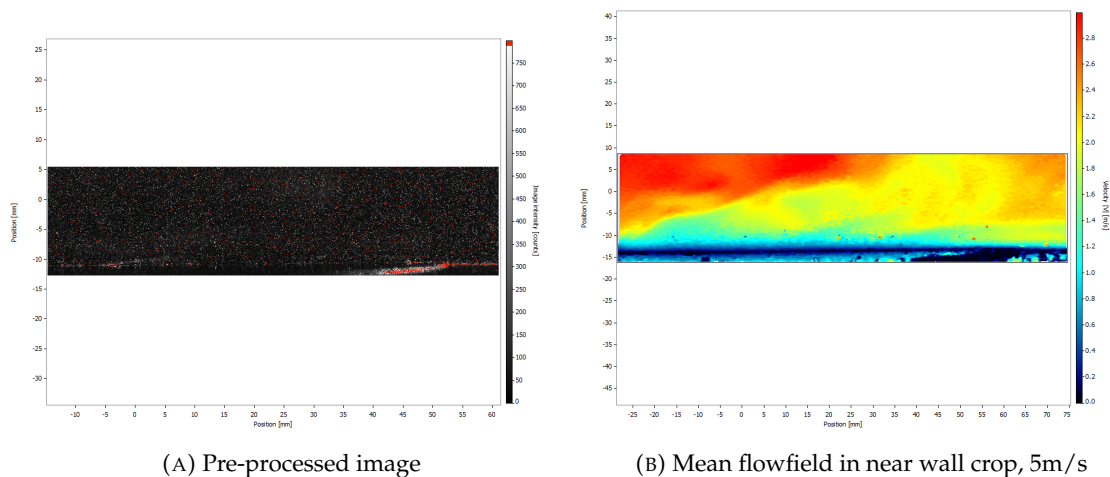
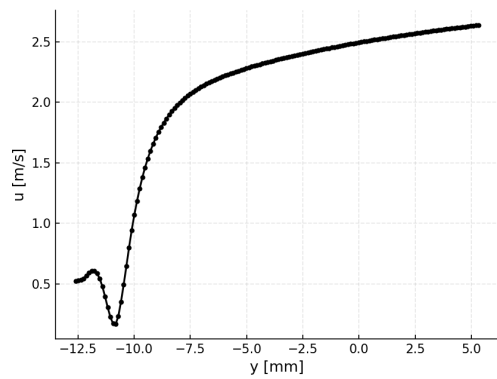


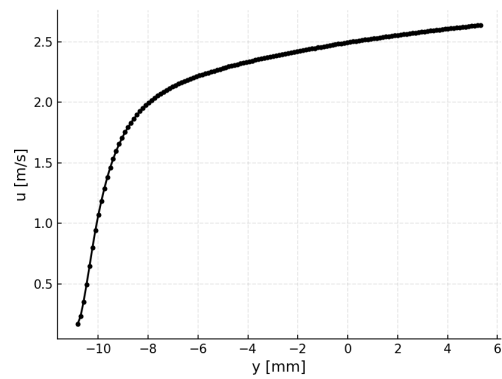
FIGURE 6.5: Extracted volume for near-wall measurements, pre-processed (left) and correlated (right).

If we plot a streamwise average of this profile versus the wall-normal position, we obtain results like Figure 6.6a. The first step in the data reduction is removing the obviously reflected data-points,

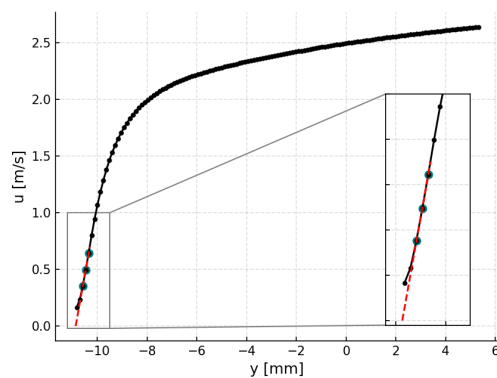
to achieve a figure similar to Figure 6.6b below. This step can be performed algorithmically by finding the inflection point of the mean profile, as well as computing its slope and finding the index of the point just before the slope transitions from positive to negative. The profile that results from this cutoff can now be used to investigate the linear region and offset, by using a Python package providing linear regression models. The used model, `linear_model.LinearRegression` contained within the package `sklearn`, accepts as input a set of  $x$  and  $y$  coordinates and builds a linear regression through them, returning the slope, the  $y$ -intercept (in this case, the intercept at  $\bar{u} = 0$ ) and the R-squared value of the fit. An example of this fit is shown in Figure 6.6c. With the now known intercept it is possible to offset the full boundary layer profile like in Figure 6.6d. Furthermore, we know from PIV principles that each vector is generated at the center of the interrogation window. If any of the points on the below graph ends up between 0 and half of the physical interrogation window size it has to be removed and the slope has to be recalculated with the new points. Kahler et al. (2012) states that single-pixel ensemble-correlation or PTV should be applied below this threshold, but due to practical constraints it was decided to simply discard the points. The slope found via the above described method can also be reused for further data analysis later, as it is effectively  $1 / \left( \frac{\partial u}{\partial y} \right)_{y=0}$



(A) Mean velocity profile before any data reduction.



(B) Inflection cutoff from profile.



(C) Fit found using linear regression through marked points.

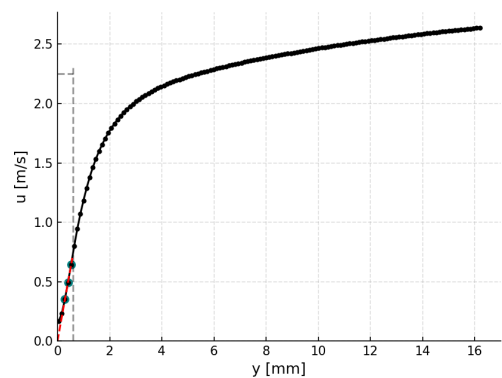
(D) Offset of profile according to intercept, with the linear region ( $y^+ < 5$ ) bounded by dashed line.

FIGURE 6.6: Data reduction steps to make the mean profiles suitable for analysis

For profiles further away from the wall, where the linear region is not resolved with high accuracy, as similar method is employed. The systematic error of this method is higher, but it is as accurate as

determining the inflection point and the offset visually. Furthermore, for very large fields of view such as those captured with the 60mm lens, the exact wall location is often unnecessary as no data of interest is found for  $y^+ < 100$ .

Although the location of the wall can now be computed algorithmically, another question remains about the disc inclination and effects on the local flowfield. It is already known from visual inspection that the discs are not exactly flush with the stationary plate due to a number of reasons. By plotting the vertical velocity distribution over the disc (Figure 6.7) one can clearly notice the location of the disc surface by observing the symmetrical properties of certain parts of the image, leading to the appreciation that the disc is not fully tangent to the  $x$ -axis. For this reason, as well as the large distribution of wall-normal velocity, it was decided to divide the disc surface in 7 individual segments over which the data reduction procedure described above could take place. This would allow the correction for the wall surface for each individual segment, instead of taking the overall mean of the image. Furthermore, variations in turbulence statistics and the disc leading and trailing edge interactions with them can be properly analyzed, allowing for a more comprehensive analysis of the results.

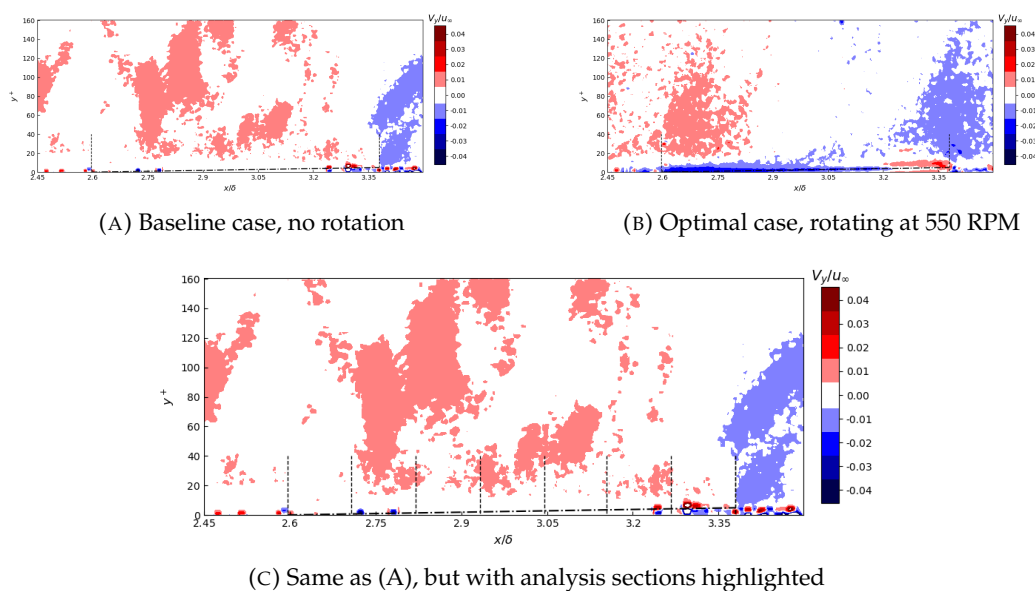


FIGURE 6.7: Normalized wall-normal velocity distribution for 3 [m/s]. Disc leading and trailing edge are marked at  $x = 2.6\delta$  and  $x = 3.38\delta$  respectively. Disc surface is marked with the dash-dotted line.

### 6.3.3 Reconstruction of full boundary layer profile

The characterization of the turbulent boundary layer requires its reconstruction at high resolution. Using data from *FOV-S* it is possible to extract high resolution data up to  $y^+ \approx 500$ . Above this threshold, the second camera with the 60mm Nikkor lens can be employed to capture even the outermost parts of the boundary layer (*FOV-L*). After the datasets have been processed following the steps outlined in the sub-sections above, it is possible to splice them together and describe the entire boundary layer at high resolution. The results of this characterization are presented in the following chapter, labelled for the respective crop.

## 6.4 Uncertainty Analysis

In the present work both averaged data and instantaneous data will be used to describe the various flow fields encountered. Both of these are susceptible to pitfalls in the underlying data, either directly in the case of the instantaneous imaging or propagated through the instant images when considering averages. In the following sections, some of the most significant sources of uncertainty will be discussed along with their impact on the measurements.

### 6.4.1 Statistical Uncertainty

Statistical uncertainty is related to random fluctuations intrinsic to any measurement, originated from the environment, the measurement device or any other random variable present in the experiment. For example, in the wall-parallel measurements, the highly unsteady disc reflections off the edges degrade the local quality of the measurements with what is no more than random noise. To reduce these random fluctuations it is common to capture a large number of samples and then average them in an attempt to achieve the true value of the measured quantity. Statistical uncertainty is therefore related to mean quantities, concerning most of this work.

The statistical uncertainty is calculated as follows

$$\epsilon_u = \frac{\sigma}{\sqrt{N}} \quad (6.10)$$

where  $N$  is the number of samples and  $\sigma$  the standard deviation of the measurements. As per Benedict and Gould (1996), the standard deviation is related to the instantaneous flow oscillations as  $\sigma = \sqrt{u'^2}$ .

### 6.4.2 Interrogation Window Size Uncertainty

Having a finite window size means that any flow feature smaller than the physical window dimensions will not be resolved, and quantities that are resolved will be spatially averaged across the domain. A smaller window leads to higher resolution, but decreasing it too much would lead to a loss of particles between the image pair. This is especially relevant when discussing very small scales of the flow common in viscous interactions. The uncertainty related to this can be calculated as described in Schrijer and Scarano (2008)

$$\epsilon_{ws} = \sin \frac{l_{window}}{\lambda} \quad (6.11)$$

where  $l_{window}$  is the window size.

### 6.4.3 Cross-Correlation Uncertainty

The cross-correlation operation that transforms the particle image pair to a vector field is itself uncertain. According to Raffel et al. (2018), the error for planar PIV is in the order of 0.1 pixels, and can be expressed in terms of flow velocity using the following equation:

$$\epsilon_{cc} = \frac{\epsilon_c}{k\delta_t} \quad (6.12)$$

where  $\epsilon_c$  is the correlation uncertainty,  $k$  the image resolution in [px/mm] and  $\delta_t$  the laser pulse separation.

#### 6.4.4 Particle Tracing Uncertainty

Finally, recall from Section 6.1.1 that the flow velocity is approximated by the particle velocity. This approximation itself, which is then captured by the PIV system, presents an error in the lag between the particle and the flow velocities. This slip velocity is an indicator of how good the particle represents the flow motion, and therefore the uncertainty in the PIV measurements.

The slip velocity (previously described in Equation 6.1) can be estimated as

$$\vec{u}_{slip} = \vec{u}_p - \vec{u}_f = \tau_p \cdot \vec{a}_p \quad (6.13)$$

where  $\tau_p$  is the particle response time and  $\vec{a}_p$  the particle acceleration. Assuming that the particle's motion is dominated by viscous forces, the acceleration of such particle must be the dot product of velocity with its gradient

$$\vec{a}_p = \vec{V} \cdot \nabla \vec{V} \quad (6.14)$$

which substituted back in Equation 6.13 yields

$$\vec{u}_{slip} = \tau_p \vec{V} \cdot \nabla \vec{V} \quad (6.15)$$

and for a two-component velocity field

$$\vec{u}_{slip} = \tau_p \vec{V} \cdot \left( \frac{\partial u}{\partial x} + \frac{\partial u}{\partial y} \right) \quad (6.16)$$

From the above equations, it can be inferred that the maximum slip velocity will be present in regions with the steepest gradients, and therefore the uncertainty can be estimated from the modulo value of the slip velocity.

$$\epsilon_{slip} = ||\vec{u}_{slip}|| \quad (6.17)$$

#### 6.4.5 Uncertainty in numbers

To conclude this chapter, Table 6.4 sums up the uncertainty values calculated using the equations above. Note that the wall-parallel statistical uncertainty is much higher than the wall-normal measurements'. This can be attributed to the larger number of images taken for the latter, while the absolute numbers of standard deviation and fluctuations remain in the same order of magnitude. Moreover, the statistical  $w$  for wall-normal and statistical  $v$  for wall-parallel measurements are not reported due to being out-of-plane components, and therefore not available from planar PIV.

Uncertainty Source	Symbol	Wall-Normal	Wall-Parallel
Statistical $u$	$\epsilon_u$	0.0079 [m/s]	0.021 [m/s]
Statistical $v$	$\epsilon_v$	0.0076 [m/s]	/
Statistical $w$	$\epsilon_w$	/	0.023 [m/s]
Cross-Correlation	$\epsilon_{cc}$	0.03 [m/s]	0.02 [m/s]
Particle Slip	$\epsilon_{slip}$	0.0012 [m/s]	0.0 [m/s]
Interrogation window size (spatial resolution)	$\epsilon_{ws}$	0.0051 [m/s]	0.0025 [m/s]

TABLE 6.4: Report of uncertainty values.

## Chapter 7

# Results and Discussion

The current chapter presents and discusses the results obtained after the data collection and reduction routines have been performed. The chapter begins with a section dedicated to the characterization of the turbulent boundary layer considered in this work. Subsequently, a comparison of the boundary layer with and without disc rotation is presented, discussing mean quantities, Reynolds statistics and instantaneous fields. Moving on to the wall-parallel datasets, a wall-parallel view of the entire disc array is presented and array-wise flow structures are discussed. In the final part of this chapter a methodological description of the drag reduction mechanism is provided, in the context of previous literature and current findings. In this process, the research question of Chapter 1 is addressed.

### Contents

---

<b>7.1</b>	<b>Canonical Turbulent Boundary Layer</b> . . . . .	<b>60</b>
<b>7.2</b>	<b>Wall Shear and Friction Velocity estimation</b> . . . . .	<b>62</b>
<b>7.3</b>	<b>Turbulence Statistics</b> . . . . .	<b>66</b>
	7.3.1 Reynolds Shear Stresses . . . . .	66
	7.3.2 Near Wall TKE Production . . . . .	67
<b>7.4</b>	<b>Quadrant Decomposition</b> . . . . .	<b>68</b>
<b>7.5</b>	<b>Instantaneous Field Organization</b> . . . . .	<b>71</b>
<b>7.6</b>	<b>Over-Array Structure Behaviour</b> . . . . .	<b>75</b>
<b>7.7</b>	<b>Discussion</b> . . . . .	<b>80</b>

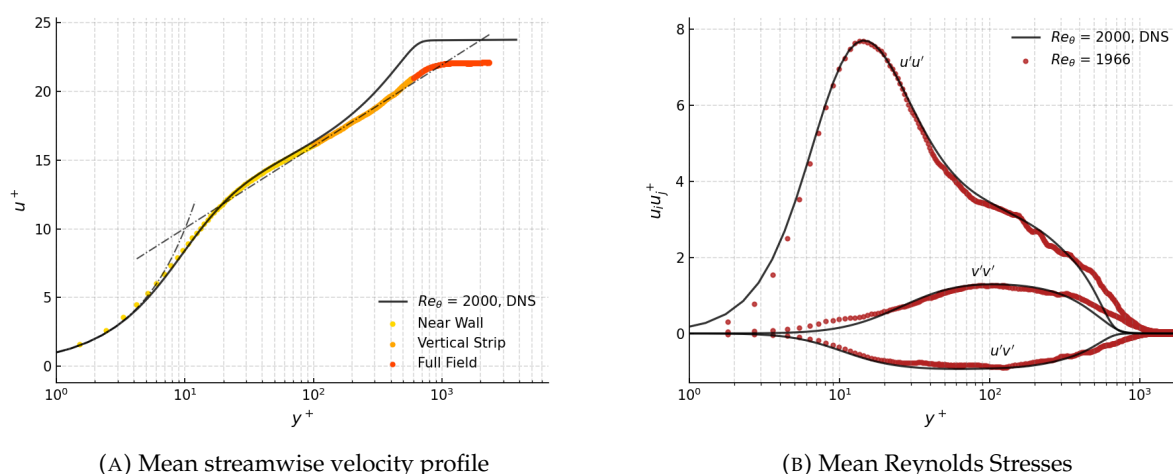
---

## 7.1 Canonical Turbulent Boundary Layer

This section presents the description of the turbulent boundary layer in its undisturbed (without disc rotation) state. It accomplishes two goals. On one hand, it allows to establish the flow characteristics and the flow properties of the nominal scenario created with this windtunnel configuration. On the other hand, it allows to characterize the disc rotation's impact on the flowfield when the controlled TBL is compared to the baseline flow without disc rotation.

The work of Schlatter and Örlü (2010), covering a DNS of a zero-pressure gradient turbulent boundary layer flow, has been used as a comparison of the experimental baseline flow. Alongside this, comparisons are made with algebraic relationships for the linear region ( $y^+ = u^+$ ) and the logarithmic law (Eq. 2.9).

Both the mean quantities and the Reynolds statistics have been obtained through an ensemble average of all the fields captured, as well as applying the data reduction techniques highlighted in the previous chapter and normalizing the axes and data with inner variables.



(A) Mean streamwise velocity profile

(B) Mean Reynolds Stresses

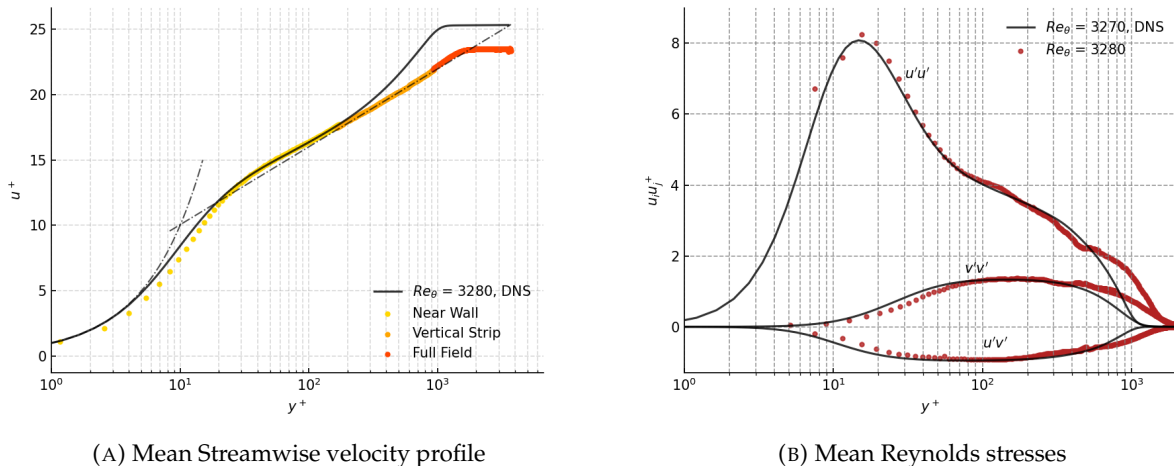
FIGURE 7.1: Characterization of TBL at  $Re_\theta = 1966$ , both profiles normalized with inner variables

Figure 7.1 presents the scaled boundary layer profile and the Reynolds stresses for  $u_\infty = 3$  [m/s] or  $Re_\theta = 1966$ . This plots presented here have been captured over FOV-S (recall Fig. 6.2) for the *Near Wall* and *Vertical Strip* sections of the graph, and FOV-L for the *Full Field*.

The boundary layer profile presented in Figure 7.1a is colored so to distinguish the various crops used to gather information about the full boundary layer at high resolution. Indeed, this profile begins well within the viscous sublayer at a  $y^+$  of  $\sim 1.5$ . Here a linear relationship exists between the wall-normal coordinate and the normalized flow velocity, highlighted in this plot by the dash-dotted line following the profile until approximately  $y^+ = 5$ . Following  $y^+ \sim 40$  there is a well defined logarithmic relationship between the normalized velocity  $u^+$  and the normal wall distance  $y^+$ , seen both from the DNS data and the numerical relationship itself dash-dotted. The profile in this region is slightly curved so that it does not follow the relationship exactly, but it is still an acceptable approximation. Finally, the data points extend all the way to  $y^+ \sim 2500$ . Overall there is good agreement between PIV and DNS data, with the wake component of the boundary layer being the main difference between the profiles. The difference is mainly attributed to the aggressive trip used in this experimental campaign (Chauhan et al., 2009; Marusic et al., 2015). Another likely possibility is that the boundary layer was not strictly ZPG as the cross-sectional area of the test section

was constant and not expanding. This difference however does not impact the conclusions made by this work as the focus is on regions closer to the wall. The high spatial resolution of data-points throughout the entire boundary layer, and especially in the linear region, is attributed to the low friction velocity of this specific test.

Looking at Figure 7.1b, the normalized Reynolds stresses also support the validity of the data collected. The streamwise Reynolds stresses  $u'u'$  are in good agreement with DNS data except for the region nearest to the wall and some deviations in the outer region. Again, the latter phenomenon is attributed to the aggressive transition strip used in this experimental campaign. The values closest to the wall are likely to be lower than DNS due to the averaging effect of the interrogation windows on the very small domain considered. The wall normal Reynolds stress  $v'v'$  also agrees well with DNS, and presents a lower overall magnitude due to the lack of significant variation in the wall-normal fluctuations. Finally, the combination of the wall-normal and streamwise fluctuations is represented in the  $u'v'$  component. This component is negative due to the opposite signs of the fluctuations composing it, and once again it is in good agreement with the DNS solution except for the regions at the edge of the boundary layer.



(A) Mean Streamwise velocity profile

(B) Mean Reynolds stresses

FIGURE 7.2: characterization at  $Re_\theta = 3270$ , both profiles normalized with inner variables

The profile of the TBL at  $u_\infty = 5$  [m/s] ( $Re_\theta = 3270$ ) is presented in Figure 7.2a. Unlike its predecessor, this boundary layer's viscous sublayer presents a slight offset to the DNS data; until  $y^+ = 15$  the normalized velocity is slightly below the DNS results. This subtle differences are attributed to a small wall offset present when calculating the intercept, likely due to the increased complexity in getting valid data points in a "shrinking" viscous sublayer. The logarithmic region is however still clearly defined, extending even further than the previously considered TBL due to scale separation. The agreement of this region with both the DNS data and the log-law is high, and the slight divergence present in the  $Re_\theta = 1966$  boundary layer does not appear in this data. Once again, the boundary layer extends all the way to the wake region at  $y^+ \sim 3700$ , again offset from the DNS data. The Reynolds stresses in Figure 7.2b also present good agreement with DNS data. The wall-normal and combinations,  $v'v'$  and  $u'v'$  respectively, have a good agreement until the outer parts of the boundary layer: once again the trip proves to be too aggressive for the data to match the DNS perfectly. The streamwise stresses  $u'u'$  are also in relatively good agreement, although the higher flow velocity means that the near wall characteristics cannot be full explored, with the first valid data point only present at  $y^+ = 8$ . The peak of the stresses however has good correlation with DNS.

The comparison of the collected TBL data with DNS and algebraic laws show that the boundary layers collected are indeed canonical with the literature, and further analysis can now be performed to extract more quantitative information.

The turbulent boundary layer properties are therefore tabulated in Table 7.1.

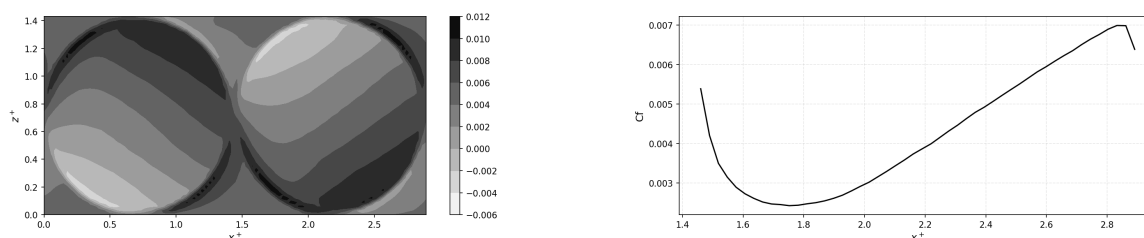
$u_\infty$ [m/s]	$\delta_{99}$ [mm]	$\delta^*$ [mm]	$\theta$ [mm]	$Re_\theta$	$u_\tau^\dagger$ [m/s]	$u_\tau^\ddagger$ [m/s]	$Re_\tau$	$H$
3	87.0	16.75	8.78	1966	0.154	0.152	912	2.033
5	90.2	18.75	9.01	3280	0.218	0.241	1483	2.083

*note* †refers to values computed using the linear region of the profile,  
‡refers to values computed using the Clauser plot method

TABLE 7.1: Turbulent Boundary Layer properties. The friction Reynolds number has been calculated using the  $u_\tau$  from the linear region.

## 7.2 Wall Shear and Friction Velocity estimation

After the characterization of the nominal turbulent boundary layer it is now possible to evaluate the effect of the rotating discs on the former. As mentioned in the data reduction section, the imaged domain over the fourth center disc has been divided into 7 streamwise segments of equal size, each of which can be analyzed independently. This allows for taking into account the streamwise variation of the mean skin-friction over the extent of the disc. The typical variation of mean skin-friction is visualized in Figure 7.3a.



(A) Contours of time-averaged skin-friction coefficient (B) Streamwise evolution of  $C_f$  over the second disc's centerline. (Levoni and Modesti, 2021).

Starting from a purely qualitative analysis, plots of the boundary layer affected by the disc rotations can be made by plotting velocity versus wall-normal distance. These are presented in Figure 7.4 below, with the Reynolds number increasing from left to right.

The different lines in the figures represent the various sections over the disc. Although it is quite hard to discern details from this, qualitatively one can already notice patterns in the various bundles. So far it is not possible to comment on the slope at the wall as the lines overlap each other and there is no information on the linear region, but between  $y^+$  values of 20 and 80 there is a clear trend showing that the High RPM experiences a higher mean velocity than the Optimal and Baseline. A fuller turbulent boundary layer, corresponding to a shift up of the mean velocity profile, has been stated by Choi and Clayton (2001) (among others) to compliment a reduction in the mean velocity at the wall. The decrease in skin-friction coefficient arising from this reduces the mean mass flow rate close to the wall and the mean velocity profile shifts up to compensate for this. It therefore appears that the momentum deficit has decreased for both the Optimal and High case at

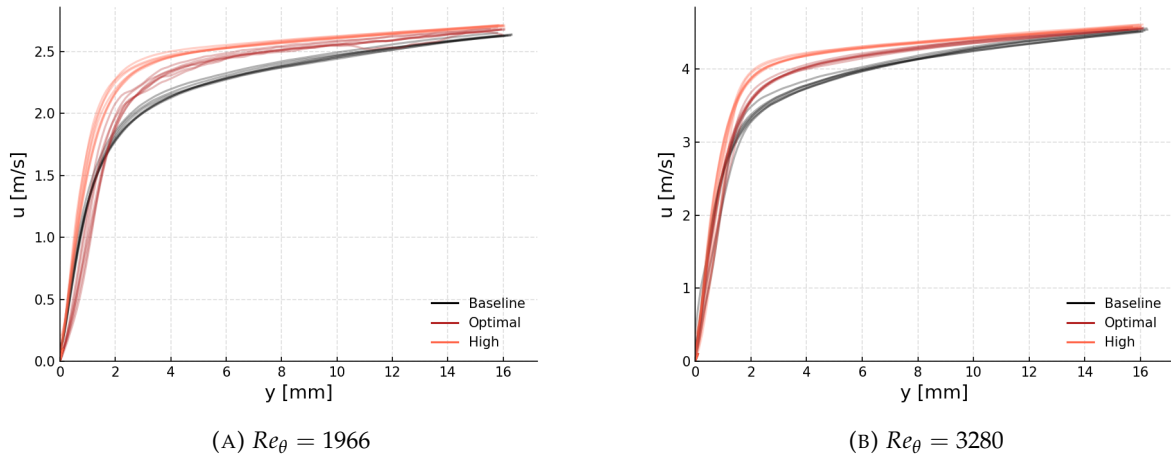


FIGURE 7.4: Comparison of wall-normalized boundary layer profiles, extracted from each section of FOV-4 as described in Section 6.3.2.

both Reynolds numbers. To offer more insight, the momentum thickness can be computed for the three different profiles as indicated by Eq. 2.3, and using the maximum velocity from the graph as  $u_\infty$ . The undisturbed boundary layer has a momentum thickness of 1.55, while the other two profiles have 1.21 and 1.05 respectively for Optimal and High. This quantitatively shows that the flow momentum has greatly increased for the High case, followed closely by the Optimal.

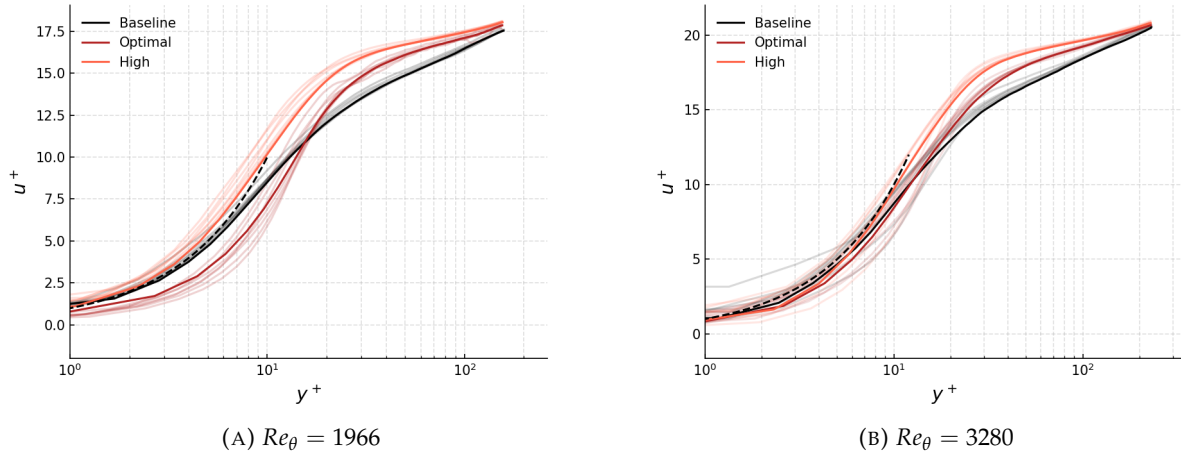


FIGURE 7.5: Comparison of wall-normalized boundary layer profiles on semilogarithmic axis.

Following the previous observations, the profiles presented in Fig. 7.4 can be scaled using inner units and plotted on a semi-logarithmic axis, resulting in Figure 7.5. The friction velocity used for scaling corresponds to the baseline (no rotation) case, so that difference in the linear region can be highlighted for all the various rotations. Furthermore, the profiles are plotted on semi-logarithmic axes to enhance the visualization of behaviour close to the wall. The bundles still represent the various sections over the disc, yet this time the mean has been highlighted to emphasize the overall behaviour of the flowfield over the disc.

It is immediately clear that for both Reynolds numbers the profiles collapse deep into the logarithmic region, with the most differences being present at the wall. Comparing the various profiles on the left-side case ( $Re_\theta = 1966$ ), the High RPM setting shows the profile much closer to the wall than the baseline until  $y^+ = 60$  while the Optimal RPM is shifted further away from the wall. The linear region is highlighted with a dashed black line, further emphasizing the differences between the three rotation settings. The buffer layer also presents interesting changes, thickening and extending to larger  $y^+$  values for both cases. A similar comparison can be done for the higher Reynolds number case on the right. Despite the linear region being harder to discern near the wall at these Reynolds numbers there is some clear patterns in the rotating disc cases being lower than baseline for the mean.

These changes in the linear region occur despite the profiles in Figure 7.4 showing a reduction in momentum deficit. A plausible explanation for this is that at High RPM the slight disc misalignment causes an increase in wall-normal velocity oriented towards the wall, much like the effect of suction over the disc. The velocity between the disc edge and the stationary wall (disc-gap velocity) generates a low pressure area in the gap, thereby resulting in a suction peak at the trailing edge of the disc (see the comparison in Figure 7.6). This ends up having a local detrimental effect on the mean skin-friction, much like pure wall suction (Antonia et al., 1995).

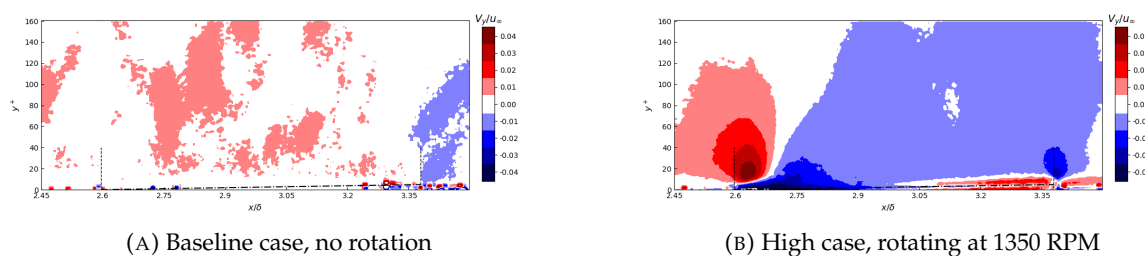


FIGURE 7.6: Wall-normal velocity contours over the fourth disc. Measured at  $Re_\theta = 1966$ ,  $W^+ = 0$  (A) and  $W^+ = 25$  (B).

To extract skin-friction coefficient data from the Figures presented previously we can use Equation 7.1 to calculate the skin-friction from the friction velocity, which itself has been extracted from the slope at the wall where more than two data-points exist within the linear region ( $y^+ < 5$ ). This condition is satisfied for both cases analyzed in this work.

$$C_f = 2 \left( \frac{u_\tau}{U_0} \right)^2 \quad (7.1)$$

$$u_\tau = \sqrt{\frac{\partial \bar{u} / \partial y}{\nu}} \quad (7.2)$$

The data processed for the various RPMs has been collected in Table 7.2 and shown graphically in Figure 7.7 below.

Figure 7.7 shows the skin-friction coefficient calculated for each different disc section for the three RPMs, at  $Re_\theta = 1966$ . Furthermore, the mean of all the sections is represented by the horizontal line. As could be qualitatively extrapolated from Figure 7.5a, the average skin-friction coefficient of the Optimal case is much lower than baseline while it is slightly higher for the High case.

Before getting excited at the big numbers presented in the table below, please note that the numbers reported in the are calculated with the mean value extracted from the figures above, and as such it does not represent the most detailed view on the skin-friction change over the entire array. These

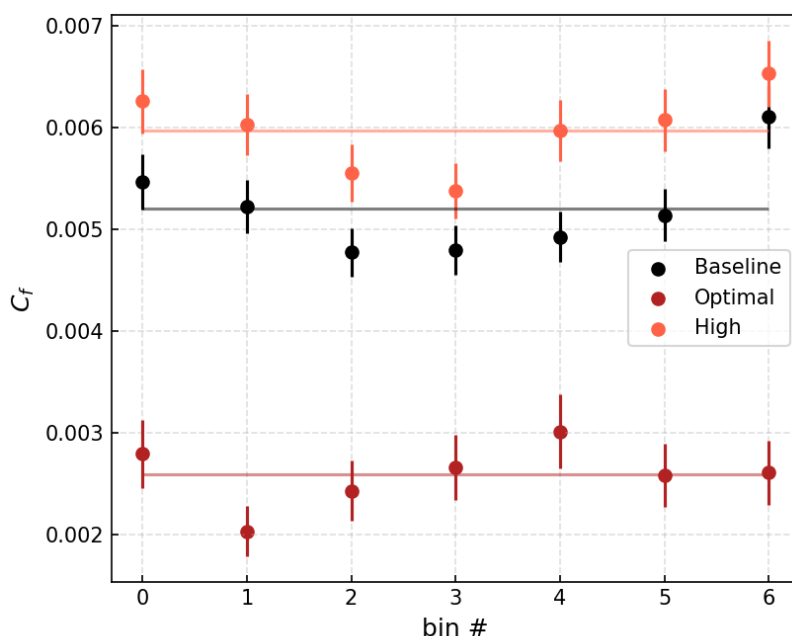


FIGURE 7.7: Skin-friction coefficient calculated using Eq. 7.1 per section,  $Re_\theta = 1966$

are merely local values of skin-friction calculated over the centerline of the last disc. It will be the aim of later sections to explore their applicability to the entire array.

Flow Velocity $U_\infty$ [m/s]	$W^+$	$\Omega$ [RPM]	$u_\tau$ [m/s]	$C_f \times 10^{-3}$	Percent change to baseline
3	0	0	0.153	5.21	0
	10	550	0.108	2.59	-50.3%
	25	1350	0.164	5.97	14.6%
5	0	0	0.215	10.31	0
	10	870	0.201	9.04	-12.3%
	25	2170	0.209	9.98	-3.6%

TABLE 7.2: Skin Friction coefficient and change to baseline for tested datasets. Data is mean of sections from Figure 7.7, captured over the last central disc.

For the flow at  $Re_\theta = 1966$  the skin-friction coefficient decreases by  $\approx 50\%$  for the optimal case and increases by  $\approx 15\%$  for the higher RPM. For the cases at  $Re_\theta = 3280$  the behaviour is slightly different, with both the rotation velocities resulting in local skin-friction drag decreases.

These results are in agreement with Ricco and Hahn (2013), at least in terms of patterns seen. Recall Figure 6.3, where Ricco's drag reduction values were reported for the parameter space tested. Given the shape of the drag-increasing domain, it is very likely that at  $D^+ = 555$  the high RPM would have also resulted in a drag increase if Ricco had performed a simulation on that case. On the other hand, the high value of  $W^+$  for  $D^+ = 900$  returns in some borderline area between drag increase and decrease. Given the trend of drag increase as  $W^+$  increases for fixed  $D^+$  it is not surprising that the high RPM has a lower drag reduction value than the optimum. It is also possible, as discussed, that the drag increase is due to the suction induced at high disc-rotation rates.

Now that the changes in skin-friction coefficient have been quantified, it is productive to delve into the fluctuations present in the turbulent boundary layer and analyze their behaviour, so that they may shed some light on the physical effects taking place in the flowfield.

### 7.3 Turbulence Statistics

The fluctuations in the streamwise and wall normal directions, respectively  $u'$  and  $v'$ , contribute directly to the Reynolds stresses, a mathematical construct obtained as a by-product of the Reynolds decomposition of flow variables. These fluctuations are tied with the coherent structures present in the TBL, and allow for the derivation of information directly tied to the dynamic variation of the TBL. For example, the production of turbulence as well as quantitative information about quadrant events such as ejections and sweeps can be ascertained from this.

#### 7.3.1 Reynolds Shear Stresses

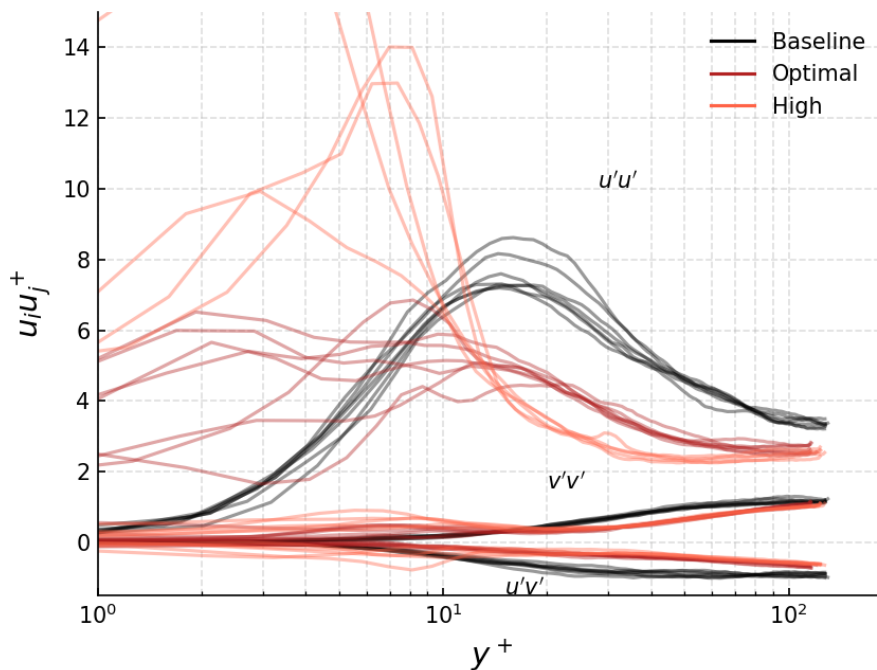


FIGURE 7.8: Mean streamwise Reynolds stresses for each section over the disc,  $Re_\theta = 1966$ .

The Reynolds stresses presented in Figure 7.8 present several changes between the various rotations and the baseline. Firstly, it is important to notice how the streamwise Reynolds stresses for all the sections for the baseline case collapse nicely both at the wall and away from it, with some changes present only over the peak. This is reminiscent to the stresses presented in Figure 7.1b, both in magnitude and behaviour. What is interesting is that the other two cases don't particularly abide by the same patterns, with the Optimal case presenting a deviation from a uniform trace when moving closer to the wall. Below  $y^+ = 20$ , all the various sections of the disc diverge and don't show a uniform peak. Likewise for the High case, below the same wall-normal location the streamwise

Reynolds stresses become spurious and with over-exaggerated peaks. Above  $y^+ = 20$  however both of these cases collapse for all the sections, resulting in a mean streamwise Reynolds stress some 20% lower than the Baseline case. Interestingly, after a crossover point at  $y^+ \approx 15$ , the High case displays lower streamwise Reynolds stresses than the Optimal throughout the entire range of wall-normal locations. Furthermore, both rotating cases present much higher streamwise stresses at the wall than baseline; while this might be attributed to some processing difference between them, it is further supported by literature (Ricco and Hahn, 2013) that the disc-stresses contribution to the overall Reynolds stresses brings the  $u'u'$  component much higher at the wall. The movement of the discs is superimposed on the mean flow in much a similar way to how the actual flow fluctuations are. A further speculation for this behaviour could be related to the imaging technique employed (Scharnowski and Kahler, 2016). The particles at the leading and trailing edge of the disc are moving out of and into the plane, respectively. They do so with a velocity  $\frac{D_0}{2\pi}\Omega$ , which corresponds to 4.8 [m/s] and 12 [m/s] for the Optimal and High case, respectively. Given that a 200 [ $\mu$ s] time interval was used to capture an image pair, a particle at the leading/trailing edge of the disc would have travelled out/into the imaging plane approximately 0.96 [mm] or 2.4 [mm], depending on the RPM tested. Given that the imaging plane depth of field was approximately 2 [mm], it is very possible that particles at the edges of the disc have moved too much to give realistic results for second order statistics such as the above.

Both the optimal and high case appear to decrease the wall-normal stresses with an inflection in the profile after  $y^+ = 20$ , but a peak above baseline below  $y^+ = 10$ .

### 7.3.2 Near Wall TKE Production

The production of turbulent kinetic energy (TKE) is an essential part of determining the reasons behind the changes in wall shear stress because it can be linked to the turbulent skin-friction generation, following Fukagata et al. (2002). It is calculated as

$$\mathcal{P} = -\overline{u'v'} \frac{\partial \bar{u}}{\partial y} \quad (7.3)$$

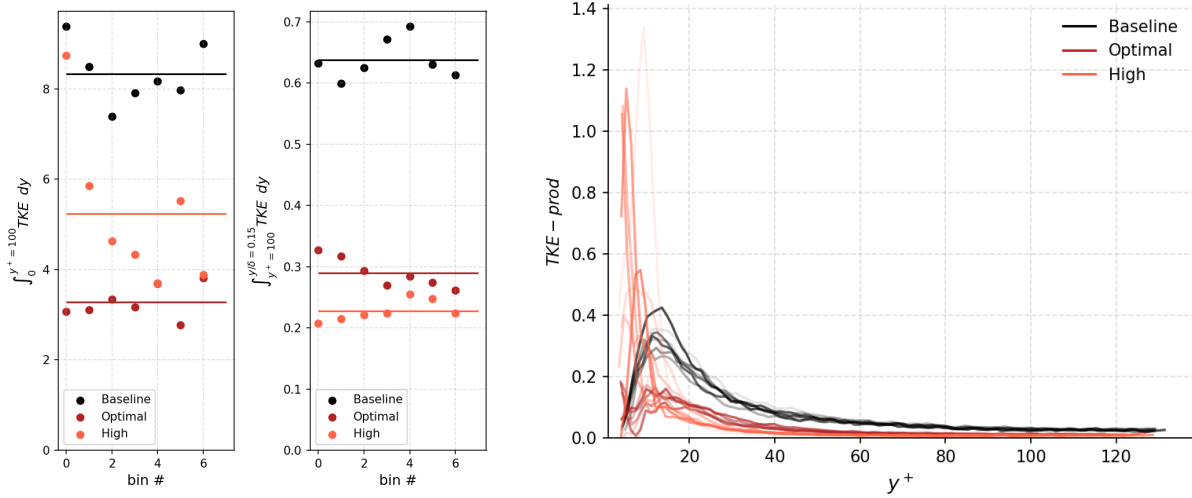
and in this work will be normalized with outer variables  $u_\infty$  and  $\delta_{99}$ . Furthermore, within this work the derivatives of the velocity have been calculated using first order accurate central differences of the mean velocity profiles.

The following plots then present the turbulent kinetic energy production, defined as

$$\text{TKE-prod} = -\frac{\delta_{99}}{u_\infty^3} \overline{u'v'} \frac{\partial u}{\partial y} \quad (7.4)$$

for each section of the disc. Furthermore, each of these lines has been integrated for an inner region (defined from the lowest  $y^+$  sampled to  $y^+ = 100$ ) and an outer region defined from  $y^+ = 100$  to  $y/\delta = 0.15$ . The results of these can be seen in Figure 7.9a.

A few remarks can be made about the above. Firstly, across virtually all the disc sections, the peak of TKE production is highest for the High case, followed by the Baseline and Optimal cases, in that order. This can be seen near the wall in sub-figure 7.9b. These peak reductions can be noticed in the regions closest to the wall, followed by a collapse in TKE production at different rates for the different RPMs. The peak reductions for both High and Optimal RPM follow the trends described so far, with percent changes closely matching the skin-friction ones described in Table 7.2. The variation in peak for the High case is extremely high, but the mean of this is  $\approx 20\%$  higher than baseline, possibly leading to the increase in wall shear stress  $\tau_w$  and the consequent increase in skin-friction drag. The optimal case on the other hand is around 50% lower, coinciding with the



(A) Integrals of TKE production per disc section near the wall (**left**) and in the logarithmic region (**right**). Horizontal lines represent the mean value for given rotation regime. (B) TKE Production versus wall-normal distance. Lines represent the various disc-sections for relevant rotation.

FIGURE 7.9: Turbulence Kinetic Energy Production normalized by outer variables  $u_\infty$  and  $\delta_{99}$  for  $Re_\theta = 1966$ .

drag reduction calculated via the skin friction coefficient. This reduction is a consequence of the  $u'v'$  stress component and the slope of the near-wall mean streamwise velocity.

In an attempt to reduce the locally strong variations in the profiles, the local TKE-production can be integrated to describe the bulk TKE-production over each section. Figure 7.9a presents the integrands of TKE production over the two domains described above. The integrand for the High case presents a lower TKE production than baseline for all disc sections besides the one closest to the leading edge. In the logarithmic region this trend is exacerbated, with the mean value of the High case falling even below the Optimal, and both of them being still below baseline. This behaviour reversal is very similar to what had been shown in Figure 7.8, and once again highlights how the detrimental effects of the high RPM disc rotation are shown only near the wall.

From both the Reynolds statistics analyzed so far it appears clear how the skin-friction increase phenomenon found for high rotations is very much confined at the wall, whereas away from it all quantities that indicate a change in wall-shear are lower than both Baseline and Optimal cases. To shed more light on this phenomenon we can now look at the turbulent fluctuations and their distribution across a quadrant plot.

## 7.4 Quadrant Decomposition

The changes observed in the Reynolds stresses and the TKE production can be further assessed using probability density functions of the streamwise and wall-normal fluctuations  $u'$  and  $v'$  at various wall-normal distances. Furthermore, this will allow us to identify changes in sweep and ejections, critical creators of turbulent skin-friction.

The plots presented in this work are obtained for  $Re_\theta = 1966$  at a selection of  $y^+$  values, as highlighted in Figure 7.4. These locations were chosen within the buffer and logarithmic layers due to the high frequency of sweeps and ejections. At higher values of  $y^+$  the fluctuations seen would be events that have occurred upstream of the acquisition location, therefore not shedding much insight over the flow physics over the disc. Once again, this data is “smoothed out” by being acquired over the entire disk, a domain in which it is known there are flowfield changes.

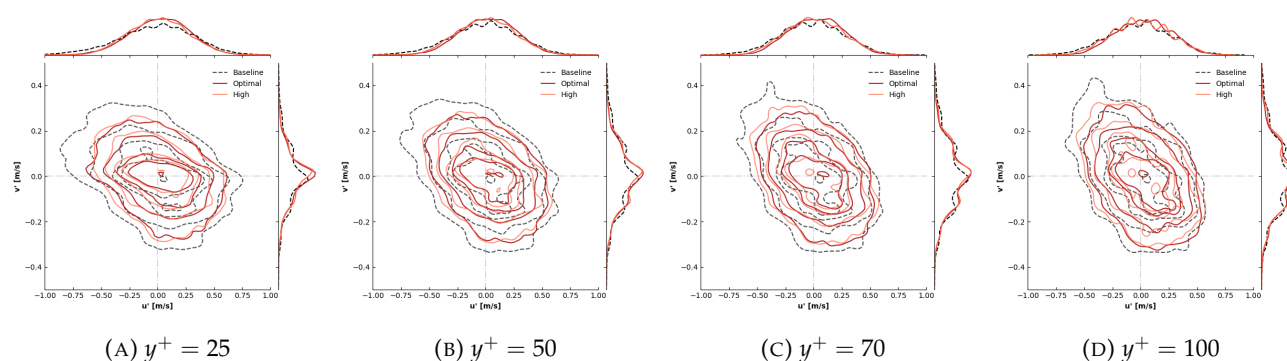
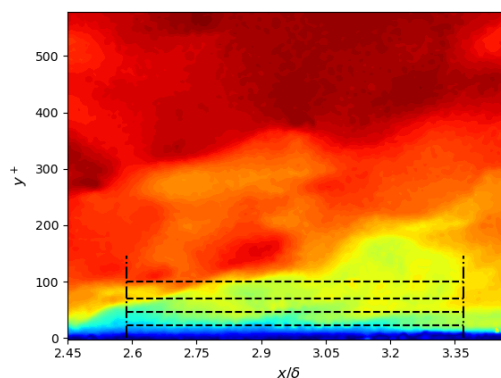


FIGURE 7.10: Probability Density Function of streamwise and wall-normal velocity fluctuations for a selection of wall-normal locations.  $Re_\theta = 1966$ .

The above plots present a bivariate distribution of  $u'$  and  $v'$ , with the streamwise fluctuating component on the horizontal x-axis and the wall-normal component on the vertical y-axis. The 2-dimensional plot in the center can be divided into quadrants by the thin dash-dotted line, separating events in  $Q_2$  (ejections) and  $Q_4$  (sweeps), much like Figure 2.7. The trend seen throughout the range of  $y^+$  is that the bivariate distribution tends to compress along the x-axis and extend on the y-axis, “turning” the potato-like shape. This occurs for all disc rotations, and it is clear it is an underlying phenomenon of any turbulent boundary layer. Closer to the wall the fluctuations are dominated by streamwise low-speed streaks and similar streamwise-oriented features. Away from the wall more phenomena like sweeps and ejections take place, clearly shifting the potato plot on an axis running through  $Q_2$  and  $Q_4$ .

Focusing on the case closest to the wall, it can be noticed how the baseline case has fluctuations spread out throughout the entire range both in the streamwise and wall-normal direction. For both the Optimal and High case however, these fluctuations decrease in frequency and thereby form a tighter peak around 0 for both  $u'$  and  $v'$ . These peaks are present at approximately the same location for both RPMs, implying that over the disc there is no direct effect on fluctuations dependent on disc rotation, at least at this wall-normal location. Moving away from the wall removes this defined peak, smoothing out the rotating cases’ fluctuations at the peak, and removing mostly the ones at the extremes. The trend seen throughout these plots seem to imply that the effect of the disc rotation is seen mostly closer to the wall and that information does not travel very far in the wall-normal direction. However it is important to consider that at the highest  $y^+$  considered the fluctuations might be generated before the disc and analyzed here due to the convection velocity of the flow.

To visualize this effect more thoroughly, it is interesting to introduce the concept of two-point spatial correlations. These techniques are often used to identify the strength and spatial extent of coherent motions within a turbulent boundary layer, and have been previously used to construct general theories regarding turbulence structures (Sillero et al., 2014; Hwang et al., 2016; Kevin et al., 2019). The correlation coefficients used in this work are computed in a similar way to Sillero et al. (2014), where the autocorrelation coefficient is computed in Fourier space and converted back to real space to compare results.

The normalized correlation coefficient is defined as

$$\rho(\Delta x, y_{signal}, y_{ref}) = \frac{\langle \mathcal{R}(x, y_{ref}) \cdot \mathcal{S}(x + \Delta x, y_{signal}) \rangle}{\sqrt{\langle \mathcal{R}^2 \rangle \langle \mathcal{S}^2 \rangle}} \quad (7.5)$$

where  $\langle \dots \rangle$  represents an ensemble average over all the captured images and  $\mathcal{S}$  and  $\mathcal{R}$  are the signals (in this case, the velocity fluctuations) at the various reference  $y$  and “travelling”  $y$  locations,  $y_{ref}$  and  $y_{signal}$  respectively. Practically, the numerator of the above was computed by

$$\hat{C} = \hat{\Psi}(u'_{ref}) \hat{\Phi}^*(u'_{sig}) \quad (7.6)$$

where  $\hat{\dots}$  is the Fourier transformation and the asterisk represents the complex conjugation.

The outcome of this process is a map of correlation coefficients for a given reference wall-normal location, such as the one presented in Figure 7.11a below. With the highlighted threshold at 0.1, this map shows an angled correlation in  $u'$  values extending way down close to the wall. For comparison, Figure 7.11b is the same correlation map but with the discs rotating at the optimal RPM. It is immediately noticeable how the extent of the 0.1 threshold, as well as the grey background surrounding it, is much reduced in the near-wall regions. The inclination of the correlated feature is still present, highlighting a key behaviour in the structures present in turbulent boundary layers.

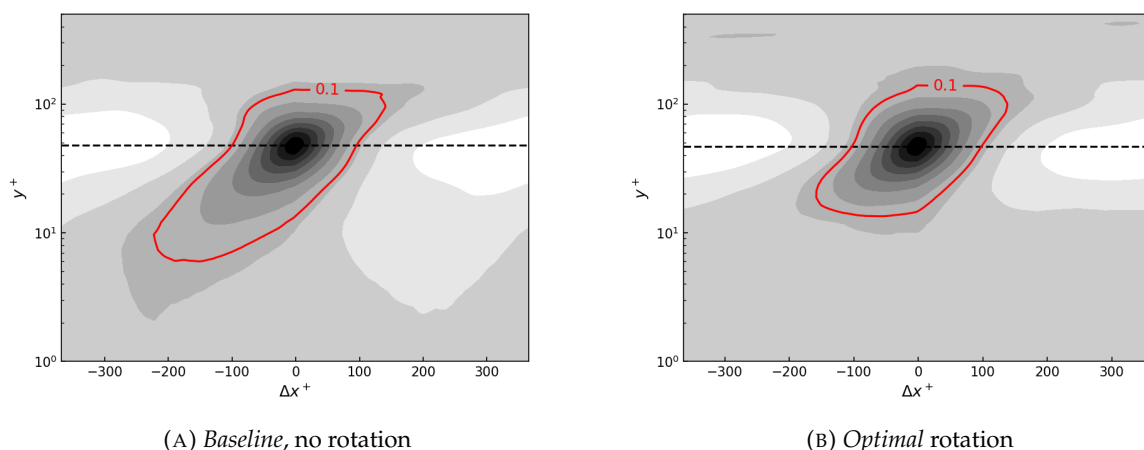


FIGURE 7.11: Two-point cross correlation map of  $u'$  at  $y^+ = 50$ .

From this simple comparison it appears that the discs are effectively decreasing the coherence of streamwise velocity fluctuations close to the wall, which would lead to a decrease in sweeps and other turbulence producing events. To further appreciate this behaviour is possible to select the same  $y^+$  values considered in the PDF plots described above and plot the threshold for every RPM considered at each wall-normal height. The results are as follows in Figure 7.12.

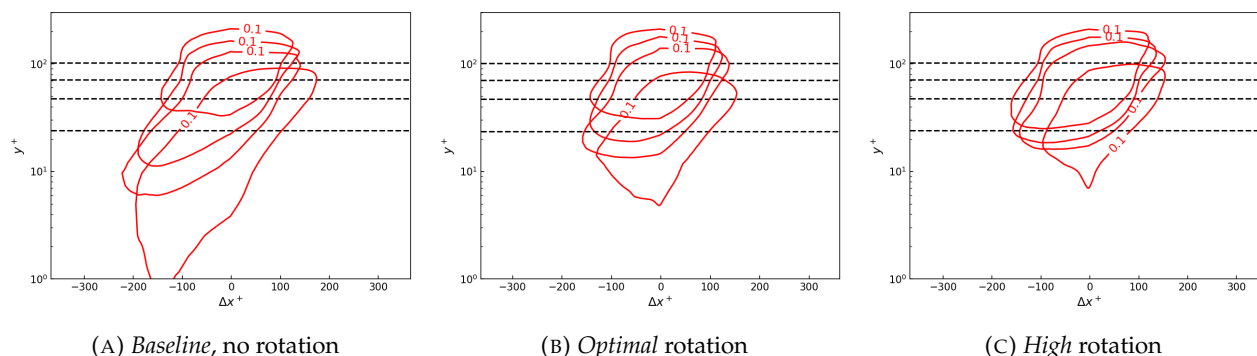


FIGURE 7.12: 0.1 threshold contours of two-point correlation coefficients for  $u'$  fluctuations. Captured at  $y^+ = 25, 50, 70, 100$  from bottom to top. Axis normalized with viscous units.

Here the most noticeable changes occur between the no rotation and rotation cases. Especially at the lower values of  $y^+$ , the coherence stops much more abruptly and away from the wall instead of dipping down into the inner layers. This effect is seen primarily at  $y^+ = 25$  and  $50$ , almost completely disappearing over  $70y^+$  and leading to the hypothesis that the disc effect is seen primarily in the inner regions of the boundary layer, not propagating much further than the very beginnings of the logarithmic layer. In these inner layers the discs are having a clear effect on the streamwise velocity fluctuations, clearly diminishing them in magnitude and frequency. The lack of major differences between the Optimal and High case also supports the hypothesis that the higher disc rotational velocities appear to underperform due to the suction present very close to the disc. A note of caution to present here is that the view presented in this chapter is limited to a single streamwise wall-normal plane. This severely limits the extent of the coherent structures that can be visualized, as they are generally highly three dimensional (Sillero et al., 2014). It is very possible that over the discs such structures become spanwise-inclined, but here we can only see a “cut-out” of them.

## 7.5 Instantaneous Field Organization

The effects discussed until now can be further analyzed in depth by looking at the instantaneous field organization. The data presented in this section has been captured for the full field of view over disc 4 at  $Re_\theta = 1966$ , and presents an evolution of the out-of-plane vorticity ( $\omega_z$ ) topology with increasing RPM. As discussed in previous chapters many coherent structures can be identified in the following fields, with the three main features of interest highlighted in the descriptive figure below.

The structures presented in Figure 7.13 above can be described as follows:

- (1) Hairpin heads depicted as strong negative vorticity, and inclined at angles between  $25^\circ$  and  $45^\circ$  (Adrian, 2007). This region contains a hairpin packet, defined as several hairpins closely following each other.
- (2) The wake and outer layer vorticity signatures are generally background vorticity. This has been described by Eitel-Amor et al. (2014) to accelerate the decay of turbulent coherent structures closer to the wall.

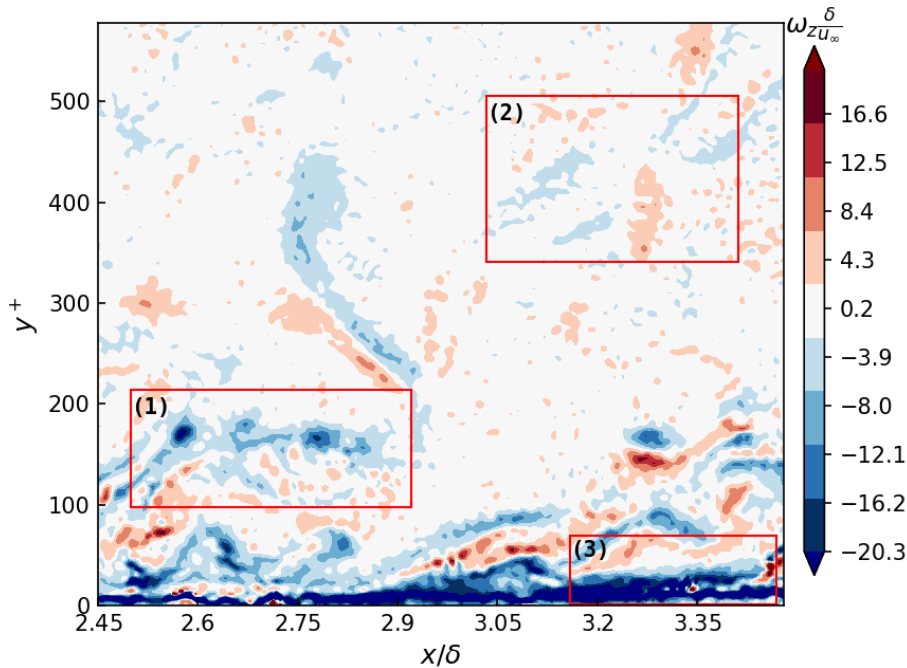


FIGURE 7.13: (1) Hairpin vortices heads, (2) wake layer vorticity signatures, (3) viscous sublayer.

- (3) The viscous sublayer is where the shear is highest, as the velocity decreases to 0 at the wall. This is reflected in the vorticity contours by the strong negative sign. Above this there are inclined vorticity signatures indication sweeps and ejections from the near-wall region. Adrian (2007) describes them as flow in the viscous sublayer being lifted between the legs of hairpin vortices.

Based on the features mentioned above we can qualitatively analyze a selection of pictures.

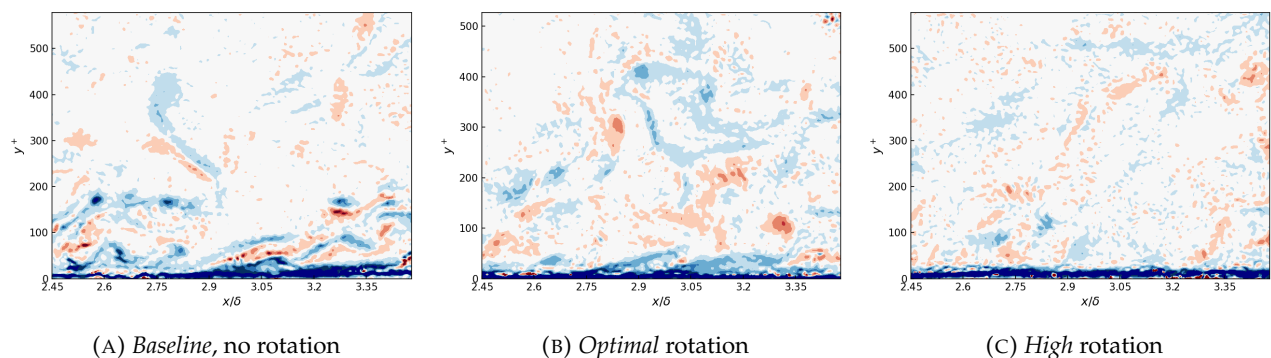


FIGURE 7.14: Instantaneous fields captured at  $Re_\theta = 1966$  and colored by vorticity.

As the disc rotation increases (from left to right in Figure 7.14), the inclined vortical structures at the wall decrease in magnitude and frequency, culminating in them fully disappearing for the High rotation case. As these structures are purported to appear due to turbulence producing events

within the turbulent boundary layer, a reduction in their frequency should represent a reduction in turbulence producing events, something consistent with the PDF from Section 7.4. Likewise, the amount of hairpin vortices present also decreases throughout the images, with the characteristic “heads” not being noticeable anymore. Increasing the rotation furthermore increases the amount of vorticity signatures in the boundary layer outer and wake layers, although their magnitude is not necessarily grown. The viscous sublayer, finally, remains constant throughout the range of rotation. This is contradiction to what was stated by Ricco and Hahn (2013), that a thin spinning boundary layer forms over the core of the discs. Perhaps the qualitative way in which these images can be analyzed so close to the wall is what is preventing this phenomenon to be fully analyzed. One may argue that the pictures above present a biased view of the phenomenon, and that they could be cherry picked to support the analysis. To counteract this sentiment, two point correlations have been performed at various wall-normal distances much like in the previous section. The results are presented in Figure 7.15 and 7.16 below. The first set of figures consists in the same two-point cross correlation algorithm described in Section 7.4, this time performed using values of out-of-plane vorticity  $\omega_z$ .

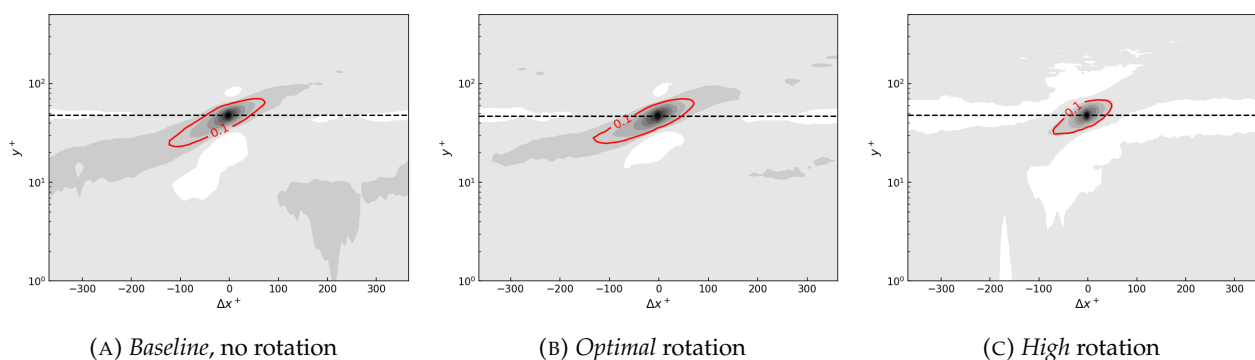


FIGURE 7.15: Two-point cross correlation map for  $\omega_z$  calculated at  $y^+ = 50$  and  $Re_\theta = 1966$ .

Here in the inclination of the correlation contours we can see the characteristic  $45^\circ$  angle at which vortical structures are inclined in turbulent boundary layers, as described by Adrian (2007) and many others. In the undisturbed state the coherence of these structures extends deep into the boundary layer and to wall-normal heights over  $100y^+$ , as emphasized by the dark grey patch in sub-figure 7.15a. As the discs rotate the coherence in the structures decreases, with the inclined grey patch now stopping much further away from the wall. This phenomenon culminates in sub-figure 7.15c depicting the correlations for the High rotation case, where the coherence has almost completely disappeared. The characteristic angle is still present, but the 0.1 threshold has shrunk greatly compared to the previous cases. These figures support the hypothesis presented in the previous section, that the disc rotation inhibits the formation and propagation of vortical structures present in a turbulent boundary layer.

Considering that this analysis deals with data acquired at one single wall-normal location, it is interesting to repeat the process from previous sections and plot the 0.1 threshold contours for the four wall-normal locations considered so far in this work. The results are as follows in Figure 7.16. A broader understanding can be gained from Figure 7.16 than when analyzing a single wall-normal location. As the disc rotation increases the coherence of the structures at  $y^+ = 25$  becomes less and less pronounced, until becoming as uncorrelated as the structures found in the logarithmic layer. The contour at  $y^+ = 50$  does not seem to change much between the Baseline and Optimal case, while it decreases strongly at the High case. This is expected and is known to be due to the single

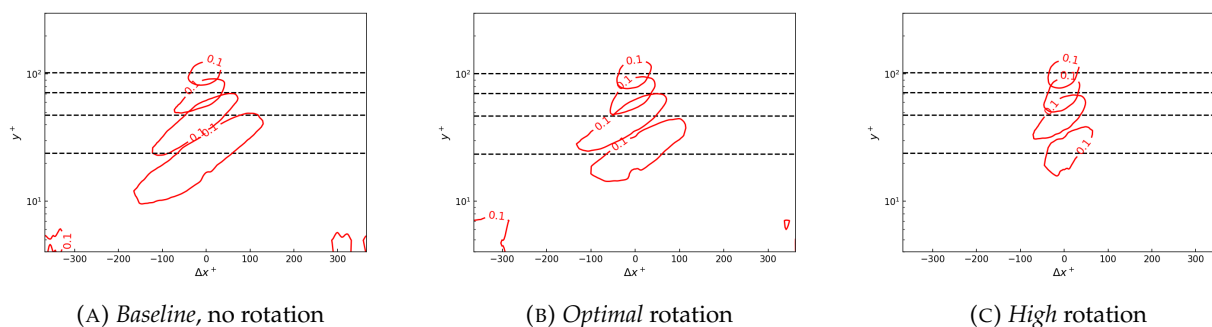


FIGURE 7.16: Two-point cross correlation contours of  $\omega_z$  with a threshold value of 0.1. Contours at  $y^+ = 25, 50, 70, 100$ .

contour considered which does not include the areas of slightly less correlation which can show bigger changes (for example, see the difference in contours and threshold between Fig. 7.15a and 7.15b above). Above this, the other two wall-normal locations' contours do not present significant changes between the three rotation cases, especially considering the one at  $y^+ = 100$ . What these contours can emphasize is that the out-of-plane vorticity is reduced in coherence from  $y^+ = 25$  up until the logarithmic layer, by the rotation of the discs. Outside the inner layers it therefore appears that the discs play a pivotal role at reducing both the velocity fluctuations and vortical events for both rotation velocities.

Once again, the reader must be warned on the closing of this section that these measurements were acquired only over the centerline of a disc, and that no spanwise development was measured. Furthermore, by using the values over the entire disc surface the streamwise development of disc effects is inherently smoothed out.

We have explored till now how the rotation of the discs influences the flowfield directly above the centerline. In summary, near the wall, different rotation velocities result in different behaviours. The Optimal case decreases the local skin friction significantly while the High case presents an increase, speculated to be due to the high values of wall-ward velocity present for this rotation. Away from the wall, however, velocity fluctuations and vortical turbulence events that occur in a normal boundary layer are decreased in frequency and magnitude for both rotation regimes up to a height of  $y^+ = 70$ . Two-point correlation contours show that the effect of the disc rotation is to decrease  $Q_2$  and  $Q_4$  events between  $y^+ = 25$  and  $y^+ = 100$  regardless of the disc rotation velocity. Furthermore, similar contours for out-of-plane vorticity quantitatively display a reduced coherence in characteristic vortical structures. Comparison of this with the mean quantities presented in the first section of this Chapter also provides an explanation for the shift up of the velocity profile and the thickening of the buffer layer. These mean behaviours have all been noted in prior studies to be a consequence of drag reduction effectiveness (for a review, consult Ricco et al. (2021)).

A qualitative analysis of several instantaneous fields revealed that as the disc rotation is increased the incidence of hairpin heads greatly decreases, as well as the vortical signatures indicating sweeps and ejections from the near wall region. Meanwhile, the vorticity signatures in the wake layer increase in prevalence as the disc rotation increases. These were described by Eitel-Amor et al. (2014) to accelerate the decay of turbulent coherent structures closer to the wall. Clearly these different events are linked, and point towards the fact that along the centerline of the rotating disc coherent structures are greatly diminished.

With this in mind we can now perform an analysis on the datasets acquired at a wall-parallel location in the logarithmic layer. They will shed light on the behaviour of the rotating disc array as a

whole, including the spanwise development of various flow features.

## 7.6 Over-Array Structure Behaviour

Using wall-parallel data it is possible to describe the mean flow dynamics over the entire array and ideally arrive at a general description of the flow phenomena involved in the skin-friction changes described in previous sections.

Firstly, to determine the wall-normal location of the plane a posteriori we can make use of any of the datasets without rotation. Considering  $Re_\theta = 1966$  and taking the spatial and temporal mean of both the fields of view returns a velocity of 2.34 [m/s], corresponding to a  $u^+$  of 15.4 [m/s]. Using the plots presented in Figure 7.1 we can deduce a wall normal distance of  $y^+ = 69$ , well within the logarithmic region. Of course, due to experimental manufacturing consideration, as well as the practical complexity in aligning the laser sheet parallel to the disc array, the actual mean velocity presents a slight change in the streamwise direction. This is less than 1% however, with the upper and lower bounds of  $y^+$  found at 65 and 78, and shown in Figure 7.17 below.

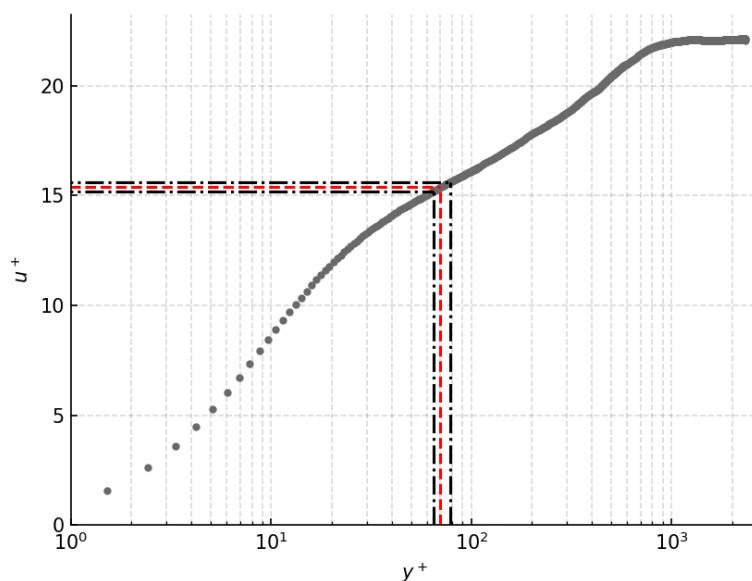


FIGURE 7.17: Location of wall parallel imaging plane. The red line is the mean velocity over the fields of view, and black dash-dotted lines are the upper and lower bounds of velocities found within the FOV.

To start off the analysis of wall-parallel data, the mean velocity over the array can then be plotted in Figure 7.18 below. The velocity shown is the normalized local velocity with the mean subtracted, resulting in contours around 0 for the all cases. The dimensions are scaled by the disc diameter  $D_0$ , and the coordinate system is centered around the center disc's leading edge, as described in Section 5.2.

The first noticeable feature is that as the RPM of the discs increases, high- and low-momentum pathways start forming over and between the discs. These are consistent regions where the streamwise mean velocity is significantly higher and lower than the global mean, respectively. These high- and low-momentum pathways are typically found in wall-bounded flows over surfaces with significant

spanwise variation of friction velocity, such as the ones found in Barros and Christensen (2014) and Bai et al. (2018). Already noticeable for the Optimal RPM, high velocity and high momentum flow starts passing over the discs, something that is rendered even more clear at the High RPM setting, where a noticeable “bump” in velocity is present over the disc’s leading edge. Meanwhile, in the spacing between the discs, low momentum flow accumulates. These regions display velocities well below the mean, speculated by Wise et al. (2014) to be induced by a viscous layer created by the radial flow due to the von Karman pumping effect over the stationary wall.

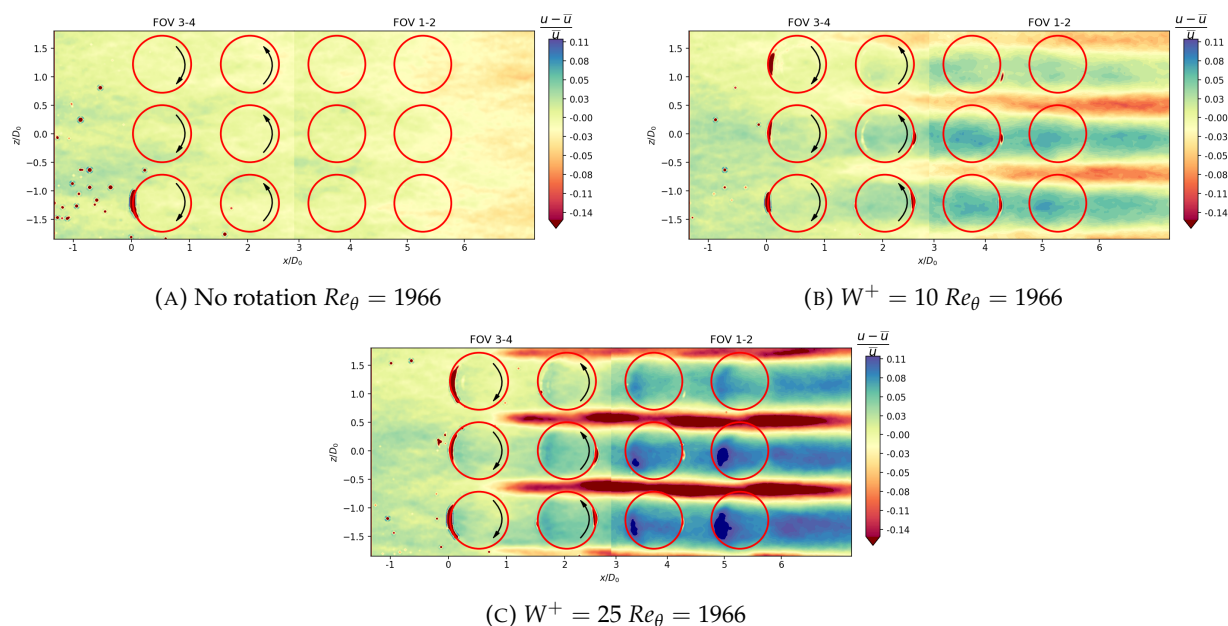


FIGURE 7.18: Normalized mean velocity for different RPMs at  $Re_\theta = 1966$ . Discs locations are highlighted in red, with their direction of rotation marked by the arrow.

Given this evolution of the flow’s momentum, it is interesting to extract wall-normal vorticity and see whether structures such as those described in Ricco and Hahn (2013) affect this momentum modulation throughout the array. The wall-normal vorticity  $\omega_y$  has been normalized with the disc diameter and the mean flow velocity over the array at plane height.

The first picture presents a quasi-isotropic vorticity distribution, with no clear outliers across both the fields of view. As the discs start to rotate at the optimum velocity the flow starts to evolve, with elongated structures developing downstream from the second disc onwards. The blue structures are oriented into the page, while the red ones towards the outside. As the RPM is increased the magnitude of these structures grows more and more, reaching the ones seen in Figure 7.19c. Here the vorticity in the “arms” of the structures is extremely high, and interesting patterns can be seen in the regions where the discs are closest to each other.

Recall how Ricco and Hahn (2013) and Olivucci et al. (2019) depict the inter-disc structures as iso-surfaces of disc-induced velocity. These structures are angled away from the wall, and contribute negatively to the drag reduction. At first sight, the vorticity contours presented in Figure 7.19 could represent the structures described by Ricco, but the latter have nothing to do with differential quantities. The question remains whether the vorticity signatures are related to Ricco’s inter-disc structures, but if that was the case one could speculate that the diminished drag reduction at high rotations is due to the increasingly negative effect that these structures have on the flow. It is however interesting to note how the shear created between these positive and negative vortical structures might lead to the low-momentum areas found between the discs in Figure 7.18. Furthermore,

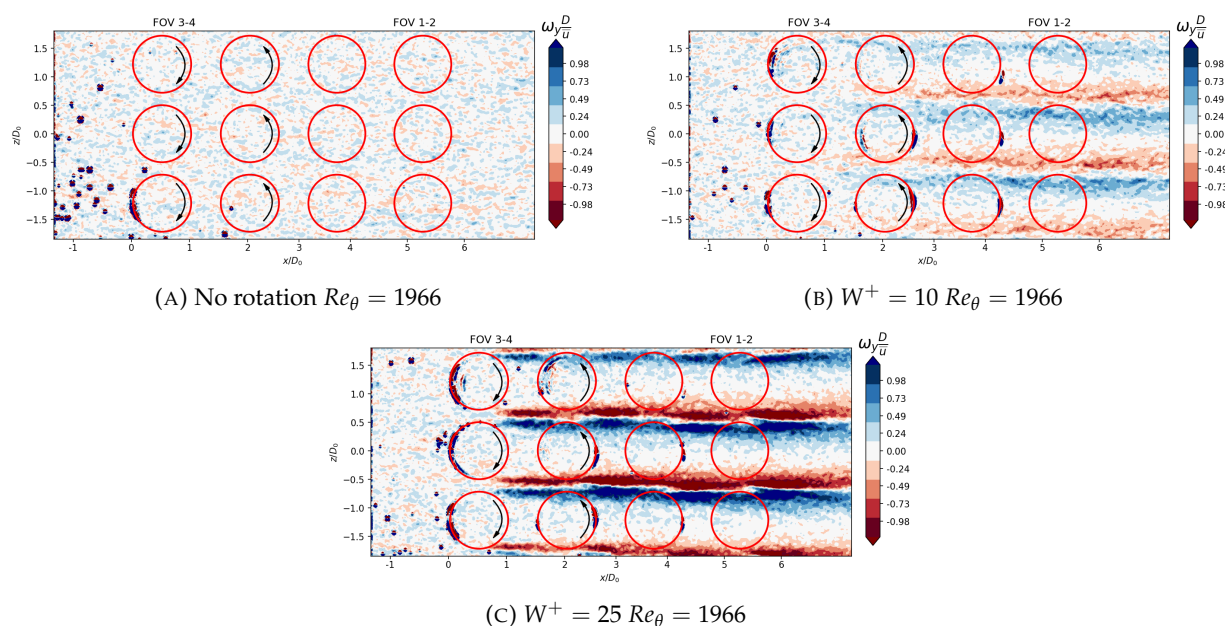


FIGURE 7.19: In plane normalized vorticity contours for three different RPMs at  $Re_\theta = 1966$ . Discs locations are highlighted in red, and the black dots to the left of the image are poor quality data-points far into the test section.

it has been shown before that boundary-condition-altering motions such as wall oscillations do not effectively change the global organization of the flow (Di Cicca et al., 2002). This differs from the findings presented here, with the figures above highlighting an interesting view on the difference between temporal and spatial oscillations. Recall that the former are oscillations of the flow in time (if the flow was standing still it would follow an oscillatory motion) and the latter are oscillations in space. These findings suggest that spatial oscillations are introducing an extra shear component that is significantly changing the flow features.

Finally, one of the quantities that can be extracted from this dataset is the streamwise Reynolds stress component  $R_{xx}$ . This has been normalized with the friction velocity extracted from the baseline case, and presents perhaps the most interesting phenomena in this section.

As with the other two figures, the Baseline case presents a mostly uniform distribution of Reynolds stress. As the RPM increases a pattern begins to emerge, one much different than the ones seen so far. Looking at sub-figure 7.20c, patches of high stresses appear between the discs, while a mostly uniform distribution of low stress is present over the discs. Furthermore, the high  $R_{xx}$  at the disc edges is not symmetrical in the streamwise direction; instead, these patches appear only at the disc edge where the local velocity vector is oriented in the same way as the flow. Further support to this claim is lent by the very edges of the imaged field of view, where darker patches clearly appear only at alternate discs, and where there is no disc on the other side. The low stress channels over the discs, on the other hand, directly support the claim from Wise et al. (2014) that the radial flow induced between the streamwise extent of the discs is beneficial for drag reduction, and that to maximize efficiency in the array consequent “columns” of discs have to be spaced around  $1.5D_0$  apart. It appears then that it would be ideal if the shearing action between the discs spanwise interaction would be kept to a minimum, reducing all the unpleasant effects that take place between disc rows.

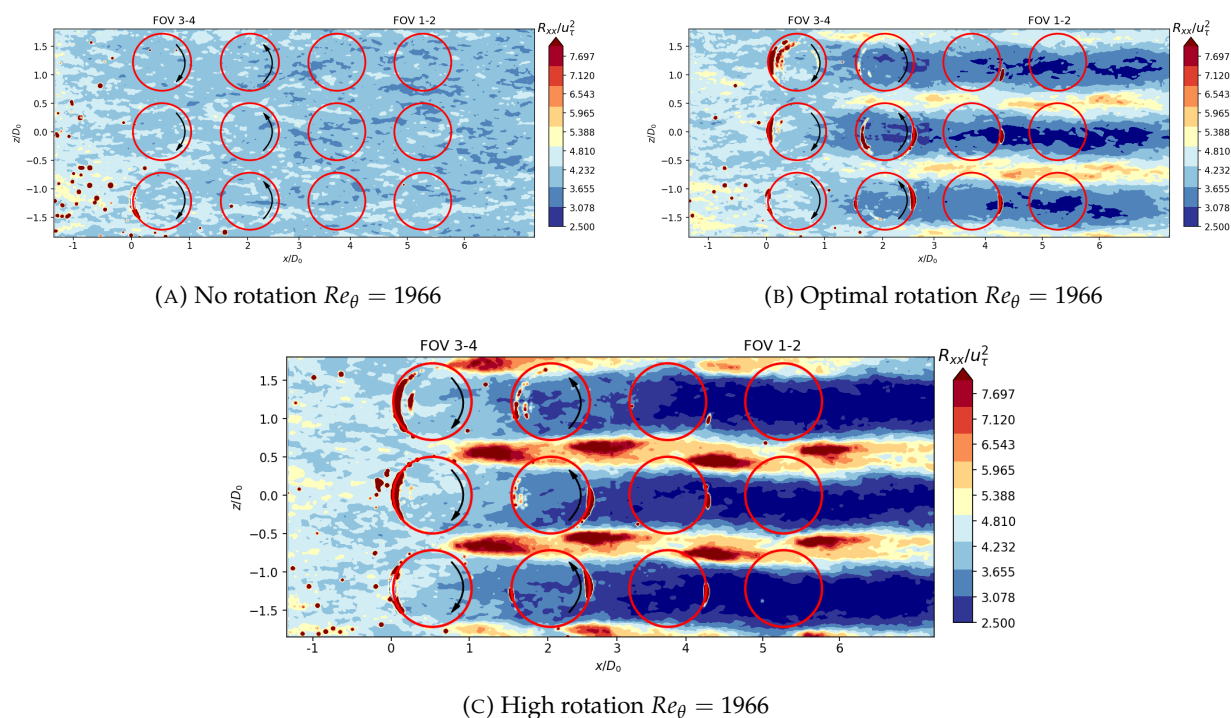
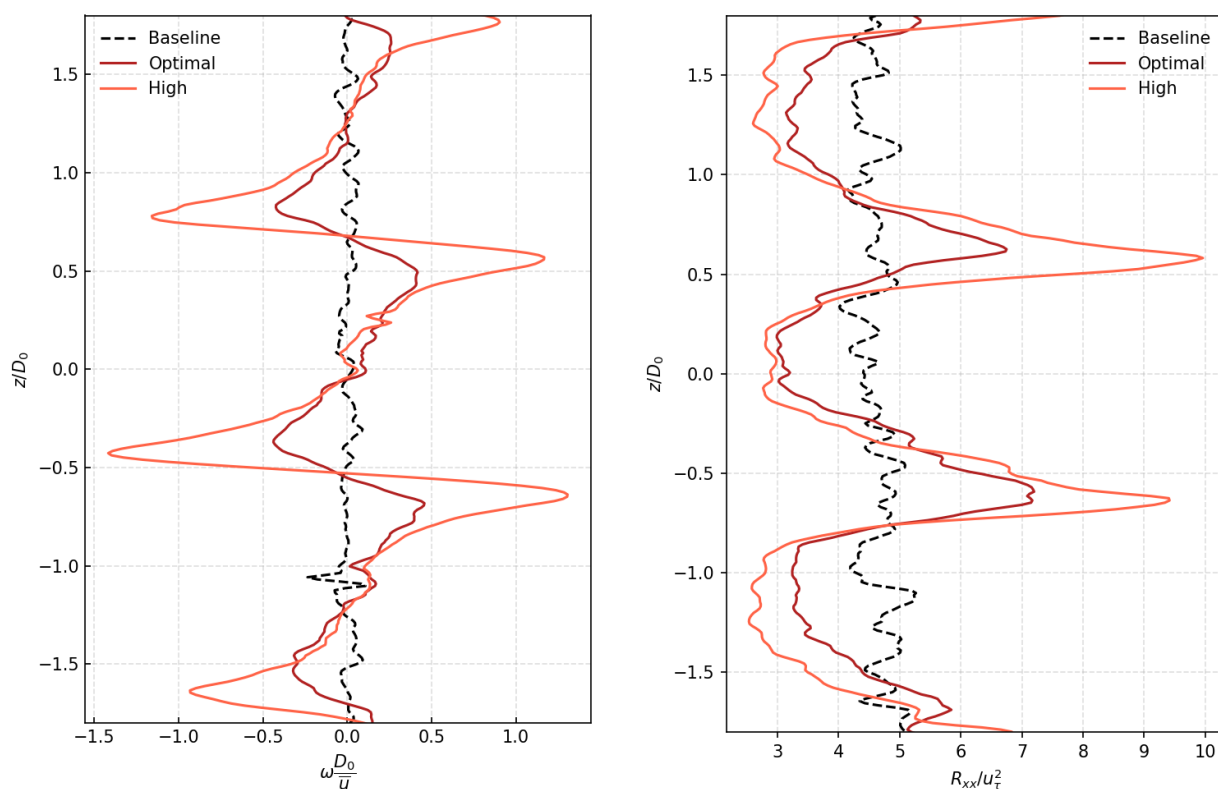


FIGURE 7.20: In plane normalized streamwise Reynolds stresses contours for three different RPMs at  $Re_\theta = 1966$ . Discs locations are highlighted in red.

To numerically quantify the effect of the Reynolds stresses and vorticity spanwise development, a spatial mean over the wall between the last two disc columns has been taken and plotted in Figures 7.21a and 7.21b below.

Focusing on the vorticity plot, a very similar pattern to what was intuitively extracted from Figure 7.19 can be found. The High case presents very sharp peaks of both positive- and negative-signed vorticity, with the Optimal case oscillating much more gently around 0 and the Baseline case having effectively no vorticity present in the domain. The right hand side figure however presents something that is not intuitively gathered from the contours presented previously. Over the discs ( $-1.5 < z/D_0 < -1.0$ ,  $-0.5 < z/D_0 < 0.5$  and  $1.0 < z/D_0 < 1.5$ ) the normalized Reynolds stresses are relatively similar between the Optimal and High case reaching a value of  $\sim 3$ . However, in the channels between the discs the value of the stresses for the High case is much higher than for the Optimal, exceeding 9 for the former versus a maximum of 7 for the latter. In other words, while the rotation benefits (in terms of Reynolds stresses) are somewhat equal regardless of rotation velocity, the downsides of the rotation are disproportionally worse at higher RPM regimes.

The wall parallel datasets can offer another interesting insight on the overall array dynamics. Assuming that there is an outer layer similarity at all spanwise locations in the plane, one would be able to use the friction velocity determined at the wall in Section 7.2 to extrapolate the entire array's friction velocity, point by point. The idea of outer layer similarity was first proposed by Townsend (1951) and further assessed in more recent times by Schultz and Flack (2005) and Chung et al. (2014). Essentially, it states that in a rough-wall turbulent boundary layer the outer layers of wall turbulence remain largely independent of the viscous sublayer. First and second order statistics collapse from the buffer region upward, with higher order statistics being only slightly more dependent on the boundary conditions. There is overwhelming experimental evidence that a defect law expressed as  $(u_\infty - \bar{u})/u_\tau = f(y/\delta)$  is universal in all boundary layers (Krogstad and Antonia, 1999). Within



(A) Spanwise normalized  $\omega_y$  distribution, mean from  $x/D_0 = 4$  to  $x/D_0 = 5$ .  
 (B) Spanwise normalized  $R_{xx}$  distribution, mean from  $x/D_0 = 4$  to  $x/D_0 = 5$

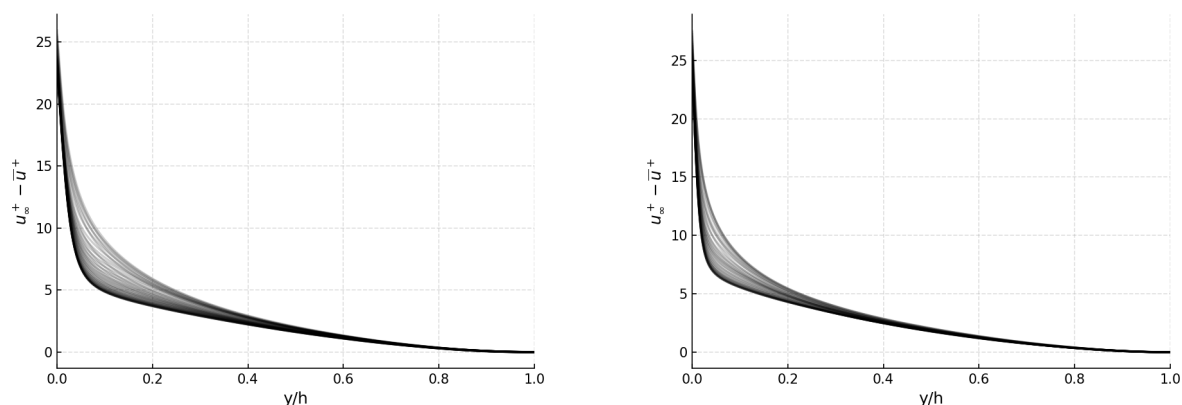
this work, this implies that knowing the velocity defect and the friction velocity at one point would allow the extrapolation of the friction velocities at all other points of the disc array.

The question remains as to whether the outer layer similarity in this experiment is present and verifiable. Thankfully another MSc. thesis (Levoni and Modesti, 2021) can be used to provide DNS data at various spanwise locations over the disc to verify this. Their disc array was slightly different, without spanwise or streamwise spacing, but by using only a single disc for the analysis an assumption can be made regarding the similarity between study cases. By measuring the velocity defect at each spanwise location and normalizing by the local (spanwise) friction velocity, one can verify whether the resulting profiles collapse in the logarithmic layer. The velocity defect is calculated in channel flow by subtracting the local streamwise mean velocity from the velocity at half-channel height. Since this work concerns itself with the turbulent boundary layer, the freestream velocity will be used instead. Quantitatively, this is expressed as follows

$$u_d\left(\frac{y}{\delta}\right) = \frac{(u_\infty - \bar{u})}{u_\tau} \quad (7.7)$$

Applying the expression above to the DNS data results in Figure 7.22, presented below.

The comparison between two friction Reynolds numbers is provided to show that, despite a good collapse not being achieved at medium Reynolds numbers, the increasing scale separation improves the collapse in the logarithmic layer. It stands to reason that at higher Reynolds number a full collapse would be achieved and that the influence of the Reynolds number decreases at higher values of  $Re_\tau$ .



(A) Velocity defect for a friction Reynolds number of 550    (B) Velocity defect for a friction Reynolds number of 1000

FIGURE 7.22: Velocity defect for DNS solutions of a channel flow at  $Re_\tau = 550$  and  $Re_\tau = 1000$ . Note how the “fan” between  $y/h = 0.05$  and  $y/h = 0.4$  becomes more cohesive as the Reynolds number increases.

With the assumption of outer layer similarity we can then use plots such as 7.18b or 7.18c to determine the local friction velocity at each spanwise location of the array, as well as the overall performance of it. Indeed, it has now become clear that the data to determine the skin-friction reduction had been collected at a very favorable location, not representative of the entire array.

Figure 7.23 below highlights this phenomenon. Here the curved lines represent the values of normalized mean velocity at the location where the skin-friction measurements took place, over FOV-4, and they quantify the pattern previously seen in Figure 7.18. The horizontal lines are mean normalized velocity over the array, representing the “performance” of the entire array as a velocity deficit from the dashed black line. From this it’s already evident that both the Optimal and High RPM increase the mean normalized velocity by approximately 3% when compared to baseline. The location at which the measurements took place is highlighted by the colored dots and the difference of these from the overall mean is marked by the arrow. It is therefore possible, with a few assumptions, to identify that the measured disc performance is 5-10% better than the overall array performance, depending on disc rotation. This is however at a wall normal height where both Optimal and High rotation regimes have been shown to significantly “improve” the behaviour of the flowfield, so it is complicated to make a direct connection to the behaviour displayed near the wall.

## 7.7 Discussion

The previous sections reported the findings of an experimental test campaign with the goal to investigate the interaction between flush-mounted rotating discs and a turbulent boundary layer. The relevance of this experiment is especially clear in the context of a push for environmental friendliness of air- and water-borne transport. With the planar PIV data captured for this experimental campaign it was possible to attempt to dissect the flow features characterizing the rotating disc array. Capturing high quality PIV data allowed the quantification of the velocity, vorticity and Reynolds stresses among others. These have been used to describe the discs’ effect on the local flowfield.

The characterization of the boundary showed that it is indeed canonical, representing turbulent boundary layers from literature and direct numerical simulations accurately below the wake region.

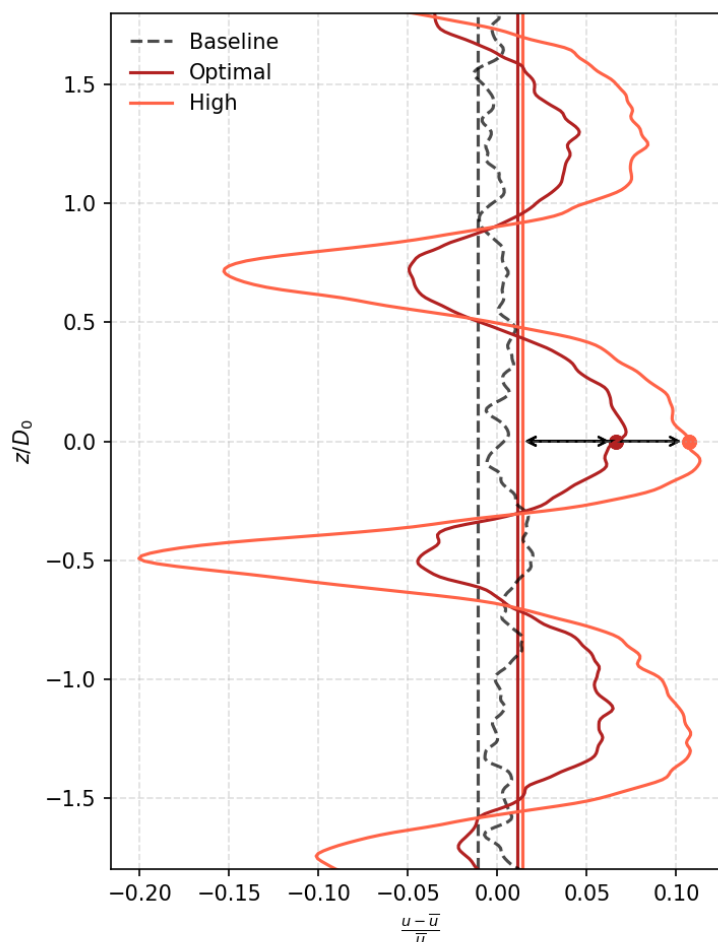


FIGURE 7.23: Mean normalized spanwise velocity over the streamwise extent of FOV-4 (curved lines) compared to measurement location (dots). The horizontal lines represent the mean velocity over the entire array.

This initial validation allowed to gather a sample friction velocity for the stationary wall, something used throughout the rest of the work to validate individual datasets.

After providing voltage to rotate the discs, it was measured how the disc rotation has a significant effect on the local skin-friction coefficient throughout the disc. Imaging over the last center disc showed that the Optimal RPM provides significantly lower skin-friction throughout the streamwise extent of the disc, as well as lower peaks in streamwise Reynolds stresses and turbulent kinetic energy production. This was attributed to a reduction in the velocity fluctuations near the wall, fluctuations that decrease for both the Optimal and High case up to  $y^+ = 70$ . Two-point cross correlation contours of  $u'$  showed that the rotation greatly hinders the penetration of these fluctuations in the near wall region, offering a hypothesis for the drag reduction mechanism. Further analysis on the instantaneous fields revealed that vortical structures within the boundary layer essentially disappear when the disc rotates, with two-point cross correlation contours highlighting how this effect propagates up to  $y^+ = 100$ . This analysis highlighted how the effect of the rotating discs is not confined at the wall, but can be felt up until the logarithmic layer. Furthermore, an increase in wake-layer background vorticity highlighted how the decay of turbulent structures closer to the wall is accelerated, in accordance with Eitel-Amor et al. (2014). With these results we

can hypothesize that the discs' rotation inhibits both the velocity fluctuations always present in a turbulent boundary layer and the vortical coherent structures so often defined in literature. It has been shown how increasing the disc rotation further decreases the incidence of these structures, almost removing them completely. This is fully in agreement with Ricco and Hahn (2013), where structures over the center of the discs were reduced in intensity compared to the ones travelling over stationary-wall regions.

It now appears clear that the major skin-friction drag changes, especially between the Optimal and High case, are taking place primarily in the regions closest to the wall. At the higher wall-normal locations, at which most of the statistical analysis took place, the Optimal and High case are very similar in behaviour. Even when looking back at the very first results, one can clearly notice how after  $y^+ = 20$  both the Optimal and High profile are fuller than the Baseline, representing higher momentum in the flow (Choi et al., 1998). The buffer layer is also demonstrably fuller when the data is plotted on a logarithmic x-axis, another characteristic of drag reducing flows (Ricco et al., 2021).

Perhaps some of the most striking findings came from the wall-parallel datasets captured at  $y^+ = 70$ . The spanwise spacing between the discs turned out to be a key area of interest, with interesting flowfield features developing over it. For example, the alternation of low and high momentum pathways suggests that there are significant three-dimensional effects at play within this mechanism, with the low speed areas suggested to be the drivers of drag increase. Analysis of the wall-normal vorticity ( $\omega_y$ ) revealed that between the discs there are two counter-rotating regions of shear, where the vorticity swings from positive to negative halfway through the spacing. These regions form immediately after the first disc, with the negative-signed vorticity coming from where the flow and the disc edge velocities have opposite signs. An analysis of the streamwise Reynolds stresses in this plane revealed that "patches" of very high stress exist at the disc edge where the local edge velocity and the disc velocity have the same sign, and that these patches severely increase in magnitude as the rotation velocity of the discs increases.

Based on these findings and on a review of the literature it is therefore possible to propose the existence of two different types of flow phenomena within this rotating discs study case, much akin to what was described by Wise and Ricco (2014). The first, happening over the centerline of the discs, is similar to a fully oscillating wall. The oscillation takes place in the spatial domain, unlike the fully oscillating wall where the oscillation is defined temporally. This spatial oscillation works like described in the literature reviewed in Chapter 3, with the movement of the discs inhibiting the low-speed streaks, hairpin packets and other drivers of turbulence. This is done mainly by shifting these coherent structures side-to-side and impeding their regeneration (Hamilton et al., 1995; Ricco, 2004). Between the discs, the second type of flow occurs. This is almost fully sheared flow, driven by the interaction between the disc edges themselves and between the edges and the surrounding flowfield. The shear created by the opposite velocity vectors of the disc edges greatly increases the stresses over the stationary wall, leading to a local drag increase. For this reason the spanwise spacing between the discs should be kept to a minimum, in accordance with results from Wise et al. (2014). By minimizing the surface area where the shearing effect takes place, any industrial application of this method would be able to maximize the drag reduction offered by it. While there will always be some sheared flow due to the simple physics of the discs' edges moving in opposite directions, minimizing the area between them is paramount for efficiency purposes.

Noting how alternating columns of discs can be "flipped" vertically to achieve a symmetrical pattern for the streamwise Reynolds stresses, one can generalize the two flows described above with a single schematic, hereby presented in Figure 7.24 below. The center portion contained between the dashed lines depicts the oscillating flow-like behaviour, while the arrows on the edges and the spacing between the discs represents the shearing action of the discs.

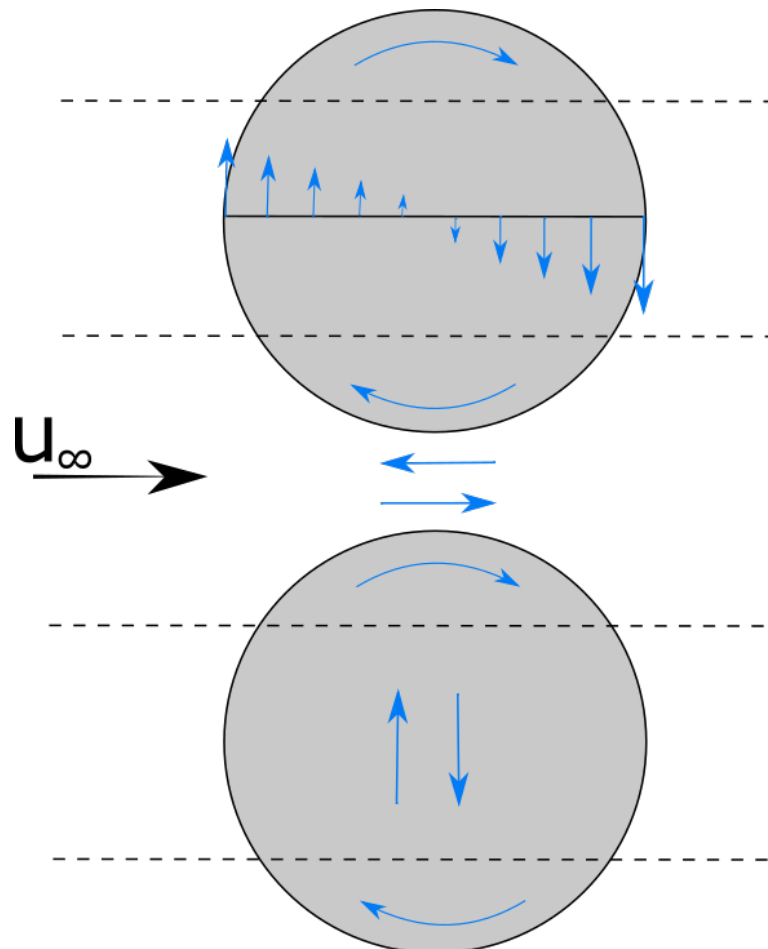


FIGURE 7.24: Schematic aiming to illustrate the different types of flow phenomena present in a disc array. Over the discs the flow behaves like in an oscillating wall, while between the discs the flow is strongly sheared.

## Chapter 8

# Conclusion and Recommendations

This chapter will cover the overall conclusions of the thesis, followed by recommendations for future research in this field.

### 8.1 Conclusions

The research performed was aimed at investigating the flowfield effects of flush-mounted rotating discs on a turbulent boundary layer. Skin-friction drag contributes to a large share of overall fuel expenditure in air- and water-borne transport, and as such any reductions in drag can result in monumental monetary and environmental benefits.

To begin this work, a thorough research into the relevant literature was performed. The turbulent boundary layer fundamentals were explored, paying special attention to the scaling parameters of such flows and the turbulent structures and characteristics found with them. Following, a general overview of existing skin-friction drag reducing methods was presented. Here, special attention was paid to the oscillating wall, a well established technique that has managed to show drag savings a plurality of times in laboratory settings. Noting the similarities between this technique and the rotating discs, a thorough investigation was performed on literature discussing the latter, chiefly the few numerical studies performed so far.

After a review of literature, a setup was designed and manufactured to allow for the testing in TU Delft's windtunnel laboratories. This setup was designed to house a  $4 \times 3$  array of discs, with each streamwise row rotating in the opposite direction as the previous. Using performance parameters from literature, the discs were sized with a diameter of 0.055 [m], a streamwise spacing of 0.083 [m] and a spanwise spacing of 0.066 [m]. The rotational velocity of the discs was changed throughout the testing campaign and was in a range between 550 and 1500 RPM. To achieve a fully turbulent boundary layer in a relatively short streamwise extent, the flow was aggressively tripped using distributed roughness elements.

The tests were performed in TU Delft's windtunnel laboratory. The windtunnel used, known as the W-Tunnel, is an open-jet open-return facility with an exit cross-sectional area of  $60 \times 60$ [cm]. The facility used was augmented with a transparent plexiglass test section, so that the flowfield could be imaged at high resolution through the sidewall.

Throughout the testing campaign planar PIV measurements were acquired at various locations over the disc array. The fourth center disc was imaged over its midspan, reaching vector resolutions down to 0.12 [mm] per vector. This allowed the determination of the friction velocity from the linear region. Furthermore, the entire disc array was imaged via a wall-parallel plane located at  $y^+ = 70$ .

An analysis of the near-wall behaviour using high resolution sCMOS cameras revealed that significant friction drag reductions occur near the wall. Looking at mean statistical quantities reveals that the Reynolds stresses as well as the turbulent kinetic energy production have a significant increase

in regions near the wall for High rotation regimes, while decreasing steadily for lower rotations. Further away from it the behaviour inverses, with higher rotations resulting in lower Reynolds stresses and TKE production. The mean velocity over the disc also showed this behaviour, with the linear region displaying behaviour characteristic of a friction drag increase for the High case while the buffer layer thickened for both, signifying skin-friction drag decreases in both rotation regimes. This flow behaviour was further explored by analyzing the turbulent velocity fluctuations at a selection of wall-normal locations over the disc. Quadrant decomposition revealed that the disc rotation inhibits velocity fluctuations from the lowest  $y^+$  analyzed to  $y^+ = 70$ . Two-point correlation contours were further employed to discuss the instantaneous field organization, showing that the out-of-page vorticity  $\omega_z$  decreases sharply throughout the range of wall-normal locations as the disc rotation velocity is increased. Knowing from literature how velocity fluctuations and vortical structures are a key in the production of turbulence, it was speculated this was the case for the greatly reduced Reynolds stresses and TKE production at a similar  $y^+$  range.

Analyzing the wall-parallel images acquired at  $y^+ = 70$  returned further compelling results. Mean velocity contours over the entire array showed a stark decrease in momentum at spanwise locations between the discs and an increase over the discs proper. The streamwise Reynolds stresses also showed interesting behaviour, with patches of stresses of magnitude more than double the baseline appearing at the disc-flow interface when the disc velocity vector points in the same direction as the flow. An analysis of these stresses showed that the detriment of the higher disc rotation outweighs the benefits displayed over the mid-span. Further analysis using DNS data from another study, as well as several assumptions, showed that the performance over the mid-disc's centerline overestimates the entire array's performance by about 10%. This allows for a gross estimation of the overall drag reduction at  $\approx 40\%$ .

Regarding the research questions, the main objective of this work has been answered, namely how the turbulent boundary layer above the discs is influenced by the rotation of the latter.

The sub-questions first presented in the introduction also have been answered to different extents. It has been shown how the discs' rotation affects the turbulent boundary layer and the coherent structures within it, as well as how different rotational velocities have different effects. Furthermore, the effects of the Reynolds number have been quantified in the mean quantities over the disc centerline. Regarding the overall array, interesting flowfield changes have been identified and analyzed in depth. The only question not thoroughly answered is on the Reynolds number effect on the disc scaling factors. For that, a larger parametric study would ideally be performed.

Despite providing an answer to the research question, there are still some doubts over the practicality of this method and its industrial readiness. First and foremost, in its current status, it is hard to see how this system could work in a fluid other than air. The gap between the disc and the surface inherently allows some flow inside it, requiring sub-millimeter precision in assembly to minimize this. In maritime applications the compartment containing the motors and/or belts to move the discs would be flooded instantly, without even accounting for the corrosions of the discs due to salinity and other problems. Even in aircraft, the complexity of installing and maintaining such a system is not to be overlooked, with possibly hundreds of motors or connecting mechanisms needed to be assembled and operated. It would not be possible to have a motor per disc, as the sheer weight of this would play against any possible drag savings. Any malfunction in the driving mechanism would then prevent several discs from working effectively, essentially becoming dead weight on the aircraft. As Ricco and Hahn (2013) state, the disc size scaled to Reynolds numbers present on aircraft approaches 1[mm], increasing the complexity of installing and maintaining such a system. Overall, even if the drag savings could be reliably and effectively established, it is hard to see how such a method would be considered "industrially ready".

## 8.2 Recommendations

Throughout the course of this thesis several additional questions have developed naturally from the intrinsic limitations of the setup or by features further revealed by the data analysis process. The foregoing highlights a few points of importance to consider when conducting a similar or expansionary testing campaign.

Related to the windtunnel facilities used, as well as the setup design, the chief recommendation is to improve the plate manufacturing. As extensively discussed in Sections 5.3.2 and 6.3.2, the discs were never exactly flush with the flat plate and this caused them to experience slightly different rotation velocities, as well as induced vertical velocities due to the disc-gap shear (see Figure 8.1 below).

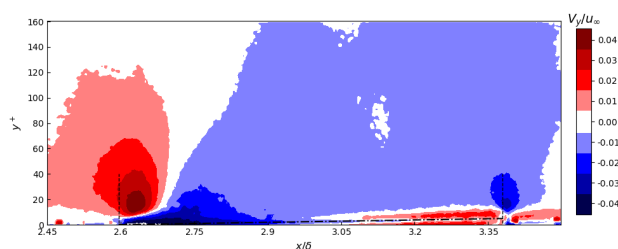


FIGURE 8.1: Wall-normal velocity contours over the fourth disc, measured at  $Re_\theta = 1966$  and  $W^+ = 25$ .

An obvious recommendation therefore is to improve the plate and disc manufacturing overall. This could be done via CNC methods or similar, but ideally the gap between the disc and the plate would be invariant along its circumference and kept to a minimum. The precise, computer controlled, location of the setting holes for the discs would moreover make sure that the discs are always at the center of the holes in the plate, ideally making the RPMs across the array more consistent.

Some recommendations can also be made about what and how to image the flowfield, be it for extra datasets or to augment the ones already presented. The first recommendations would be to employ tomographic PIV to shed further light on the vortical features. Much like in Kempaiah et al. (2020), tomographic PIV would allow the visualization of the weakening of the streamwise coherent vortices, something that is not directly observed in this work. Furthermore, the vortical structures oriented in and out of the plane visualized from wall-parallel data would be able to be mapped in three dimensions and their effect would be better quantified. If tomographic PIV could not be employed, imaging the flow at multiple wall-parallel planes would open the door to better visualization of the spanwise variation in velocity and vorticity. An experimental campaign aimed only at wall-parallel imaging of this setup could image planes much closer to the wall, ideally below  $y^+ = 20$ . Thirdly, for a full characterization of the impact a rotating disc makes on the flowfield, a clear recommendation would be to image the flow at least at three different spanwise locations over the array. This would allow the researcher to determine the turbulent boundary layer behaviour near the wall for one full disc. Further light would be shed on the friction velocity's spanwise development at the wall, something that would be key to understanding the overall potential of the rotating discs. Finally, it would be apt to measure the same datasets in large scale facilities or with higher resolution/smaller FOVs. This allows the imaging of higher quality data at higher Reynolds numbers, allowing a full investigation of the Reynolds number effects in this type of flowfield. Furthermore, this could push the boundaries of what DNS simulations can resolve and add more information to the body of knowledge.

---

As an overarching recommendation, the takeaway from this work should be to try to achieve similar fundamental effects on the flowfield but without the complexity of the disc array. We have seen the potential in terms of skin-friction drag reduction, and we have analyzed why these physical effects are taking place. Ideally more rounded technologies in passive flow control, or non-moving active techniques should aim at changing the flowfield in a similar way; this would reduce the practical influences of things like disc-wall gaps and uneven motor velocities.

## Appendix A

# Appendix A - Technical Drawings

This appendix presents the technical drawings on which the manufacturing of the parts of the test was based.

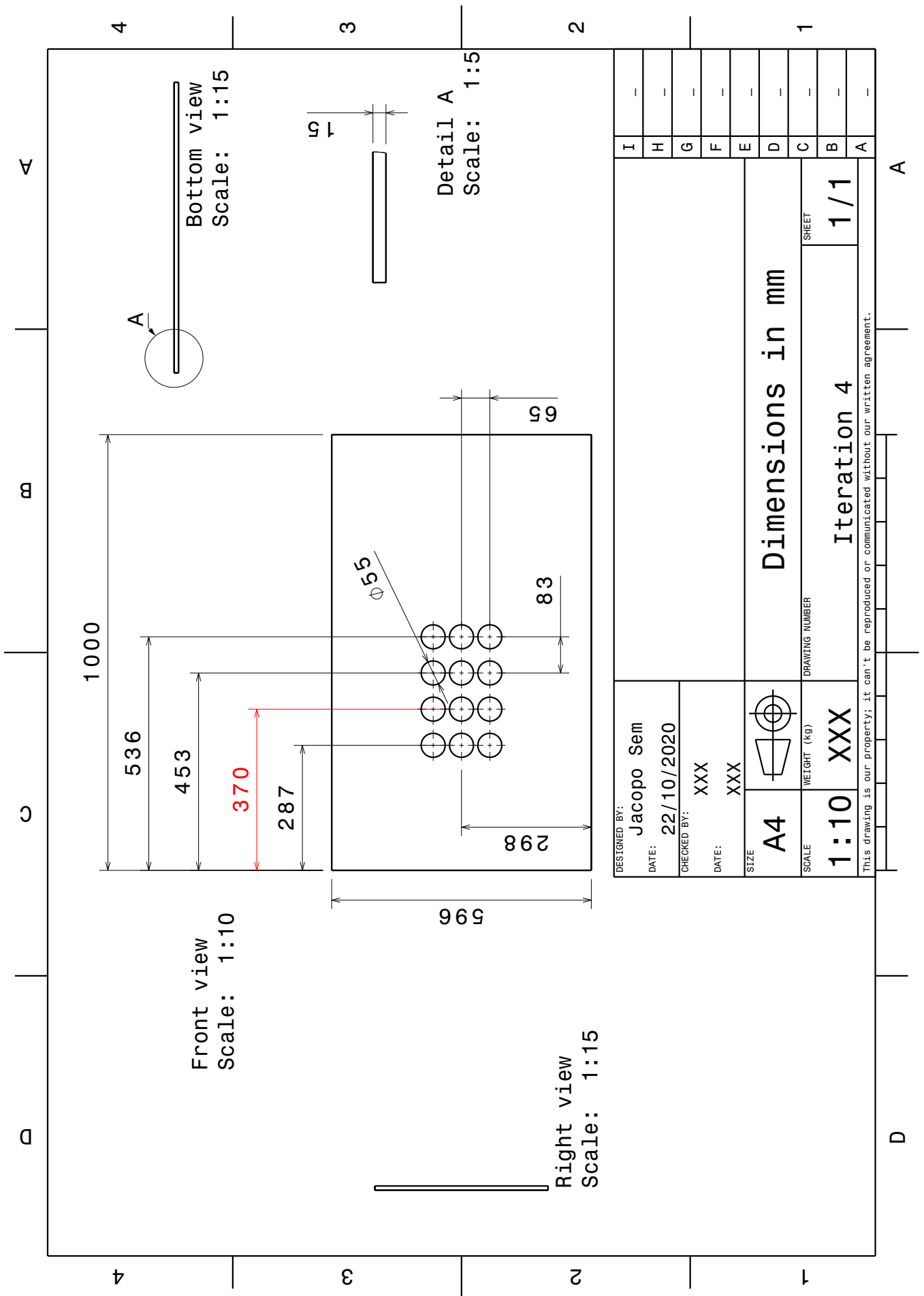


FIGURE A.1: The plate holding the disc array in the test section

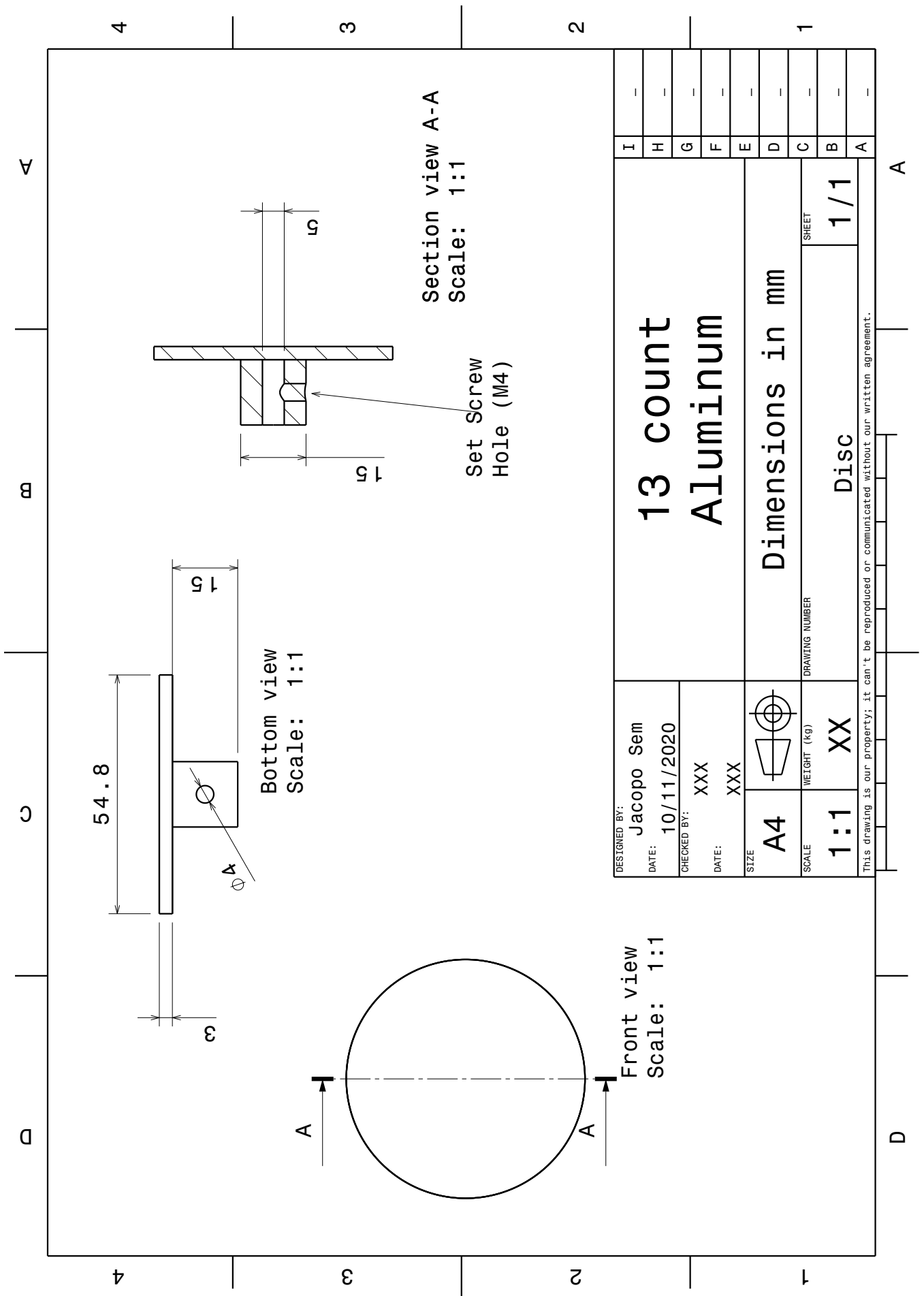


FIGURE A.2: The disc

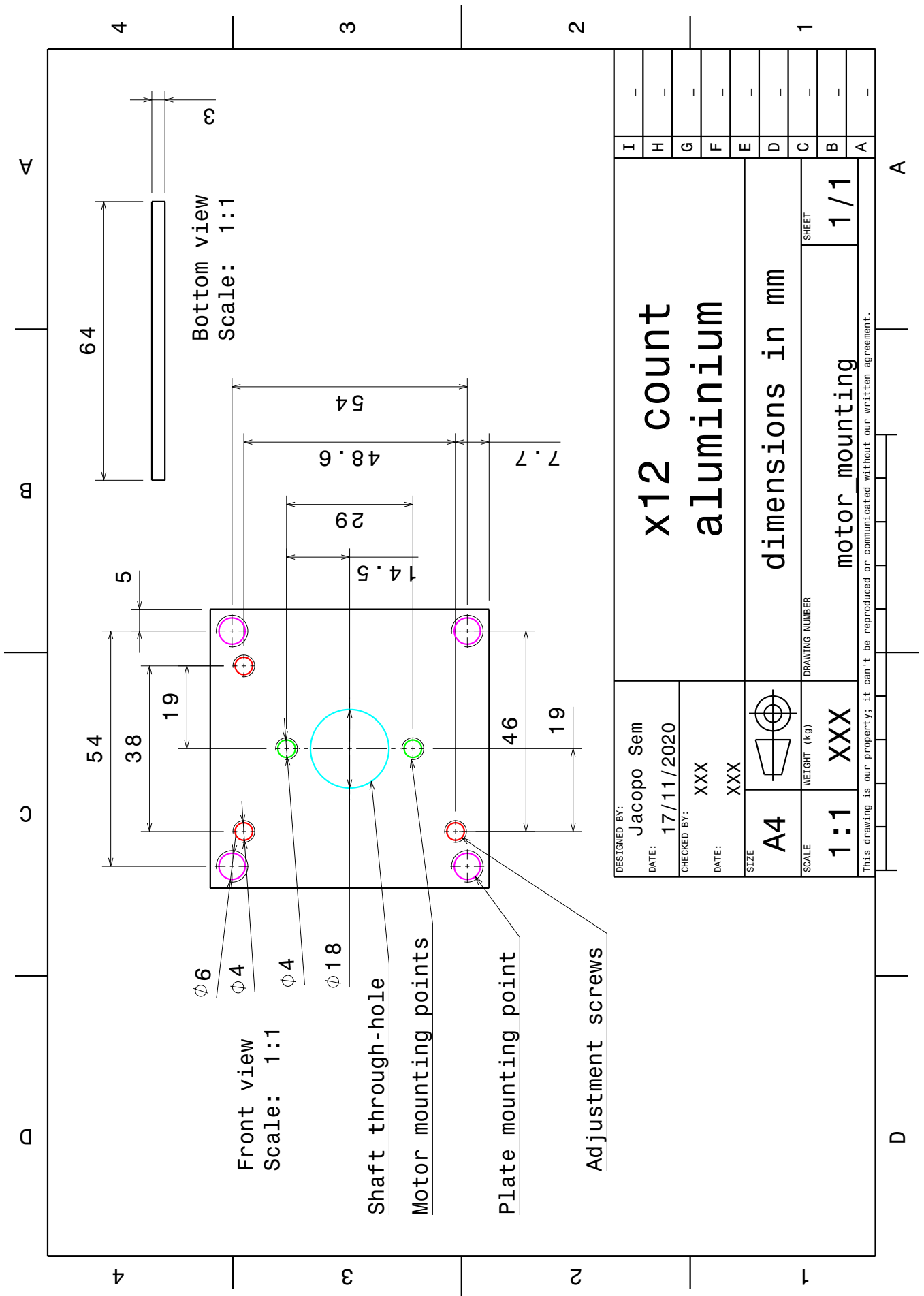


FIGURE A.3: The plate used to secure the discs flush with the plate in Fig. A.1

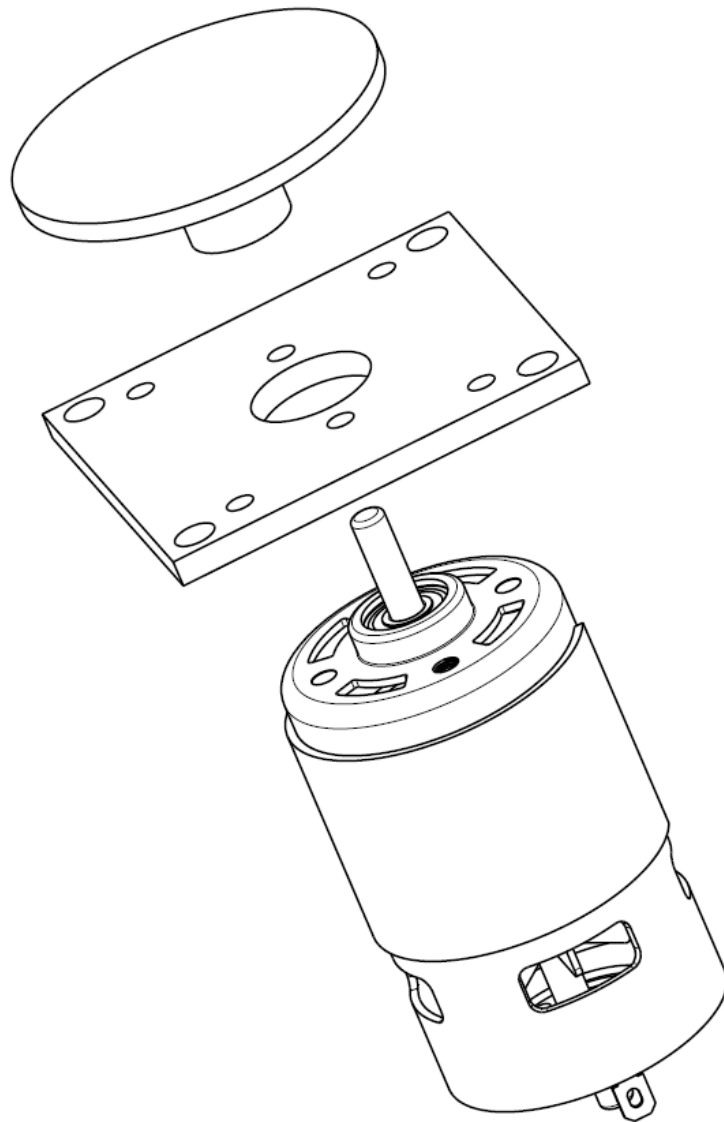


FIGURE A.4: Assembly of motor, mounting plate and disc.

## Appendix B

# Appendix B - Test Matrices

Velocity	Camera Config.	Disc RPM	Voltage	Images captured	Tunnel RPM
3	FOV-3 and FOV-4	0	0	500	610
		550	2.4	1000	610
		1400	5.2	1000	610
3	FOV-4 and FOV-A	0	0	500	610
		550	2.4	1000	610
		1400	5.2	1000	610
5	FOV-4 and FOV-A	0	0	500	970
		870	3.4	1000	970
		2170	7.5	1000	970
10	FOV-4 and FOV-A	0	0	500	1850
		1350	5.0	1000	1850
		3400	11.7	1000	1850

TABLE B.1: Test matrix for FOVs over the discs

Velocity	Disc RPM	Voltage	Images captured	Tunnel RPM
3	0	0	500	610
	550	2.4	500	610
	1400	5.2	500	610
5	0	0	500	970
	870	3.4	500	970
	2170	7.5	500	970
10	0	0	500	1850
	1350	5.0	500	1850
	3400	11.7	500	1850

TABLE B.2: Test matrix for wall parallel FOVs

<b>Velocity</b>	<b>Disc RPM</b>	<b>Voltage</b>	<b>Images captured</b>	<b>Tunnel RPM</b>
3	0	0	500	610
	550	2.4	500	610
5	0	0	500	970
	870	3.4	500	970
10	0	0	500	1850
	1350	5.0	500	1850

TABLE B.3: Test matrix for FOVs over the full array

# Bibliography

- [1] R. J. Adrian. "Hairpin vortex organization in wall turbulence". In: *Physics of Fluids* 19.4 (2007), p. 041301. DOI: [10.1063/1.2717527](https://doi.org/10.1063/1.2717527).
- [2] J. D. Anderson. *Fundamentals of Aerodynamics*. McGraw-Hill series in aeronautical and aerospace engineering. McGraw-Hill, 2010. ISBN: 9780070700123. URL: <https://books.google.nl/books?id=7B4GQ9G1jPMC>.
- [3] R. A. Antonia, Y. Zhu, and M. Sokolov. "Effect of Concentrated Wall Suction on a Turbulent Boundary-Layer". In: *Physics of Fluids* 7.10 (1995), pp. 2465–2474. ISSN: 1070-6631. DOI: [Doi10.1063/1.868690](https://doi.org/10.1063/1.868690).
- [4] H. L. Bai, Kevin, N. Hutchins, and J. P. Monty. "Turbulence modifications in a turbulent boundary layer over a rough wall with spanwise-alternating roughness strips". In: *Physics of Fluids* 30.5 (2018). ISSN: 1070-6631. DOI: [Artn05510510.1063/1.5026134](https://doi.org/10.1063/1.5026134).
- [5] H. L. Bai, Y. Zhou, W. G. Zhang, S. J. Xu, Y. Wang, and R. A. Antonia. "Active control of a turbulent boundary layer based on local surface perturbation". In: *Journal of Fluid Mechanics* 750 (2014), pp. 316–354. ISSN: 0022-1120. DOI: [10.1017/jfm.2014.261](https://doi.org/10.1017/jfm.2014.261).
- [6] A. Baron and M. Quadrio. "Turbulent drag reduction by spanwise wall oscillations". In: *Applied Scientific Research* 55.4 (1995), pp. 311–326. ISSN: 0003-6994.
- [7] J. M. Barros and K. T. Christensen. "Observations of turbulent secondary flows in a rough-wall boundary layer". In: *Journal of Fluid Mechanics* 748 (2014). ISSN: 0022-1120. DOI: [ARTNR110.1017/jfm.2014.218](https://doi.org/10.1017/jfm.2014.218).
- [8] C. Barthlott and F. Fiedler. "Turbulence structure in the wake region of a meteorological tower". In: *Boundary-Layer Meteorology* 108.1 (2003), pp. 175–190. ISSN: 0006-8314. DOI: [Doi10.1023/A:1023012820710](https://doi.org/10.1023/A:1023012820710).
- [9] L. H. Benedict and R. D. Gould. "Towards better uncertainty estimates for turbulence statistics". In: *Experiments in Fluids* 22.2 (1996), pp. 129–136. ISSN: 0723-4864. DOI: [DOI10.1007/s003480050030](https://doi.org/10.1007/s003480050030).
- [10] N. S. Berman. "Drag Reduction by Polymers". In: *Annual Review of Fluid Mechanics* 10.1 (1978), pp. 47–64. DOI: [10.1146/annurev.fl.10.010178.000403](https://doi.org/10.1146/annurev.fl.10.010178.000403).
- [11] H. C. Bilinsky. "Riblet Microfabrication Method for Drag Reduction". In: *55th AIAA Aerospace Sciences Meeting*. 2017. DOI: [10.2514/6.2017-0047](https://doi.org/10.2514/6.2017-0047).
- [12] R. F. Blackwelder and H. Eckelmann. "Streamwise vortices associated with the bursting phenomenon". In: *Journal of Fluid Mechanics* 94.3 (1979), pp. 577–594. DOI: [10.1017/S0022112079001191](https://doi.org/10.1017/S0022112079001191).
- [13] R. F. Blackwelder and L. S. Kovasznay. "Time Scales and Correlations in a Turbulent Boundary-Layer". In: *Physics of Fluids* 15.9 (1972), pp. 1545–+. ISSN: 1070-6631. DOI: [Doi10.1063/1.1694128](https://doi.org/10.1063/1.1694128).
- [14] P. Bradshaw and N. S. Pontikos. "Measurements in the Turbulent Boundary-Layer on an Infinite Swept Wing". In: *Journal of Fluid Mechanics* 159.Oct (1985), pp. 105–130. ISSN: 0022-1120. DOI: [Doi10.1017/S0022112085003123](https://doi.org/10.1017/S0022112085003123).

- [15] M. H. Buschmann and M. Gad-El-Hak. "Structure of the canonical turbulent wall-bounded flow". In: *AIAA Journal* 44.11 (2006), pp. 2500–2503. ISSN: 0001-1452. DOI: [10.2514/1.19172](https://doi.org/10.2514/1.19172).
- [16] L. N. Cattafesta and M. Sheplak. "Actuators for Active Flow Control". In: *Annual Review of Fluid Mechanics, Vol 43* 43 (2011), pp. 247–272. ISSN: 0066-4189. DOI: [10.1146/annurev-fluid-122109-160634](https://doi.org/10.1146/annurev-fluid-122109-160634).
- [17] K. A. Chauhan, P. A. Monkewitz, and H. M. Nagib. "Criteria for assessing experiments in zero pressure gradient boundary layers". In: *Fluid Dynamics Research* 41.2 (2009). ISSN: 0169-5983. DOI: [Artn02140410.1088/0169-5983/41/2/021404](https://doi.org/10.1088/0169-5983/41/2/021404).
- [18] H. Choi, P. Moin, and J. Kim. "Active Turbulence Control for Drag Reduction in Wall-Bounded Flows". In: *Journal of Fluid Mechanics* 262 (1994), pp. 75–110. ISSN: 0022-1120. DOI: [Doi10.1017/S0022112094000431](https://doi.org/10.1017/S0022112094000431).
- [19] K. S. Choi and B. R. Clayton. "The mechanism of turbulent drag reduction with wall oscillation". In: *International Journal of Heat and Fluid Flow* 22.1 (2001), pp. 1–9. ISSN: 0142-727x. DOI: [Doi10.1016/S0142-727x\(00\)00070-9](https://doi.org/10.1016/S0142-727x(00)00070-9).
- [20] K. S. Choi, DeBisschop Jr, and B. R. Clayton. "Turbulent boundary-layer control by means of spanwise wall oscillation". In: *AIAA Journal* 36.7 (1998), pp. 1157–1163. ISSN: 0001-1452. DOI: [Doi10.2514/2.526](https://doi.org/10.2514/2.526).
- [21] D. Chung, J. P. Monty, and A. Ooi. "An idealised assessment of Townsend's outer-layer similarity hypothesis for wall turbulence". In: *Journal of Fluid Mechanics* 742 (2014). ISSN: 0022-1120. DOI: [ARTNR310.1017/jfm.2014.17](https://doi.org/10.1017/jfm.2014.17).
- [22] E. R. Corino and Robert S. Brodkey. "A visual investigation of the wall region in turbulent flow". In: *Journal of Fluid Mechanics* 37.1 (1969), pp. 130. DOI: [10.1017/S0022112069000395](https://doi.org/10.1017/S0022112069000395).
- [23] T. C. Corke, C. L. Enloe, and S. P. Wilkinson. "Dielectric Barrier Discharge Plasma Actuators for Flow Control". In: *Annual Review of Fluid Mechanics* 42 (2010), pp. 505–529. ISSN: 0066-4189. DOI: [10.1146/annurev-fluid-121108-145550](https://doi.org/10.1146/annurev-fluid-121108-145550).
- [24] T. C. Corke, Y. Guezennec, and H. M. Nagib. "Modification in drag of turbulent boundary layers resulting from manipulation of large-scale structures". In: *Progress in Astronautics and Aeronautics* 72 (1980), pp. 128–143.
- [25] D. B. DeGraaff, D. R. Webster, and J. K. Eaton. "The effect of Reynolds number on boundary layer turbulence". In: *Experimental Thermal and Fluid Science* 18.4 (1998), pp. 341–346. ISSN: 0894-1777. DOI: [Doi10.1016/S0894-1777\(98\)10042-0](https://doi.org/10.1016/S0894-1777(98)10042-0).
- [26] G. M. Di Cicca, G. Iuso, P. G. Spazzini, and M. Onorato. "Particle image velocimetry investigation of a turbulent boundary layer manipulated by spanwise wall oscillations". In: *Journal of Fluid Mechanics* 467 (2002), pp. 41–56. ISSN: 0022-1120. DOI: [10.1017/S002211200200157x](https://doi.org/10.1017/S002211200200157x).
- [27] A. P. Dowling. "The effect of large-eddy breakup devices on oncoming vorticity". In: *Journal of Fluid Mechanics* 160 (1985), pp. 447–463. DOI: [10.1017/S002211208500355X](https://doi.org/10.1017/S002211208500355X).
- [28] D. M. Driver and S. K. Hebbar. "Experimental-Study of a 3-Dimensional, Shear-Driven, Turbulent Boundary-Layer". In: *AIAA Journal* 25.1 (1987), pp. 35–42. ISSN: 0001-1452. DOI: [Doi10.2514/3.9575](https://doi.org/10.2514/3.9575).
- [29] M. Duvelleroy, L. Benquet, S. Schaffrath, and M.A. Delestrade. *Airbus reveals new zero-emission concept aircraft*. Available at <https://www.airbus.com/newsroom/press-releases/en/2020/09/airbus-reveals-new-zeroemission-concept-aircraft.html>. 2020.
- [30] G. Eitel-Amor, O. Flores, and P. Schlatter. "Hairpin vortices in turbulent boundary layers". In: *1st Multiflow Summer Workshop* 506 (2014). ISSN: 1742-6588. DOI: [Artn01200810.1088/1742-6596/506/1/012008](https://doi.org/10.1088/1742-6596/506/1/012008).

- [31] O. A. El-Samni, H. H. Chun, and H. S. Yoon. "Drag reduction of turbulent flow over thin rectangular riblets". In: *International Journal of Engineering Science* 45.2-8 (2007), pp. 436–454. ISSN: 0020-7225. DOI: [10.1016/j.ijengsci.2007.03.002](https://doi.org/10.1016/j.ijengsci.2007.03.002).
- [32] R. E. Falco. "Coherent motions in the outer region of turbulent boundary layers". In: *The Physics of Fluids* 20.10 (1977), S124–S132. DOI: [10.1063/1.861721](https://doi.org/10.1063/1.861721).
- [33] H. H. Fernholz and P. J. Finley. "Incompressible zero-pressure-gradient turbulent boundary layer: An assessment of the data". In: *Progress in Aerospace Sciences* 32.4 (1996), pp. 245–311. ISSN: 0376-0421. DOI: [Doi10.1016/0376-0421\(95\)00007-0](https://doi.org/10.1016/0376-0421(95)00007-0).
- [34] F. E. Fish and G. V. Lauder. "Passive and active flow control by swimming fishes and mammals". In: *Annual Review of Fluid Mechanics* 38 (2006), pp. 193–224. ISSN: 0066-4189. DOI: [10.1146/annurev.fluid.38.050304.092201](https://doi.org/10.1146/annurev.fluid.38.050304.092201).
- [35] K. Fukagata, K. Iwamoto, and N. Kasagi. "Contribution of Reynolds stress distribution to the skin friction in wall-bounded flows". In: *Physics of Fluids* 14.11 (2002), pp. L73–L76. ISSN: 1070-6631. DOI: [10.1063/1.1516779](https://doi.org/10.1063/1.1516779).
- [36] M. Gad-El-Hak. "Coherent structures and flow control: genesis and prospect". In: *Bulletin of the Polish Academy of Sciences: Technical Sciences* 67.No. 3 (2019), pp. 411–444. DOI: [10.24425/bpasts.2019.129644](https://doi.org/10.24425/bpasts.2019.129644).
- [37] M. Gad-El-Hak. "Flow Control: Passive, Active, and Reactive Flow Management". In: (2000). DOI: [10.1017/CB09780511529535](https://doi.org/10.1017/CB09780511529535).
- [38] M. Gad-el-Hak and P. R. Bandyopadhyay. "Reynolds Number Effects in Wall-Bounded Turbulent Flows". In: *Applied Mechanics Reviews* 47.8 (Aug. 1994), pp. 307–365. ISSN: 0003-6900. DOI: [10.1115/1.3111083](https://doi.org/10.1115/1.3111083).
- [39] R. García-Mayoral and J. Jiménez. "Drag reduction by riblets". In: *Philosophical transactions. Series A, Mathematical, physical, and engineering sciences* 369 (Apr. 2011), pp. 1412–27. DOI: [10.1098/rsta.2010.0359](https://doi.org/10.1098/rsta.2010.0359).
- [40] D. Gatti and M. Quadrio. "Performance losses of drag-reducing spanwise forcing at moderate values of the Reynolds number". In: *Physics of Fluids* 25.12 (2013). ISSN: 1070-6631. DOI: [Artn12510910.1063/1.4849537](https://doi.org/10.1063/1.4849537).
- [41] D. Gatti and M. Quadrio. "Reynolds-number dependence of turbulent skin-friction drag reduction induced by spanwise forcing". In: *Journal of Fluid Mechanics* 802 (2016), pp. 553–582. ISSN: 0022-1120. DOI: [10.1017/jfm.2016.485](https://doi.org/10.1017/jfm.2016.485).
- [42] W. K. George and L. Castillo. "Zero-Pressure-Gradient Turbulent Boundary Layer". In: *Applied Mechanics Reviews* 50.12 (Dec. 1997), pp. 689–729. ISSN: 0003-6900. DOI: [10.1115/1.3101858](https://doi.org/10.1115/1.3101858).
- [43] A. Glezer and M. Amitay. "Synthetic jets". In: *Annual Review of Fluid Mechanics* 34 (2002), pp. 503–529. ISSN: 0066-4189. DOI: [DOI10.1146/annurev.fluid.34.090501.094913](https://doi.org/10.1146/annurev.fluid.34.090501.094913).
- [44] D. Gottlieb and C. Shu. "On the Gibbs phenomenon and its resolution". In: *SIAM review* 39.4 (1997), pp. 644–668.
- [45] M. D. Graham and D. Floryan. "Exact Coherent States and the Nonlinear Dynamics of Wall-Bounded Turbulent Flows". In: *Annual Review of Fluid Mechanics* 53.1 (2021), null. DOI: [10.1146/annurev-fluid-051820-020223](https://doi.org/10.1146/annurev-fluid-051820-020223).
- [46] J. M. Hamilton, J. Kim, and F. Waleffe. "Regeneration Mechanisms of near-Wall Turbulence Structures". In: *Journal of Fluid Mechanics* 287 (1995), pp. 317–348. ISSN: 0022-1120. DOI: [Doi10.1017/S0022112095000978](https://doi.org/10.1017/S0022112095000978).

- [47] K. J. Harder and W. G. Tiederman. “Drag Reduction and Turbulent Structure in 2-Dimensional Channel Flows”. In: *Philosophical Transactions of the Royal Society of London Series a-Mathematical Physical and Engineering Sciences* 336.1640 (1991), pp. 19–34. DOI: [DOI10.1098/rsta.1991.0064](https://doi.org/10.1098/rsta.1991.0064).
- [48] M. R. Head and P. Bandyopadhyay. “New Aspects of Turbulent Boundary-Layer Structure”. In: *Journal of Fluid Mechanics* 107.Jun (1981), pp. 297–338. ISSN: 0022-1120. DOI: [Doi10.1017/S0022112081001791](https://doi.org/10.1017/S0022112081001791).
- [49] N. Hutchins and I. Marusic. “Large-scale influences in near-wall turbulence”. In: *Philosophical Transactions of the Royal Society a-Mathematical Physical and Engineering Sciences* 365.1852 (2007), pp. 647–664. ISSN: 1364-503x. DOI: [10.1098/rsta.2006.1942](https://doi.org/10.1098/rsta.2006.1942).
- [50] J. Hwang, J. Lee, H. J. Sung, and T. A. Zaki. “Inner-outer interactions of large-scale structures in turbulent channel flow”. In: *Journal of Fluid Mechanics* 790 (2016). ISSN: 0022-1120. DOI: [10.1017/jfm.2016.3](https://doi.org/10.1017/jfm.2016.3).
- [51] J. Jimenez. “Cascades in Wall-Bounded Turbulence”. In: *Annual Review of Fluid Mechanics, Vol 44* 44 (2012), pp. 27–45. ISSN: 0066-4189. DOI: [10.1146/annurev-fluid-120710-101039](https://doi.org/10.1146/annurev-fluid-120710-101039).
- [52] J. Jimenez. “Near-wall turbulence”. In: *Physics of Fluids* 25.10 (2013). ISSN: 1070-6631. DOI: [Artn10130210.1063/1.4824988](https://doi.org/10.1063/1.4824988).
- [53] W. J. Jung, N. Mangiavacchi, and R. Akhavan. “Suppression of Turbulence in Wall-Bounded Flows by High-Frequency Spanwise Oscillations”. In: *Physics of Fluids A* 4.8 (1992), pp. 1605–1607. ISSN: 0899-8213. DOI: [Doi10.1063/1.858381](https://doi.org/10.1063/1.858381).
- [54] C. J. Kahler, S. Scharnowski, and C. Cierpka. “On the uncertainty of digital PIV and PTV near walls”. In: *Experiments in Fluids* 52.6 (2012), pp. 1641–1656. ISSN: 0723-4864. DOI: [10.1007/s00348-012-1307-3](https://doi.org/10.1007/s00348-012-1307-3).
- [55] L. Keefe. “A normal vorticity actuator for near-wall modification of turbulent shear flows”. In: *35th Aerospace Sciences Meeting and Exhibit*. 1997. DOI: [10.2514/6.1997-547](https://doi.org/10.2514/6.1997-547).
- [56] K. U. Kempaiah, F. Scarano, G. E. Elsinga, B. W. van Oudheusden, and L. BermeL. “3-dimensional particle image velocimetry based evaluation of turbulent skin-friction reduction by spanwise wall oscillation”. In: *Physics of Fluids* 32.8 (2020). ISSN: 1070-6631. DOI: [Artn08511110.1063/5.0015359](https://doi.org/10.1063/5.0015359).
- [57] Kevin, J. Monty, and N. Hutchins. “Turbulent structures in a statistically three-dimensional boundary layer”. In: *Journal of Fluid Mechanics* 859 (2019), pp. 543–565. ISSN: 0022-1120. DOI: [10.1017/jfm.2018.814](https://doi.org/10.1017/jfm.2018.814).
- [58] J. Kim, P. Moin, and R. Moser. “The Turbulence Statistics in Fully Developed Channel Flow at Low Reynolds Number”. In: *Journal of Fluid Mechanics* 177 (May 1987). DOI: [10.1017/S0022112087000892](https://doi.org/10.1017/S0022112087000892).
- [59] J. C. Klewicki. “Reynolds Number Dependence, Scaling, and Dynamics of Turbulent Boundary Layers”. In: *Journal of Fluids Engineering* 132.9 (2010). ISSN: 0098-2202. DOI: [Artn09400110.1115/1.4002167](https://doi.org/10.1115/1.4002167).
- [60] J. C. Klewicki, M. M. Metzger, E. Kelner, and E. M. Thurlow. “Viscous Sublayer Flow Visualizations at R(Theta)Similar-or-Equal-to-1,500,000”. In: *Physics of Fluids* 7.4 (1995), pp. 857–863. ISSN: 1070-6631. DOI: [Doi10.1063/1.868763](https://doi.org/10.1063/1.868763).
- [61] S. J. Kline, W. C. Reynolds, F. A. Schraub, and P. W. Runstadler. “Structure of Turbulent Boundary Layers”. In: *Journal of Fluid Mechanics* 30 (1967), pp. 741–773. ISSN: 0022-1120. DOI: [Doi10.1017/S0022112067001740](https://doi.org/10.1017/S0022112067001740).

- [62] P. A. Krogstad and R. A. Antonia. "Surface roughness effects in turbulent boundary layers". In: *Experiments in Fluids* 27.5 (1999), pp. 450–460. ISSN: 0723-4864. DOI: [DOI10.1007/s003480050370](https://doi.org/10.1007/s003480050370).
- [63] F. Laadhari, L. Skandaji, and R. Morel. "Turbulence Reduction in a Boundary-Layer by a Local Spanwise Oscillating Surface". In: *Physics of Fluids* 6.10 (1994), pp. 3218–3220. ISSN: 1070-6631. DOI: [Doi10.1063/1.868052](https://doi.org/10.1063/1.868052).
- [64] A. Levoni and D. Modesti. *Rotating discs: direct numerical simulations for turbulent drag reduction*. TU Delft MSc. Thesis. 2021.
- [65] J. L. Lumley and I. Kubo. *Turbulent Drag Reduction by Polymer Additives: A Survey*. Ed. by Bernhard Gampert. Springer Berlin Heidelberg, 1985, pp. 3–21. ISBN: 978-3-642-82632-0.
- [66] A. Mahashabde, P. Wolfe, A. Ashok, C. Dorbian, Q. X. He, A. Fan, S. Lukachko, A. Mozdzanowska, C. Wollersheim, S. R. H. Barrett, M. Locke, and I. A. Waitz. "Assessing the environmental impacts of aircraft noise and emissions". In: *Progress in Aerospace Sciences* 47.1 (2011), pp. 15–52. ISSN: 0376-0421. DOI: [10.1016/j.paerosci.2010.04.003](https://doi.org/10.1016/j.paerosci.2010.04.003).
- [67] J. P. Marec. "Drag reduction: a major task for research". In: *Aerodynamic Drag Reduction Technologies* 76 (2001), pp. 17–27.
- [68] I. Marusic and R. J. Adrian. "The Eddies and Scales of Wall Turbulence". In: *Ten Chapters in Turbulence*. Ed. by Peter A. Davidson, Yukio Kaneda, and Katapalli R. Editors Sreenivasan. Cambridge University Press, 2012, pp. 176220. DOI: [10.1017/CB09781139032810.006](https://doi.org/10.1017/CB09781139032810.006).
- [69] I. Marusic, W. J. Baars, and N. Hutchins. "An extended view of the inner-outer interaction model for wall-bounded turbulence using spectral linear stochastic estimation". In: *Frontiers in Fluid Mechanics Research* 126 (2015), pp. 24–28. ISSN: 1877-7058. DOI: [10.1016/j.proeng.2015.11.171](https://doi.org/10.1016/j.proeng.2015.11.171).
- [70] I. Marusic, W. J. Baars, and N. Hutchins. "Scaling of the streamwise turbulence intensity in the context of inner-outer interactions in wall turbulence". In: *Physical Review Fluids* 2.10 (2017). ISSN: 2469-990x. DOI: [ARTN10050210.1103/PhysRevFluids.2.100502](https://doi.org/10.1103/PhysRevFluids.2.100502).
- [71] I. Marusic, R. Mathis, and N. Hutchins. "High Reynolds number effects in wall turbulence". In: *International Journal of Heat and Fluid Flow* 31.3 (2010), pp. 418–428. ISSN: 0142-727x. DOI: [10.1016/j.ijheatfluidflow.2010.01.005](https://doi.org/10.1016/j.ijheatfluidflow.2010.01.005).
- [72] I. Marusic and A. E. Perry. "A Wall-Wake Model for the Turbulence Structure of Boundary-Layers .2. Further Experimental Support". In: *Journal of Fluid Mechanics* 298 (1995), pp. 389–407. ISSN: 0022-1120. DOI: [Doi10.1017/S0022112095003363](https://doi.org/10.1017/S0022112095003363).
- [73] P. A. Monkewitz, K. A. Chauhan, and H. M. Nagib. "Self-consistent high-Reynolds-number asymptotics for zero-pressure-gradient turbulent boundary layers". In: *Physics of Fluids* 19.11 (2007). ISSN: 1070-6631. DOI: [Artn11510110.1063/1.2780196](https://doi.org/10.1063/1.2780196).
- [74] J. Murlis, H. M. Tsai, and P. Bradshaw. "The Structure of Turbulent Boundary-Layers at Low Reynolds-Numbers". In: *Journal of Fluid Mechanics* 122.Sep (1982), pp. 13–56. ISSN: 0022-1120. DOI: [Doi10.1017/S0022112082002080](https://doi.org/10.1017/S0022112082002080).
- [75] P. Olivucci, P. Ricco, and S. K. Aghdam. "Turbulent drag reduction by rotating rings and wall-distributed actuation". In: *Physical Review Fluids* 4.9 (2019). ISSN: 2469-990x. DOI: [ARTN09390410.1103/PhysRevFluids.4.093904](https://doi.org/10.1103/PhysRevFluids.4.093904).
- [76] H. Osaka, T. Kameda, and S. Mochizuki. "Re-examination of the Reynolds-number-effect on the mean flow quantities in a smooth wall turbulent boundary layer". In: *Jsm International Journal Series B-Fluids and Thermal Engineering* 41.1 (1998), pp. 123–129. ISSN: 1340-8054. DOI: [DOI10.1299/jsmeb.41.123](https://doi.org/10.1299/jsmeb.41.123).

- [77] G. F. Oweis, E. S. Winkel, J. M. Cutbrith, S. L. Ceccio, M. Perlin, and D. R. Dowling. "The mean velocity profile of a smooth-flat-plate turbulent boundary layer at high Reynolds number". In: *Journal of Fluid Mechanics* 665 (2010), pp. 357381. DOI: [10.1017/S0022112010003952](https://doi.org/10.1017/S0022112010003952).
- [78] M. Perlin, D. R. Dowling, and S. L. Ceccio. "Freeman Scholar Review: Passive and Active Skin-Friction Drag Reduction in Turbulent Boundary Layers". In: *Journal of Fluids Engineering* 138.9 (June 2016). 091104. ISSN: 0098-2202. DOI: [10.1115/1.4033295](https://doi.org/10.1115/1.4033295).
- [79] A. E. Perry and M. S. Chong. "On the Mechanism of Wall Turbulence". In: *Journal of Fluid Mechanics* 119.Jun (1982), pp. 173–217. ISSN: 0022-1120. DOI: [Doi10.1017/S0022112082001311](https://doi.org/10.1017/S0022112082001311).
- [80] A. E. Perry, I. Marusic, and M. B. Jones. "On the streamwise evolution of turbulent boundary layers in arbitrary pressure gradients". In: *Journal of Fluid Mechanics* 461 (2002), pp. 61–91. ISSN: 0022-1120. DOI: [10.1017/S002211200200825x](https://doi.org/10.1017/S002211200200825x).
- [81] S. Pirozzoli, M. Bernardini, and F. Grasso. "On the dynamical relevance of coherent vortical structures in turbulent boundary layers". In: *Journal of Fluid Mechanics* 648 (2010), pp. 325–349. ISSN: 0022-1120. DOI: [10.1017/S0022112009993156](https://doi.org/10.1017/S0022112009993156).
- [82] S. B. Pope. "Turbulent Flows". In: *Measurement Science and Technology* 12.11 (2001), pp. 2020–2021. DOI: [10.1088/0957-0233/12/11/705](https://doi.org/10.1088/0957-0233/12/11/705).
- [83] M. Quadrio and P. Ricco. "Critical assessment of turbulent drag reduction through spanwise wall oscillations". In: *Journal of Fluid Mechanics* 521 (2004), pp. 251–271. ISSN: 0022-1120. DOI: [10.1017/S0022112004001855](https://doi.org/10.1017/S0022112004001855).
- [84] M. Quadrio and P. Ricco. "The laminar generalized Stokes layer and turbulent drag reduction". In: *Journal of Fluid Mechanics* 667 (2011), pp. 135–157. ISSN: 0022-1120. DOI: [10.1017/S0022112010004398](https://doi.org/10.1017/S0022112010004398).
- [85] M. Quadrio, P. Ricco, and C. Viotti. "Streamwise-travelling waves of spanwise wall velocity for turbulent drag reduction". In: *Journal of Fluid Mechanics* 627 (2009), pp. 161–178. ISSN: 0022-1120. DOI: [10.1017/S0022112009006077](https://doi.org/10.1017/S0022112009006077).
- [86] M. Raffel, C. E. Willert, S. T. Wereley, and J. Kompenhans. *Particle Image Velocimetry: A Practical Guide, Second Edition*. 2018, pp. 1–448. DOI: [10.1007/978-3-540-72308-0](https://doi.org/10.1007/978-3-540-72308-0).
- [87] P. Ricco. "Modification of near-wall turbulence due to spanwise wall oscillations". In: *Journal of Turbulence* 5 (2004). ISSN: 1468-5248. DOI: [Artn024PiiS1468-5248\(04\)76185-810.1088/1468-5248/5/1/024](https://doi.org/10.1088/1468-5248/5/1/024).
- [88] P. Ricco and S. Hahn. "Turbulent drag reduction through rotating discs". In: *Journal of Fluid Mechanics* 722 (2013), pp. 267–290. ISSN: 0022-1120. DOI: [10.1017/jfm.2013.92](https://doi.org/10.1017/jfm.2013.92).
- [89] P. Ricco, C. Ottonelli, Y. Hasegawa, and M. Quadrio. "Changes in turbulent dissipation in a channel flow with oscillating walls". In: *Journal of Fluid Mechanics* 700 (2012), pp. 77–104. ISSN: 0022-1120. DOI: [10.1017/jfm.2012.97](https://doi.org/10.1017/jfm.2012.97).
- [90] P. Ricco and M. Quadrio. "Wall-oscillation conditions for drag reduction in turbulent channel flow". In: *International Journal of Heat and Fluid Flow* 29.4 (2008), pp. 891–902. ISSN: 0142-727x. DOI: [10.1016/j.ijheatfluidflow.2007.12.005](https://doi.org/10.1016/j.ijheatfluidflow.2007.12.005).
- [91] P. Ricco, M. Skote, and M. A. Leschziner. "A review of turbulent skin-friction drag reduction by near-wall transverse forcing". In: *Progress in Aerospace Sciences* 123 (2021), p. 100713. ISSN: 0376-0421. DOI: <https://doi.org/10.1016/j.paerosci.2021.100713>.
- [92] L. F. Richardson. *Weather prediction by numerical process*. Cambridge University Press, 1922.
- [93] S. K. Robinson. "Coherent motions in the turbulent boundary layer". In: *Annual Review of Fluid Mechanics* 23 (1991), pp. 601–639. DOI: [10.1146/annurev.fl.23.010191.003125](https://doi.org/10.1146/annurev.fl.23.010191.003125).

- [94] J. P. Rothstein. "Slip on Superhydrophobic Surfaces". In: *Annual Review of Fluid Mechanics* 42.1 (2010), pp. 89–109. DOI: [10.1146/annurev-fluid-121108-145558](https://doi.org/10.1146/annurev-fluid-121108-145558).
- [95] F. Scarano. "Theory of non-isotropic spatial resolution in PIV". In: *Experiments in Fluids* 35.3 (2003), pp. 268–277. ISSN: 0723-4864. DOI: [10.1007/s00348-003-0655-4](https://doi.org/10.1007/s00348-003-0655-4).
- [96] S. Scharnowski and C. J. Kahler. "Estimation and optimization of loss-of-pair uncertainties based on PIV correlation functions". In: *Experiments in Fluids* 57.2 (2016). ISSN: 0723-4864. DOI: [ARTN2310.1007/s00348-015-2108-2](https://doi.org/ARTN2310.1007/s00348-015-2108-2).
- [97] S. Scharnowski and C. J. Kahler. "Particle image velocimetry - Classical operating rules from today's perspective". In: *Optics and Lasers in Engineering* 135 (2020). ISSN: 0143-8166. DOI: [ARTN10618510.1016/j.optlaseng.2020.106185](https://doi.org/ARTN10618510.1016/j.optlaseng.2020.106185).
- [98] P. Schlatter and R. Örlü. "Assessment of direct numerical simulation data of turbulent boundary layers". In: *Journal of Fluid Mechanics* 659 (2010). DOI: [10.1017/S0022112010003113](https://doi.org/10.1017/S0022112010003113).
- [99] G. Schrauf. "Status and perspectives of laminar flow". In: *The Aeronautical Journal* (1968) 109.1102 (2005), pp. 639644. DOI: [10.1017/S000192400000097X](https://doi.org/10.1017/S000192400000097X).
- [100] F. F. J. Schrijer and F. Scarano. "Effect of predictor-corrector filtering on the stability and spatial resolution of iterative PIV interrogation". In: *Experiments in Fluids* 45.5 (2008), pp. 927–941. ISSN: 0723-4864. DOI: [10.1007/s00348-008-0511-7](https://doi.org/10.1007/s00348-008-0511-7).
- [101] M. P. Schultz and K. A. Flack. "Outer layer similarity in fully rough turbulent boundary layers". In: *Experiments in Fluids* 38.3 (2005), pp. 328–340. ISSN: 0723-4864. DOI: [10.1007/s00348-004-0903-2](https://doi.org/10.1007/s00348-004-0903-2).
- [102] P. Sforza. "Chapter 9 - Drag Estimation". In: *Commercial Airplane Design Principles*. Ed. by Pasquale Sforza. Boston: Butterworth-Heinemann, 2014, pp. 349–353. ISBN: 978-0-12-419953-8. DOI: <https://doi.org/10.1016/B978-0-12-419953-8.00009-7>.
- [103] J. A. Sillero, J. Jimenez, and R. D. Moser. "One-point statistics for turbulent wall-bounded flows at Reynolds numbers up to  $\delta^+$  approximate to 2000". In: *Physics of Fluids* 25.10 (2013). ISSN: 1070-6631. DOI: [Artn10510210.1063/1.4823831](https://doi.org/Artn10510210.1063/1.4823831).
- [104] J. A. Sillero, J. Jimenez, and R. D. Moser. "Two-point statistics for turbulent boundary layers and channels at Reynolds numbers up to  $\delta^+$  approximate to 2000". In: *Physics of Fluids* 26.10 (2014). ISSN: 1070-6631. DOI: [Artn10510910.1063/1.4899259](https://doi.org/Artn10510910.1063/1.4899259).
- [105] M. Skote. "Comparison between spatial and temporal wall oscillations in turbulent boundary layer flows". In: *Journal of Fluid Mechanics* 730 (2013), pp. 273–294. ISSN: 0022-1120. DOI: [10.1017/jfm.2013.344](https://doi.org/10.1017/jfm.2013.344).
- [106] M. Skote. "Turbulent boundary layer flow subject to streamwise oscillation of spanwise wall-velocity". In: *Physics of Fluids* 23.8 (2011). ISSN: 1070-6631. DOI: [Artn08170310.1063/1.3626028](https://doi.org/Artn08170310.1063/1.3626028).
- [107] C. Smith and S. Metzler. "The Characteristics of Low-Speed Streaks in the Near-Wall Region of a Turbulent Boundary Layer". In: *Journal of Fluid Mechanics* 129 (Apr. 1983), pp. 27–54. DOI: [10.1017/S0022112083000634](https://doi.org/10.1017/S0022112083000634).
- [108] A. J. Smits, B. J. McKeon, and I. Marusic. "High-Reynolds Number Wall Turbulence". In: *Annual Review of Fluid Mechanics, Vol 43* 43 (2011), pp. 353–375. ISSN: 0066-4189. DOI: [10.1146/annurev-fluid-122109-160753](https://doi.org/10.1146/annurev-fluid-122109-160753).
- [109] P. R. Spalart and J. D. McLean. "Drag reduction: enticing turbulence, and then an industry". In: *Philosophical Transactions of the Royal Society a-Mathematical Physical and Engineering Sciences* 369.1940 (2011), pp. 1556–1569. ISSN: 1364-503x. DOI: [10.1098/rsta.2010.0369](https://doi.org/10.1098/rsta.2010.0369).

- [110] T. Theodorsen. "The structure of turbulence". In: *50 Jahre Grenzschichtforschung: Eine Festschrift in Originalbeiträgen*. Ed. by H. Görtler and W. Tollmien. Wiesbaden: Vieweg+Teubner Verlag, 1955, pp. 55–62. ISBN: 978-3-663-20219-6. DOI: [10.1007/978-3-663-20219-6\\_6](https://doi.org/10.1007/978-3-663-20219-6_6).
- [111] E. Toubert and M. A. Leschziner. "Near-wall streak modification by spanwise oscillatory wall motion and drag-reduction mechanisms". In: *Journal of Fluid Mechanics* 693 (2012), pp. 150–200. ISSN: 0022-1120. DOI: [10.1017/jfm.2011.507](https://doi.org/10.1017/jfm.2011.507).
- [112] A. A. Townsend. "The Structure of the Turbulent Boundary Layer". In: *Proceedings of the Cambridge Philosophical Society* 47.2 (1951), pp. 375–395. DOI: [Doi10.1017/S0305004100026724](https://doi.org/10.1017/S0305004100026724).
- [113] C. Viotti, M. Quadrio, and P. Luchini. "Streamwise oscillation of spanwise velocity at the wall of a channel for turbulent drag reduction". In: *Physics of Fluids* 21.11 (2009). ISSN: 1070-6631. DOI: [Artn11510910.1063/1.3266945](https://doi.org/Artn11510910.1063/1.3266945).
- [114] J. M. Wallace. "Quadrant Analysis in Turbulence Research: History and Evolution". In: *Annual Review of Fluid Mechanics* 48 (2016), pp. 131–158. ISSN: 0066-4189. DOI: [10.1146/annurev-fluid-122414-034550](https://doi.org/10.1146/annurev-fluid-122414-034550).
- [115] J. M. Wallace, R. S. Brodkey, and H. Eckelmann. "Wall Region in Turbulent Shear-Flow". In: *Journal of Fluid Mechanics* 54.Jul11 (1972), pp. 39–+. ISSN: 0022-1120. DOI: [Doi10.1017/S0022112072000515](https://doi.org/10.1017/S0022112072000515).
- [116] Michael J. Walsh. "Riblets as a Viscous Drag Reduction Technique". In: *AIAA Journal* 21.4 (1983), pp. 485–486. DOI: [10.2514/3.60126](https://doi.org/10.2514/3.60126).
- [117] J. Westerweel and F. Scarano. "Universal outlier detection for PIV data". In: *Experiments in Fluids* 39.6 (2005), pp. 1096–1100. ISSN: 0723-4864. DOI: [10.1007/s00348-005-0016-6](https://doi.org/10.1007/s00348-005-0016-6).
- [118] C. M. White and M. G. Mungal. "Mechanics and prediction of turbulent drag reduction with polymer additives". In: *Annual Review of Fluid Mechanics* 40 (2008), pp. 235–256. ISSN: 0066-4189. DOI: [10.1146/annurev.fluid.40.111406.102156](https://doi.org/10.1146/annurev.fluid.40.111406.102156).
- [119] A. P. Willis, Y. G. Hwang, and C. Cossu. "Optimally amplified large-scale streaks and drag reduction in turbulent pipe flow". In: *Physical Review Fluids* 82.3 (2010). ISSN: 1539-3755. DOI: [ARTN03632110.1103/PhysRevE.82.036321](https://doi.org/ARTN03632110.1103/PhysRevE.82.036321).
- [120] D. J. Wise, C. Alvarenga, and P. Ricco. "Spinning out of control: Wall turbulence over rotating discs". In: *Physics of Fluids* 26.12 (2014). ISSN: 1070-6631. DOI: [Artn12510710.1063/1.4903973](https://doi.org/Artn12510710.1063/1.4903973).
- [121] D. J. Wise, P. Olivucci, and P. Ricco. "Turbulent drag reduction through oscillating discs (vol 746, pg 536, 2014)". In: *Journal of Fluid Mechanics* 856 (2018), pp. 1064–1066. ISSN: 0022-1120. DOI: [10.1017/jfm.2018.720](https://doi.org/10.1017/jfm.2018.720).
- [122] D. J. Wise and P. Ricco. "Turbulent drag reduction through oscillating discs". In: *Journal of Fluid Mechanics* 746 (2014), pp. 536–564. ISSN: 0022-1120. DOI: [10.1017/jfm.2014.122](https://doi.org/10.1017/jfm.2014.122).
- [123] K. M. Yoo, P. Merati, and H. M. McMahon. "Experimental Investigation of a Turbulent-Flow in the Vicinity of an Appendage Mounted on a Flat-Plate". In: *Journal of Fluids Engineering* 113.4 (1991), pp. 635–642. ISSN: 0098-2202. DOI: [Doi10.1115/1.2926527](https://doi.org/10.1115/1.2926527).
- [124] B. F. Zhang, K. Liu, Y. Zhou, S. To, and J. Y. Tu. "Active drag reduction of a high-drag Ahmed body based on steady blowing". In: *Journal of Fluid Mechanics* 856 (2018), pp. 351–396. ISSN: 0022-1120. DOI: [10.1017/jfm.2018.703](https://doi.org/10.1017/jfm.2018.703).